MOLECULAR GAS AND STAR FORMATION IN EARLY MERGER ARP 240

Molecular Gas and Star Formation in Early Merger Arp 240

By

Hao He, B.Sc.

A Thesis

Submitted to the School of Graduate Studies

in the Partial Fulfilment of the Requirements

for the Degree

Master of Science

McMaster University

McMaster University MASTER OF SCIENCE (2019) Hamilton, Ontario

(Physics and Astronomy)

TITLE: Molecular Gas and Star Formation in Early Merger Arp 240

AUTHOR: Hao He, B.Sc. (Xiamen University)

SUPERVISOR: Dr. Christine D. Wilson

NUMBER OF PAGES: xii, 119

Abstract

This thesis presents ^{12}CO J=1-0 J=2-1 and ^{13}CO J=1-0 maps of an early-stage galaxy merger Arp 240 observed with ALMA. Arp 240 has a high star formation efficiency but relatively normal gas fraction, which is in contrast with typical merging pairs. We applied RADEX modeling to fit the molecular gas properties. We found that the gas concentrated regions in this system have CO-to-H_2 conversion factors closer to typical ultra-luminous infrared galaxy (ULRG) values. This conversion factor value is consistent with that derived from LTE analysis. Adopting the ULIRG conversion factor, we explored the relationship between molecular gas surface density Σ_{mol} and star formation rate surface density Σ_{SFR}, which is traced by 33 GHz radio continuum from the VLA. We found that the star forming regions generally have a combined Toomre factor $Q_{tot} < 0.5$, with the exception of the center of NGC 5257, which has $Q_{tot} \sim 1$. This suggests these star forming regions are undergoing gravitational instability. We further calculated the star formation efficiency per freefall time ϵ_{ff} on galactic scales for these regions. It turns out some regions have ϵ_{ff} exceeding 100%. We argue that ϵ_{ff} on giant molecular cloud (GMC) scales should be about a factor of 10 lower, which might suggest the star forming activity in this system is regulated by cloud collapse on GMC scales.

Acknowledgments

I would like to thank my supervisor Dr. Christine Wilson for guiding me through this project. Your patient instruction and responsive feedback helped me to overcome many obstacles in my research. Moreover, I learnt a lot from your insight on how to find a valuable science question, which will benefit me a lot in the rest of my academic career. With those treasures, I am ready for the next four years of more chanlenging life. I would also like to thank the members of my committee, Dr. Laura Parker and Dr. James Wadsley, who brought different view of apects on my research and makes my committee meeting and defense extremely interesting.

Thank you to all of my friends in astronomy department for accepting me into this big group. It is for you guys that I don't feel alone anymore as a foreigner. Thank you to my groupmates Ashley, Nathan, Ryan and Toby for genuine offer of help in my daily life as well as research. Your kindness truely warms my heart and inspires me to become a caring and helpful person.

Finally thank you to my parents Chunmei Lyu and Jiyue He for supporting me no matter what I am going through. The weekly chat with you always makes me feel refreshed out of fatigue and depression. Although I am far away from home, I would bear your remote caring in my heart all the time.

Contents

List of Figures

List of Tables

List of Abbreviations

ACA Atacama Compact Array.

ALMA Atacama Large Millimeter/Submillimeter Array.

CASA Common Astronomy Software Applications.

CD Central Dominant.

CO carbon monoxide.

FWHM full width at half maximum.

GMC giant molecular cloud.

GOALS Great Observatories All-sky LIRG Survey.

IFU integral field unit.

IMF initial mass function.

ISM interstellar medium.

LIRG luminous infrared galaxy.

LTE local thermal equilibrium.

LVG large velocity gradient.

MS measurement set.

PDF probability density function.

PI principal investigator.

PV position-velocity.

RMS root-mean-square.

S/N signal-to-noise.

SF star forming.

SFE star formation efficiency.

SFR star formation rate.

SM stellar mass.

SMA Submillimeter Array.

SPW spectral windows.

sSFR specific star formation rate.

ULIRG ultraluminous infrared galaxy.

VLA Very Large Array.

Chapter 1

Introduction

1.1 Galaxy Interaction and Merging

In our universe, galaxy interactions play an important role in galactic evolution. Gravitational interaction between galaxies can trigger the formation of tidal tails and warps. These structures commonly exist in disk galaxies such as our Milky Way. Indeed, a survey of HI in disk galaxies by the Very Large Array (VLA) radio telescope demonstrates that a large fraction of disk galaxies displays warps (Bosma 1978). Furthermore, a specific type of interaction called mergers is found to be responsible for the formation of a large portion of elliptical galaxies (Toomre 1977). These elliptical galaxies tend to show a lot of stellar shells with different velocity structures from the cores. Observations show that about 25% of all ellipticals have different velocity fields in their cores compared with their outer regions while 56% of all ellipticals show the signature of faint stellar shells (Carroll & Ostlie 2007). Specifically for giant elliptical galaxies residing in the center of galaxy clusters, which are called Central Dominant (CD) galaxies, the signature of past merging events is more clear as more than half of CD galaxies show multiple nuclei that have velocities different from the overall velocity of the galaxy (Carroll & Ostlie 2007). Simulations also confirm that in various cases mergers can produce ellipticals (Toomre 1977). Generally, the surface brightness profiles of giant elliptical galaxies follow an $r^{1/4}$ trend, which is a normal outcome from the computer simulations (Carroll & Ostlie 2007). Studies on the evolution of galaxy clusters also require mergers to explain certain phenomena. In our local universe, most giant ellipticals reside in the central dense regions of galaxy clusters, while spirals are generally found in the less dense periphery (Oemler 1974). This is called the morphology-density relation. One explanation is that mergers happen at a higher rate in these dense regions and produce giant ellipticals there. This is also consistent with observations which look back in time at high-redshift galaxy clusters. These clusters generally show a higher fraction of spiral galaxies and a smaller fraction of ellipticals (Dressler et al. 1997).

So far we have observed a lot of systems undergoing merging events. Many of the galaxies are found to be extremely luminous at infrared wavelengths, with over $\sim 90\%$ of the energy in this band (Sanders & Mirabel 1996). These galaxies are found to be starburst galaxies, which have star formation rate (SFR) between 10 to 300 $M_{\odot}$/year (Małek et al. 2017). In comparison, the Milky Way only has a SFR of about one or two solar mass per year (Robitaille & Whitney 2010). For most of these systems, the starburst activity is found in the center of the galaxy. As fuel for star formation, we would expect a large amount of the molecular gas in the central region. Generally we can use carbon monoxide (CO) emission line to trace the amount of molecular gas. CO observations confirm the gas concentration in the center of these systems (Larson et al. 2016). Simulations show the collision between two galaxies can reduce the angular momentum of the gas in the outer region and therefore trigger gas inflow towards the center (Mihos & Hernquist 1996a). On the other hand, many systems are found to have starburst events throughout the disk like the Antennae (Mengel et al. 2005). Astronomers now believe that these off-center starburst activities are triggered by compressive turbulence triggered by the tidal interaction (Renaud et al. 2009). Both cases show these systems are perfect laboratories to study an extreme case of star forming (SF) activity. Furthermore, these starburst galaxies are an important piece for studying the star formation history of our universe. The current measured cosmic star formation history shows that the average SFR volume density peaks at z $\sim$ 2 (Madau et al. 1998). Correspondingly, observations also show that the fraction of galaxies that are mergers peaks at that redshift with a value of 10% (Ryan et al. 2008), which suggests the high SF activity at that time is caused by the high merger fraction. On the other hand, the growth of galaxies in clusters also requires these starburst galaxies. Observations generally find that late type galaxies in local galaxy clusters are much more massive than the corresponding early type galaxies in clusters at z $\sim$ 1 (Kodama & Smail 2001) . One explanation may be that these early type galaxies will undergo a lot of merging events later on and grow into giant ellipticals.

Mergers also play an important role in structure formation of the early universe. Astronomers now believe the current structure of the universe is triggered by the fluctuation of density in the early universe shortly after the Big Bang. From our current understanding, most of the fluctuations are in small mass scales ranging from 10^6 to 10^8 $M_\odot$ (Lukić et al. 2007). Therefore, the most massive galaxies, which are about 10^{12} $M_\odot$, should be formed by the merging of those smaller mass filaments. This galaxy formation model is called the Hierarchical Merger Model (Cole et al. 2000). According to this model, collisions and interactions between those small overdensities can disrupt many globular clusters and kick the stars out to be field stars. For our Milky Way, only 10% of the globular clusters have been survived today. This can actually help to explain why the remaining globular clusters span a small mass range ($10^5 \sim 10^6$ $M_{\odot}$) (Harris & Pudritz 1994). The small globular clusters, which have less binding energy, can be more easily disrupted. On the other hand, the more massive clusters will undergo more dynamical friction and quickly spiral into the centers of galaxies, where collisions happen more frequently, and get disrupted as well (Carroll & Ostlie 2007).

1.2 CO-to-H_2 Conversion Factor

Molecular gas is the fuel for star formation activity and therefore is crucial to the evolution of galaxies. It is known that 70 % of regular matter by mass in the universe is hydrogen. Therefore, we would expect the majority of the molecular gas is H_2. However, because H_2 requires high temperatures to be excited, we cannot derive the H_2 mass directly from its emission lines. After helium, the most abundant elements in the interstellar medium (ISM) are carbon and oxygen. In cold environments, they will form CO. CO is more easily excited compared with H_2 with an excitation temperature of 5.53 K. The critical density of H_2 for ^{12}CO J=1-0 emission is about 2200 cm^{-3} (Bolatto et al. 2013). The critical density for a molecular line $j \rightarrow k$ is traditionally defined as the density for which the net radiation decay rate from the higher transition j to the lower transition k equals the collisional excitation rate from lower k to higher j in the optically thin case. The critical density is generally considered as the density above which we start to see the emission line. However, this doesn't hold true for optically thick lines such as ^{12}CO J=1-0. Due to the photon trapping effect, the critical density of ^{12}CO J=1-0 will be reduced as $n_{eff} = n_{crit}/\tau$ (Shirley 2015), where τ is the optical depth of the line. For ^{12}CO J=1-0 the typical optical depth value is about 2–10. Therefore, the effective critical density of ^{12}CO J=1-0 is close to the typical cold molecular gas density.

The molecular gas is in the form of clumpy clouds in the Milky Way and nearby spiral galaxies (Dobbs et al. 2014). These molecular clouds are mostly found to be in virial equilibrium (Sun et al. 2018). For a giant molecular cloud in virial equilibrium, the mass of the cloud can be estimated as (Bolatto et al. 2013)

$$M_{mol} \approx M_{vir} \approx 200 \left[\frac{C^{1.5} L_{CO}}{T_B} \right]^{0.8} \tag{1.1}$$

where M_{vir} is the virial mass in $M_\odot$, T_B is the Rayleigh-Jeans brightness temperature of the emission in K, L_{CO} is the cloud CO luminosity in K km s^{-1} pc^2 and C is the coefficient of the size-linewidth relationship (Larson 1981) with typical value of 0.7 km s^{-1} pc$^{-0.5}$. C can be related to the cloud's surface density Σ_{GMC} via the equation

$$\Sigma_{GMC} \approxeq 331 C^2 \tag{1.2}$$

If we assume the surface density and brightness temperature of a typical giant molecular cloud (GMC) is constant, then we can see that the relation between CO luminosity and molecular gas mass is almost linear. We can then calculate the ratio between the CO luminosity and molecular gas mass, which is the

CO-to-H_2 conversion factor, as

$$\alpha_{CO} = \frac{M_{mol}}{L_{CO}} \approx 6.1 L_{CO}^{-0.2} T_B^{-0.8} \Sigma_{GMC}^{0.6} \tag{1.3}$$

In our Milky Way, the typical value of $\alpha_{\rm CO}$ is about 4.3 $M_\odot$ (K km s^{-1} pc^2)$^{-1}$ (Bolatto et al. 2013, including helium).

The conversion factor in luminous infrared galaxy (LIRG) and ultraluminous infrared galaxy (ULIRG) is different from the Milky Way value. The conversion factor has a negative correlation with brightness temperature, as implied by the equation above. Furthermore, the brightness temperature of the cloud is closely correlated with the kinematic temperature of the gas. This effect could be compensated if the gas surface density is higher in LIRGs and ULIRGs. On the other hand, the derived relationship between molecular gas mass and CO luminosity depends on the assumption that GMCs are virialized. In LIRGs and ULIRGs, a lot of gas may be in the warm phase and not bound to individual clumps. In this case, the luminosity will be overestimated as

$$L_{CO}^{*} = L_{CO} * \sigma^{*}/\sigma \tag{1.4}$$

where L_{CO}^{*} and σ^{*} are the actual CO luminosity and velocity dispersion, L_{CO} and σ are the expected virialized CO luminosity and velocity dispersion. Narayanan et al. (2011) explored the difference in conversion factor between mergers and normal disk galaxies. They found the rise in velocity dispersion and temperature in combination causes the conversion factor to be lower than the Milky Way value by factor of 2 to 10, as shown in Fig. 1.1. However, we can see the $\alpha_{\rm CO}$ they obtained in simulation has a large scat-

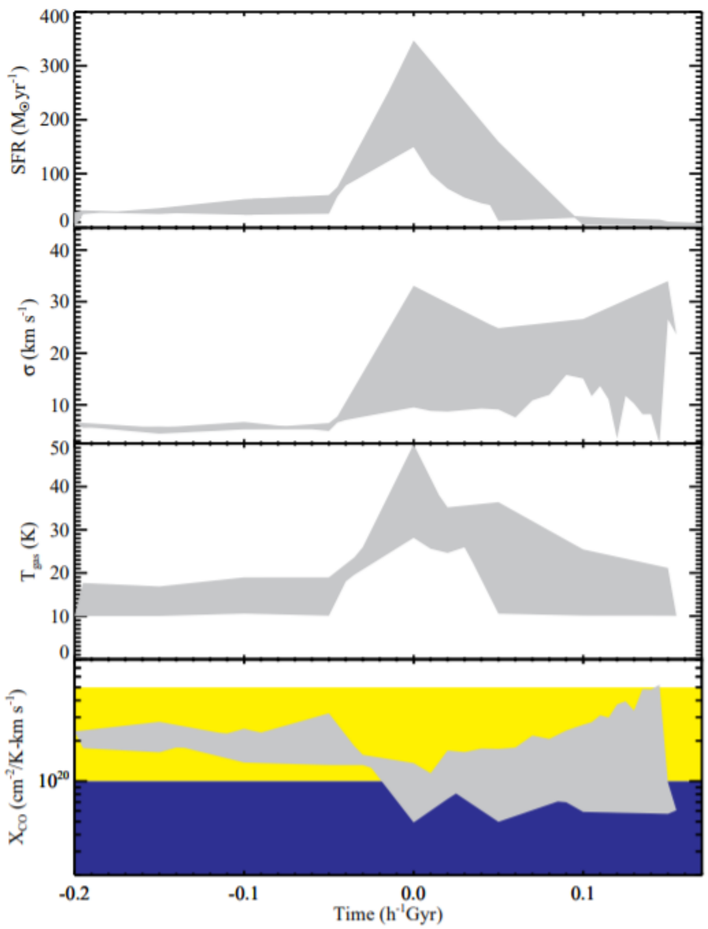

Figure 1.1: The evolution of SFR, temperature, GMC velocity dispersion and conversion factor α_{CO} as a function of time in simulated merging models (Narayanan et al. 2011). The gray shaded regions are the range of emission weighted values for the model. In the bottom panel the yellow and blue regions specify the range of the Milky Way and ULIRG α_{CO} respectively.

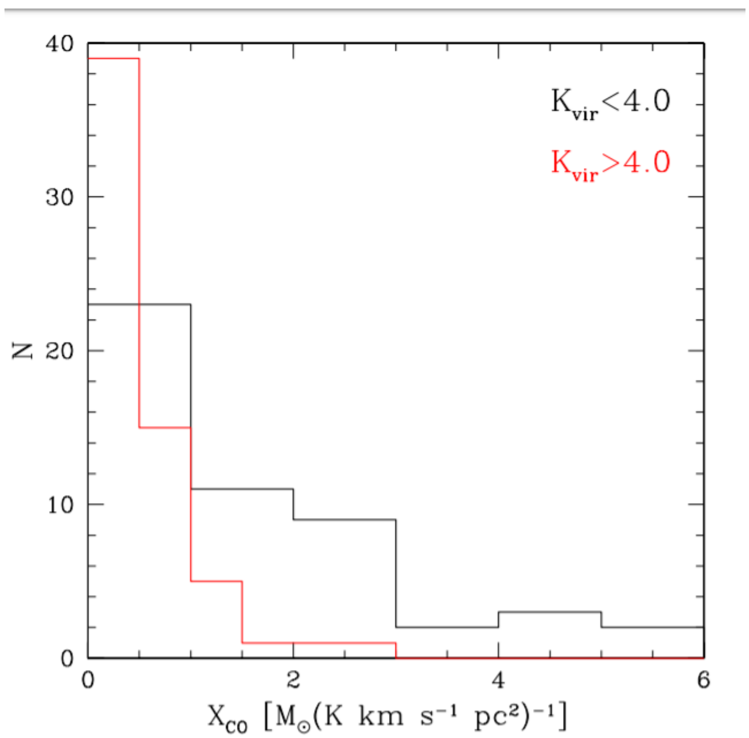

Figure 1.2: The histogram of α_{CO} calculated in a sample of LIRGs using a one phase large velocity gradient (LVG) model (Papadopoulos et al. 2012). K_{vir} is the parameter for the gas kinematic state. The gas is self-gravitating for $1 < K_{vir} < 4$ and unbound for $K_{vir} > 4$.

ter depending on specific merger parameters. Narayanan et al. (2012) further introduce the calibrated conversion factor in relation with CO intensity and metallicity. However, this calibration has a large uncertainty and needs careful treatment. In observations, the molecular gas mass of ULIRGs calculated with the Milky Way conversion factor usually exceeds the dynamical mass of the system (e.g. Downes & Solomon 1998). The molecular gas mass derived from the dust mass assuming Galactic gas-to-dust mass ratio also confirms the need for a smaller conversion factor (Bolatto et al. 2013). To constrain the molecular gas mass, a multi-transition CO line analysis has been used. The typical ULIRG conversion factor is $\alpha_{CO} \sim 0.8\mathrm{M}_{\odot}(\mathrm{Kkms}^{-1}\mathrm{pc}^2)^{-1}$ (Downes & Solomon 1998). The conversion factor of LIRGs is similar. Papadopoulos et al. (2012) performed a large survey of LIRGs with $L_{FIR} > 10^{11}\mathrm{L}_{\odot}$ and found $\alpha_{\mathrm{CO}} \approx 0.6 \pm 0.2\mathrm{M}_{\odot}(\mathrm{Kkms}^{-1}\mathrm{pc}^2)^{-1}$. They further point out that although the gas temperature in U/LIRGs is generally higher (~ 100 K), the increase in velocity dispersion is the major driver for the lower ULIRG α_{CO} value, as demonstrated in Fig. 1.2. For typical ULIRGs such as Arp 220 and NGC 6240, the adoption of a fully bound GMC parameter will bring the calculated α_{CO} back to the Milky Way value. Individual studies of starburst galaxies like M82 (Wild et al. 1992) and the Antennae (Zhu et al. 2003) also confirm a similar ULIRG α_{CO}.

1.3 Turbulence Model for Star Formation

Kennicutt (1998) found there was a general relationship between the SFR and the amount of gas

$$\Sigma_{SFR} \sim \Sigma_{gas}^{N} \tag{1.5}$$

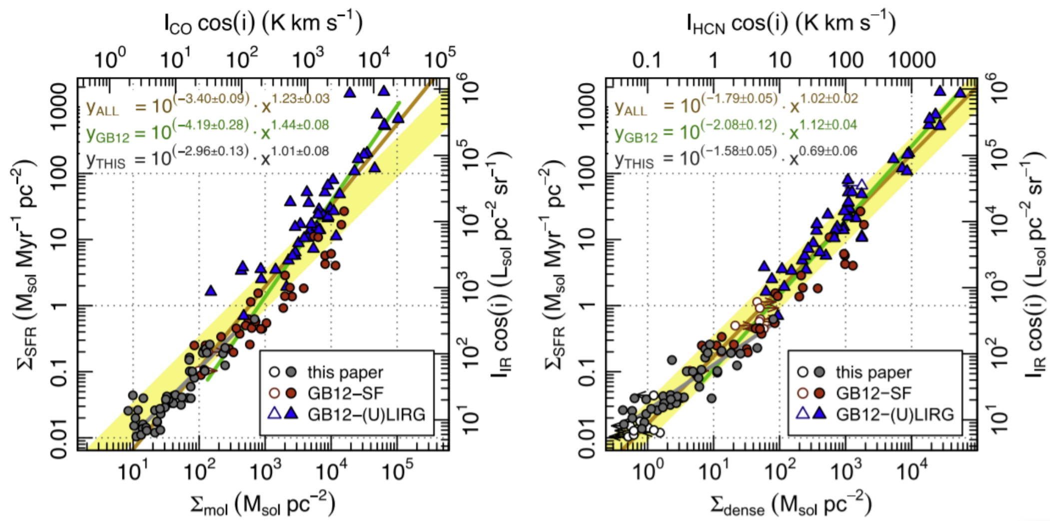

Figure 1.3: The comparison of the Kennicutt-Schmidt law for (Left) Σ_{mol} traced by CO and (Right) Σ_{dense} traced by HCN on kpc scale (Usero et al. 2015). The blue triangles and red dots are data for star forming galaxies and (U)LIRGs respectively from García-Burillo et al. (2012). The equation indicates the power law fitting for data from Usero et al. (2015) (gray line), García-Burillo et al. (2012) (green line) and combined data (brown line). The yellow shaded region indicates the power law index of 1.0 with a factor of 2 scatter.

where Σ_{SFR} and Σ_{gas} are the surface densities of the star formation rate and gas. The index N is typically 1.4 for the total gas including HI and H_2 (Kennicutt & Evans 2012). This relationship generally holds true for $\Sigma_{gas} > 10$ $M_\odot$ pc^{-2}. Recent studies find that Σ_{SFR} is more correlated to the amount of molecular gas Σ_{mol} with fitted index N$= 1.0 \pm 0.2$ (Bigiel et al. 2008, 2011). This means a molecular gas depletion time t_{dep}, which is the time to use up all the gas to form stars, is generally constant. This corresponds to a depletion time, which is the time to consume all the gas for star formation, of $\sim 10^9$ yrs for a normal disk galaxy. The inverse of the depletion time is called the star formation efficiency (SFE)

However, the linear relation between SFR and molecular gas mass is limited to the low density regime ($\Sigma_{mol} < 100$ M$_\odot$ pc^{-2}) and has a large scatter which could be attributed to the local environment. When entering the high Σ_{mol} regime, this relationship becomes superlinear with N $\sim$ 1.4, where most points are from starburst galaxies (Daddi et al. 2010). Usero et al. (2015) found that while the depletion time decreases as Σ_{mol} increases, the depletion time for dense gas, which is traced by HCN emission, stays almost constant in the whole range of Σ_{mol}. This can be accounted for by a turbulence regulated model (Krumholz & McKee 2005).

Both simulations and theory demonstrate that gas regulated by supersonic isothermal turbulence has a log-normal probability density function (PDF) for the volume density (Nordlund & Padoan 1999; Padoan & Nordlund 2002), which is

$$dp(x) = \frac{1}{\sqrt{2\pi\sigma_{width}^2}} \exp\left[-\frac{\ln x - \overline{\ln x}}{2\sigma_{width}^2}\right] \frac{dx}{x} \tag{1.6}$$

where $x = \frac{\rho}{\rho_0}$ is the density normalized by the mean density of the region ρ_0. The mean of the log density is

$$\overline{\ln x} = -\frac{\sigma_{width}^2}{2} \tag{1.7}$$

and the dispersion of the PDF is

$$\sigma_{width} \approx \left[\ln(1 + \frac{3\mathcal{M}^2}{4})\right]^{\frac{1}{2}} \tag{1.8}$$

where $\mathcal{M}$ is the Mach number. In this scenario, only the gas with density above the critical density can form stars. The critical density in this case is set to be the density at which the Jeans length of this density is equal to the sonic length of the cloud. Then the dense gas fraction of the system is

$$f_{dense} = \int_{x_{crit}}^{\infty} x \frac{dp}{dx} dx \tag{1.9}$$

Then the fraction of the gas mass converted to stars is

$$\epsilon = \epsilon_{core} \int_{x_{crit}}^{\infty} x \frac{dp}{dx} dx \tag{1.10}$$

where ϵ_{core} is the fraction of the gas mass that is not driven away by the outflow from stellar feedback, which is set to be 0.5 in Krumholz & McKee (2005). They also assume the typical timescale to form stars is on the order of the freefall timescale. They then define a new quantity called the SFE per freefall time ϵ_{ff}, which is representative of the fraction of gas converted to stars, as

$$\epsilon_{ff} = \mathrm{SFR} \frac{t_{ff}}{M_{mol}} \tag{1.11}$$

In a turbulence model, $\epsilon_{ff} \approx \epsilon$. Then we can express ϵ_{ff} as

$$\begin{aligned} \epsilon_{ff} &= \epsilon_{core} \int_{x_{crit}}^{\infty} x \frac{dp}{dx} dx \\ &= \epsilon_{core} \left[1 + \mathrm{erf} \left(\frac{-2 \ln x_{crit} + \sigma_{width}^2}{2^{3/2} \sigma_{width}} \right) \right] \end{aligned} \tag{1.12}$$

If ϵ_{ff} is constant for molecular gas, then we would expect that the ratio of $\Sigma_{SFR}/\Sigma_{GMC}$ increases as t_{ff} decreases, which means the SFE in the high Σ_{mol} regime should be larger. On the other hand, the SFE for dense gas traced by HCN is

$$\mathrm{SFE}_{dense} = \frac{\mathrm{SFE}_{mol}}{f_{dense}} \tag{1.13}$$

As the mean density of the gas increases, both SFE_{mol} and f_{dense} increase,

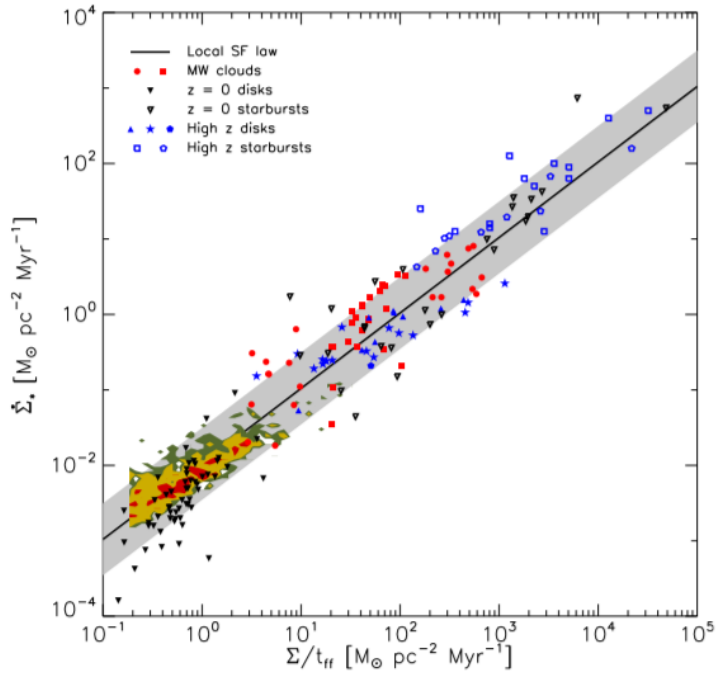

Figure 1.4: Σ_{SFR} versus Σ_{mol}/t_{ff} (Krumholz et al. 2012). Contours represent individual kpc regions in Local Group galaxies. Filled symbols represent the Milky Way clouds (red), local disk galaxies (black) and high-z disk galaxies (blue). The open symbol represents starburst galaxies in local (black) and high-z universe. The solid line represents the best-fit line with $\epsilon_{ff} = 0.01$ and the gray region shows the factor of 3 about that.

which causes SFE$_{dense}$ to be relatively constant.

Krumholz et al. (2012) argue that a ϵ_{ff} of 0.01 can well fit the star formation law in different systems (normal spiral galaxies, local starbursts and high-z starbursts) and scales (GMC and galactic scales) with only a factor of 3 scatter, as shown in Fig. 1.4. They also show that for Milky Way clouds, the GMC freefall time $t_{\mathrm{ff,GMC}}$ is smaller than the galactic freefall time $t_{\mathrm{ff,Gal}}$, which indicates the majority of the molecular gas is in the form of individual GMCs. On the contrary, $t_{\mathrm{ff,GMC}} > t_{\mathrm{ff,Gal}}$ for local and high-z starbursts, which suggests the GMCs have not totally decoupled from the rest of ISM. However, Krumholz et al. (2012) don't have a good measurement of the velocity dispersion for σ_{gas} on both GMC scales and galactic scales. For individual GMCs, they adopt 8 km/s as the value for clouds in the Milky Way and nearby spiral galaxies and 50 km/s for clouds in starburst or high-z galaxies. For the galactic velocity dispersion, they assume the gas Toomre factor Q_{gas} is about 1. As we currently know, Q_{gas} is generally above 1 with the stellar component taken into account (Romeo & Wiegert 2011) if we adopt the measured velocity dispersion.

According to Krumholz & McKee (2005), the scatter in ϵ_{ff} mainly comes from different virial parameters α_{vir} and Mach numbers $\mathcal{M}$. From the fit to the PDF integral, they get ϵ_{ff} to be

$$\epsilon_{ff} \approx 0.014(\frac{\alpha_{vir}}{1.3})^{-0.68}(\frac{\mathcal{M}}{100})^{-0.32} \tag{1.14}$$

However, Lee et al. (2016) find that ϵ_{ff} for local Galactic clouds has a scatter larger by a factor of 0.72 than the theoretical prediction, as shown in Fig. 1.5. Moreover, they find that the fraction of gas converted to stars ϵ has a similarly large scatter. This can be attributed to the change of ϵ_{ff} as a function of the cloud age. Grudić et al. (2019) performed simulations for a single GMC with various masses and Mach numbers and compared the observed $\epsilon_{ff,obs}$ and actual ϵ_{ff}. The simulation shows $\epsilon_{ff,obs}$ clearly increases as the cloud evolves. Furthermore, the scatter in $\epsilon_{ff,obs}$ in the simulation is consistent with previous observations. ϵ_{ff} is also affected by the surface density of the GMC and the median value of 1% suggests the clouds have a narrow range of surface density (Grudić et al. 2018). Semenov et al. (2016) performed this kind of simulation on an isolated Milky Way like galaxy and find that the scatter in ϵ_{ff} on GMC scales can be well produced by the broad distribution of the cloud virial parameter. They also compare their Kennicutt-Schmidt relationship with the observational data and find generally good agreement in kpc scale.

1.4 Disk Stability Analysis

Toomre (1964) derived the local instability criterion to non-axisymmetric perturbations for thin gas disks. This criterion states that when a thin disk region has Toomre factor Q less than 1, it will collapse due to self-gravity. The expression for Q is

$$Q_{gas} = \frac{\kappa \sigma_{gas}}{\pi G \Sigma_{gas}} \tag{1.15}$$

where

$$\kappa = \sqrt{2}\frac{V}{R}\left(1 + \frac{dlnV}{dlnR}\right) \tag{1.16}$$

is the epicyclic frequency, Σ_{gas} and σ_{gas} are the surface density and velocity dispersion of the gas. This is for a disk composed entirely of gas. For a disk of stars, this parameter will become

$$Q_{\star} = \frac{\kappa \sigma_{\star}}{3.36 G \Sigma_{\star}} \tag{1.17}$$

where $\sigma_{\star}$ and $\Sigma_{\star}$ are the radial velocity dispersion and surface density of the stars. Galaxies generally consist of both stellar and gas components. In this situation, Wang & Silk (1994) derived the approximate criterion for the two-component disk, which is

$$Q_{tot} = (Q_{\star}^{-1} + Q_{gas}^{-1})^{-1} \tag{1.18}$$

A more general criterion includes the thickness of the disk, which is shown in

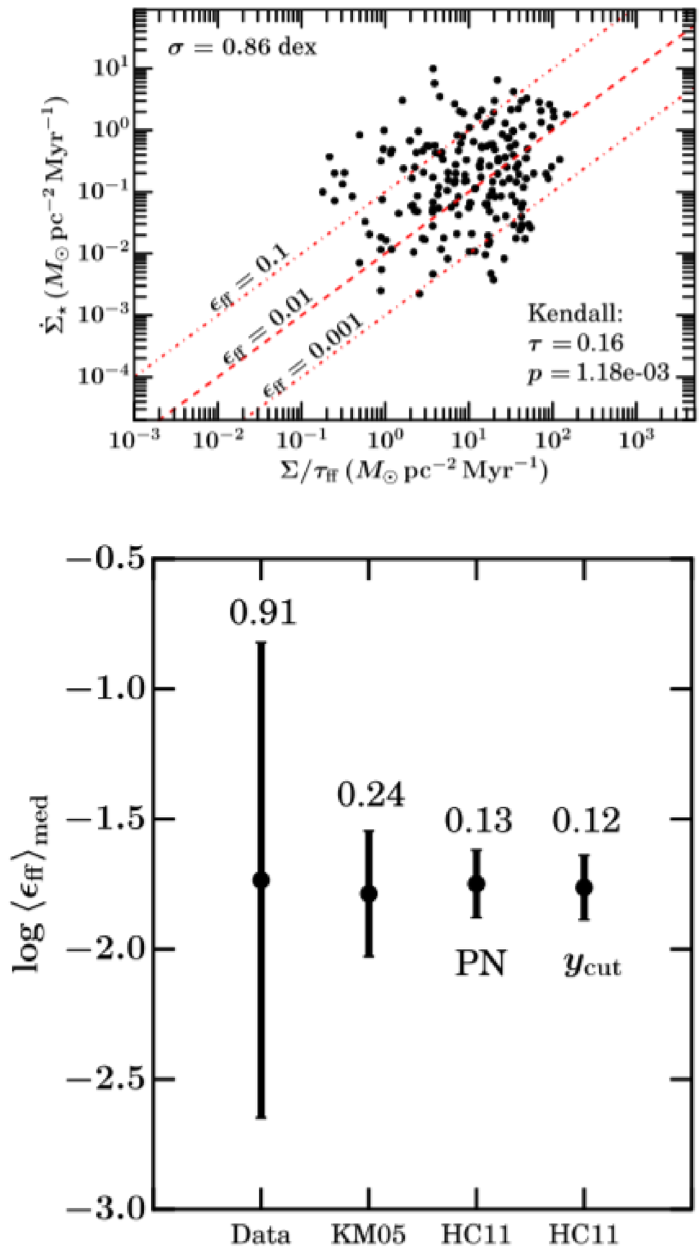

Figure 1.5: ϵ_{ff} measured in Milky Way clouds (Lee et al. 2016). (Upper) Σ_{SFR} versus Σ_{GMC}/t_{ff} for all the Milky Way clouds. The diagonal dashed line indicates constant ϵ_{ff}. (Lower) The comparision of the scatter between measured values and theoretical predications from Krumholz & McKee (2005) (KM05), Hennebelle & Chabrier (2011) (HC11).

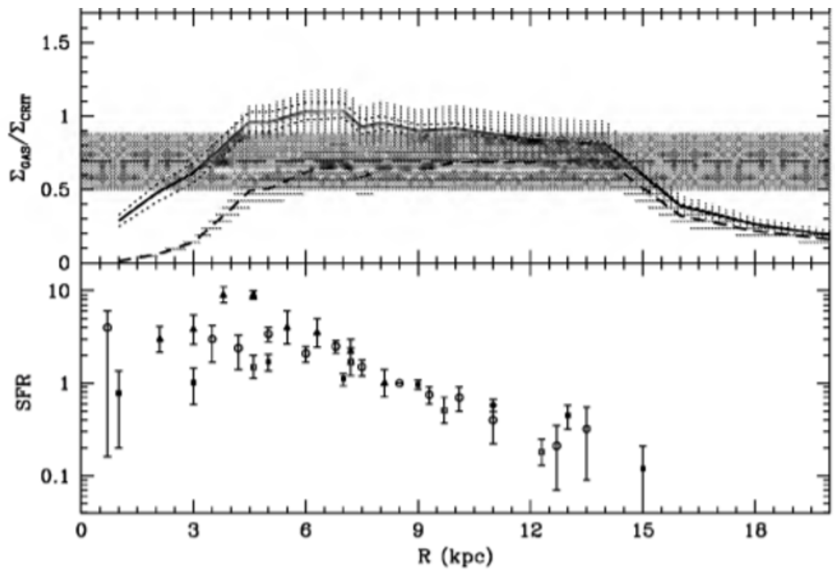

Figure 1.6: Σ_{gas} compared to Σ_{crit} derived from Toomre theory for the Milky Way (Boissier et al. 2003). (Upper) ratio of Σ_{gas} (including H_2 and HI) to Σ_{crit} assuming the Toomre factor Q_{gas} (dashed line) and Q_{tot} (solid line) to be 1.0. The shaded area indicates the value of 0.69 ± 0.2 found in Martin & Kennicutt (2001). (Lower) The SFR radial profile in the Milky Way normalized to the solar neighborhood value.

Romeo & Wiegert (2011). They also checked the approximation and found Q_{tot} generally has an uncertainty of 20% but can reach 40% when $\sigma_{gas} \leq 0.2\sigma_{\star}$ and $Q_{gas} \sim Q_{\star}$.

Self-gravitating instability plays a important role in GMC formation. Current theory favors that GMCs are formed through hierachical collapse from larger gas structures rather than build-up from collisions between small structures (McKee & Ostriker 2007). The instability of large structures can be induced by either Parker instability or Jeans instability. Simulations have shown that Parker instability has difficulty in forming GMC structures due to its limited enhancement of gas density (e.g. Kim et al. 2002). On the contrary, the Jeans instability can keep increasing the gas density. In this case, the Toomre factor sets the condition to trigger instability and we expect to see the

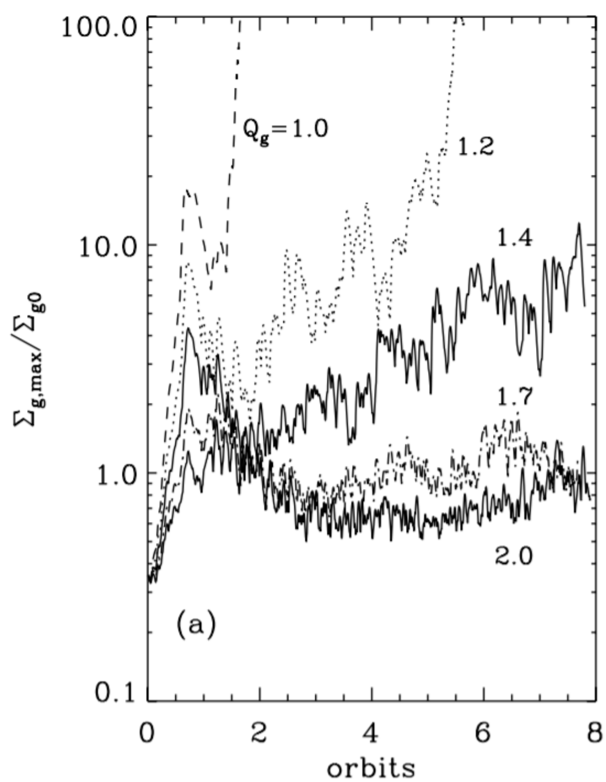

Figure 1.7: Evolution of the maximal value of Σ_{gas} with different values of Q_{gas} for solar-neighborhood like region (Kim & Ostriker 2007). The stellar component and thickness of the disk are taken into account in this simulation.

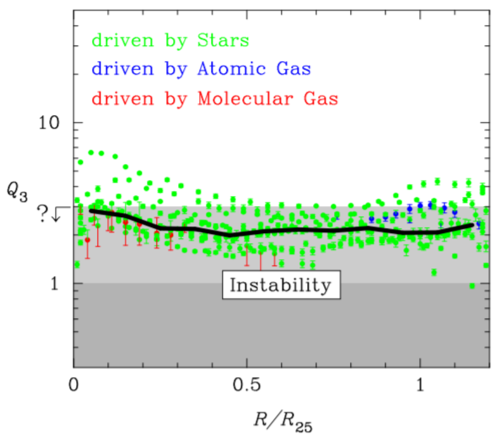

(a)

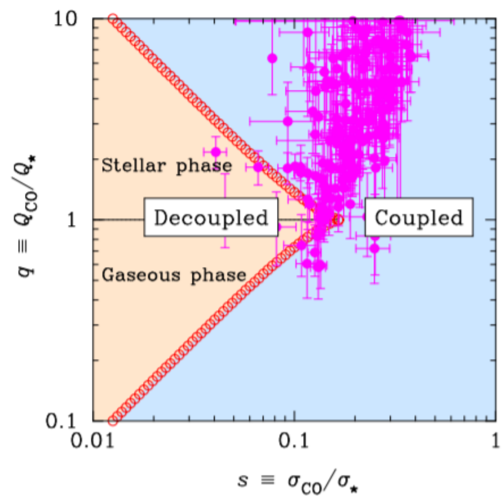

(b)

Figure 1.8: Multi-component Q analysis for nearby spiral galaxies (Romeo & Mogotsi 2017). (Left) The radial profile of three component Q_3 for nearby spiral galaxies. Green, blue and red indicate the Q_3 is mainly brought down by stellar, HI and H_2 component respectively. The deep gray region indicates the parameter space where gas is unstable to axisymmetric perturbations and the light gray region is where gas is unstable to the non-axisymmetric perturbations. (Right) The parameter plane of two-component disc instabilities populated by the data from nearby disk galaxies. σ_{CO} and $\sigma_\star$ are the velocity dispersion of the molecular gas and stars respectively and Q_{CO} and $Q_\star$ are the Toomre factors for molecular gas and stars respectively. Pink points are the data for different regions of the galaxy. The blue shaded region is where the stellar component and gas component are coupled.

SFR cutoff at regions with critical Q values. Boissier et al. (2003) explored this for the Milky Way. They found Q_{gas} is constant (~ 1.4) throughout a large range of radius (4–14 kpc) of the Milky Way assuming the gas velocity dispersion to be constant at 6 km/s, which corresponds to the star forming regions, as shown in Fig. 1.6. They also included the stellar component and got $Q_{tot} \sim 1$ for the star-forming regions, which confirms the Wang-Silk assumption. This is also consistent with simulations from Kim & Ostriker (2007), where they modeled the solar-neighborhood region with different Q_{gas} and $Q_{\star}$. They found $Q_{gas} \sim 1.4$ corresponds to the marginally stable state, as shown in Fig. 1.7. Observations from the Large Magellanic Cloud (LMC) (Yang et al. 2007) also show good correspondence between the star forming regions and regions with $Q_{tot} < 1$. Martin & Kennicutt (2001) explored the SFR cutoff for nearby spiral galaxies with similar assumption of $\sigma_{gas} = 6$ km/s and find that Q_{gas} in the SFR cutoff region is about 1.4, which suggests the stellar component plays an important role. Due to the limited resolution and sensitivity at the time, they could not measure σ_{gas} for different local regions. Romeo & Mogotsi (2017) considered the velocity dispersion from the different components (HI, H_2 and stars) and performed multi-component Toomre factor analysis on nearby spiral galaxies. They found that the major driver for the gas instability is the stellar potential. Furthermore, as shown in the right diagram of Fig. 1.8, most regions have stellar phase and gaseous phase coupled with each other, which suggests that stellar instability can drive the gravitational collapse of the molecular gas.

Leroy et al. (2008) explore the effect of Q on the SFE. The Q_{tot} is centered around 1.6, which is consistent with simulations from Li et al. (2005) for the critical Q_{tot} value. However, there is no correlation between the Q_{tot} and the

SFE. This might tell us that although the Toomre factor Q sets the threshold for SF activity, it doesn't determine how fast gas infalls once this criterion is satisfied. However, we need to keep in mind σ_{gas} in this case is assumed to be a fixed value. Also in this case, the SFE includes the HI component and therefore SFE is mainly dependent on the H_2/HI fraction.

1.5 Molecular Gas and Star Formation in Mergers

In the 1980s, the IRAS satellite was used to identify a new class of objects with extremely high infrared luminosity called LIRGs and ULIRGs (Ultra-/Luminous Infrared Galaxies). Most of these objects have been identified as merging pairs of galaxies with extreme starburst activity (Sanders et al. 1988). Mihos & Hernquist (1996b) simulated the merging process and showed that the inflow of gas towards the center induced by the tidal interaction can cause the starburst activity there. According to the simulations, the most extreme starburst activity happens during the final coalesce of the two galaxies, as shown in Fig. 1.9. During this process, the molecular gas mass in the system decreases quickly, with up to 70% of gas depleted in the end. However, how much gas is left in the end depends on the detailed information of the merging event such as inclination angle and merging pair mass ratio (Cox et al. 2008). Recent simulations (Moreno et al. 2019) considered the multiphase gas evolution during the merging process and try to explore the dependence of SFR on the different phases of gas. They find that the cold dense gas ($n > 10$ cm^{-3}) mass in mergers only has a mass excess of about 18% compared to isolated

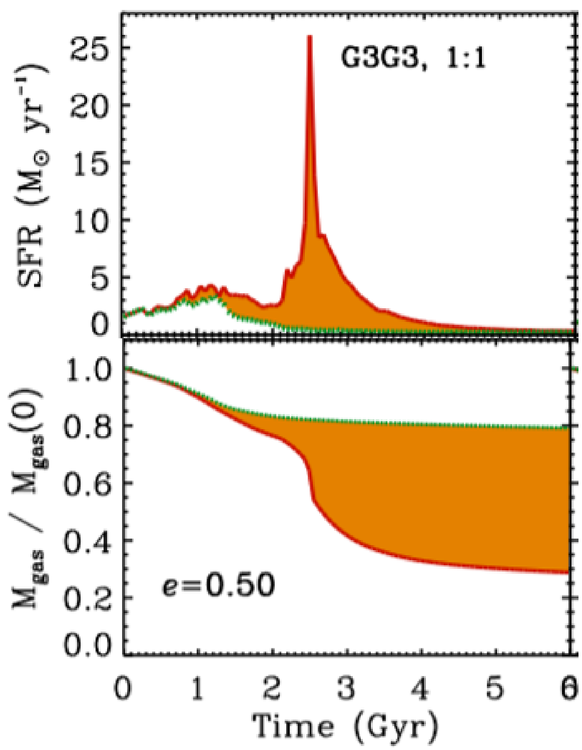

Figure 1.9: The SFR (Top) and gas (Bottom) evolution for a 1:1 major merger as a function of time in simulation (Cox et al. 2008). The green line is the evolution track of the corresponding isolated galaxy for comparison. The orange shaded region indicates the offset between mergers and isolated systems.

systems, which is consistent with observations (Violino et al. 2018). However, the mass excess for ultra-cold dense gas ($n > 10^3$ cm^{-3}) is about 240% averaging over the time between first passage and the final coalesce, which is shown in Fig. 1.10. This might suggest the enhanced SFR in merger systems might be more correlated to the increase in ultra-cold dense gas.

Based on the infrared luminosity measured from the IRAS satellite, Armus et al. (2009) started a Great Observatories All-sky LIRG Survey (GOALS), which studies LIRGs and ULIRGs in the local universe. For now, most of these galaxies have CO observations from the SMA (Wilson et al. 2008) and

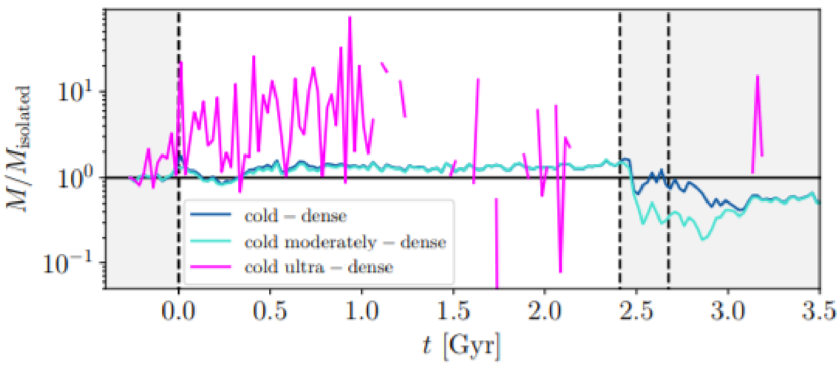

Figure 1.10: The evolution of the gas mass in different phases along the merging process (Moreno et al. 2019). Different lines indicate the evolution track of cold moderately dense gas ($n = 10$–$1000\ \mathrm{cm}^{-3}$, cyan), cold ultra dense gas ($n > 1000\ \mathrm{cm}^{-3}$, magenta) and the total amount of cold gas (blue). The vertical axis is the gas mass ratio relative to the control isolated system.

Nobeyama (Yamashita et al. 2017). These high resolution observations of ^{12}CO have confirmed that for most mergers, the gas is concentrated in the center (e.g. Wilson et al. 2008). Moreover, the gas mass in the central region of mergers is significantly higher than isolated spiral galaxies (Yamashita et al. 2017), as shown in Fig. 1.11. On the other hand, this gas concentration process can cause the conversion of HI gas to H_2 gas, which will increase the molecular gas content during the early stage of the merging process. This has been shown in Larson et al. (2016). Due to the limited size of the GOALS sample, which only contains starburst mergers, people are trying to build a more comprehensive catalogue from large survey data such as the SDSS (Violino et al. 2018; Pan et al. 2018). They found pairs in the sample generally have a higher gas fraction than normal spiral galaxies. On the other hand, the SFE of pairs has no significant difference from that of normal spiral galaxies. However, Ellison et al. (2018) found that post mergers tend to have more HI content than normal spiral galaxies, which seems to be in contradiction with the scenario of

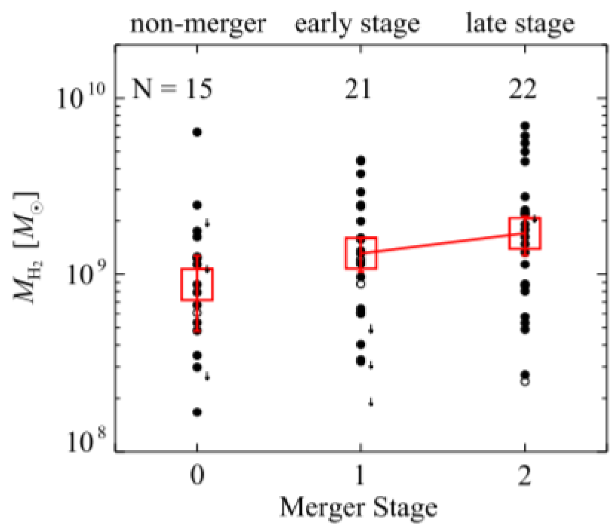

Figure 1.11: Gas mass in the central region of mergers in different stages (Yamashita et al. 2017). Number 0, 1 and 2 indicates non-merger, early merger and late merger respectively. The red square indicates the median value of the detected regions.

HI converted to H_2. They argue that the major reason for enhanced HI mass is caused by the effect of the arithmetic sum of HI mass from two galaxies. Generally for both post-mergers and normal spiral galaxies, the HI gas fraction decreases as the stellar mass increases. When two galaxies merge into one, the HI gas fraction should remain the same while the stellar mass increases. Therefore, compared to normal spiral galaxies with similar stellar mass, the post-mergers will have higher HI gas fraction. However, there are still effects from many other factors to be explored. Furthermore, they argue that these HI rich post mergers suggest the starburst activity in mergers is terminated by turbulence instead of gas exhaustion.

Another important aspect is to explore how the gas properties, such as temperature and density, evolve and how these quantities affect the star forming activity in the system. A commonly used method for modeling gas properties is LVG modeling, which allows different excitation temperatures for different transitions. The modern tool used for this kind of modeling is RADEX (van der Tak et al. 2007). Many studies have applied this modeling to LIRGs and ULIRGs in the GOALS sample (Sliwa et al. 2017, and references there in). Most of those analyzed objects are in the intermediate and late stage of merging. Most studies show those systems have typical ULIRG α_{CO} (0.8 $M_\odot$ (K km s^{-1} pc^2)$^{-1}$). According to Narayanan et al. (2011), the conversion factor will drop first to the typical ULIRG value and then come back to the Milky Way value after two galaxies finally coalesce. According to this scenario, we would expect the early mergers to tend to have $\alpha_{\rm CO}$ in between the Milky Way value and the ULIRG value. On the other hand, these intermediate and late stage mergers have extreme [^{12}CO]/[^{13}CO] ratios, which is either caused by the inflow of high [^{12}CO]/[^{13}CO] gas towards center, or a top heavy initial mass function (IMF) during the starburst stage that causes the over abundance of ^{12}CO. Sliwa et al. (2017) studied one early merger Arp 55. They found for the center of this system, while it still has typical ULIRG $\alpha_{\rm CO}$ the [^{12}CO]/[^{13}CO] ratio is more likely to be 15 $\sim$ 30, which is closer to the value of the Milky Way center. They also find in this early stage merger, the gas tends to be denser ($> 10^3$ cm^{-2}) and colder ($\sim$ 10 K). Moreover, the thermal pressure of this system tends to be higher than that of late stage mergers. Possible scenarios include that the stellar feed back pushes the molecular gas out to larger volumes or the H_2 gas is more consumed than replenished.

Although most mergers have starburst activity in the center, some mergers are found to have off-center starburst activity such as the Antennae and NGC 5258 (Wilson et al. 2008). One scenario for the off-center starburst is that it is caused by tidally induced compressive turbulence (Renaud et al. 2009). In general turbulence models, the cloud density PDF is in the form of a log normal distribution function, with the width of the PDF set by

$$\sigma_{width}^2 = ln(1 + (1 - 2\zeta/3)^2 \mathcal{M}^2) \tag{1.19}$$

where $\mathcal{M}$ is the Mach number of the clouds. ζ is the coefficient determined by the composition of the turbulence mode in the GMC. The turbulence mode can be generally decomposed into a compressive mode and a solenoidal mode. $\zeta = 0$ when the turbulence is fully compressive and $\zeta = 0.5$ when the compressive mode and solenoidal mode reach the equipartition. Therefore, when the cloud turns from equipartition mode to fully compressive mode, the PDF of the cloud is broadened and more gas is squeezed into the dense regime. Therefore, more dense gas is available to form stars. Renaud et al. (2009) simulated a major merger similar to the Antennae and found that the fraction of the gas in the compressive mode rises by a factor of $4 \sim 13$ when colliding or passing each other, which is consistent with the global SFR enhancement in the simulation of Di Matteo et al. (2008). Teyssier et al. (2010) further explored these simulations on GMC scales and found that the high resolution simulation (12 pc) gives significant enhancement in total SFR compared to the low resolution simulation (96 pc), which demonstrates the high SFR enhancement is caused by the increase of dense gas fraction due to the compressive turbulence. The increase in dense gas fraction will also give us a shorter depletion time for the merging system, which is closer to the typical (U)LIRG depletion time ($\sim 10^8$ yrs). Renaud et al. (2014) further explored how the increase in the fraction of the compressive mode would broaden the PDF, as shown in Fig. 1.12. As turbulent energy increases, the compressive mode gradually overcomes the solenoidal mode. In that case, the PDF will broaden much more quickly. They

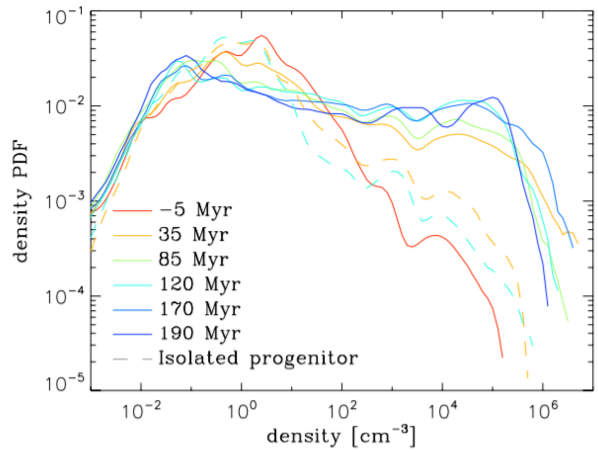

Figure 1.12: The PDF of the gas density in different stages of the merging process (Renaud et al. 2014).

also explored how the SFE evolves in the merging process, as shown in Fig. 1.13. Right before the first passage, the dense gas fraction is increased by the compressive mode overcoming the solenoidal mode while the inflow hasn't increased the Σ_{gas} yet. After the second passage, Σ_{gas} increases and boosts up the SFE again.

Arp 240 is identified as a Luminous Infrared Galaxy (LIRG). Like most LIRGs, it is a merging system including two massive spiral galaxies, NGC 5257 and NGC 5258. The two galaxies are intertwined in HI (Iono et al. 2005) but well separated in optical images. The projected distance of the two galaxies is about 40 kpc. Simulations (Privon et al. 2013) show the two galaxies are in the early stage of the merging process and have just been through first passage.

1.6 Outline of This Thesis

In the following chapters, we will focus on this particular early merger Arp 240. We mainly use the CO line data from Atacama Large Millimeter/Submillime-

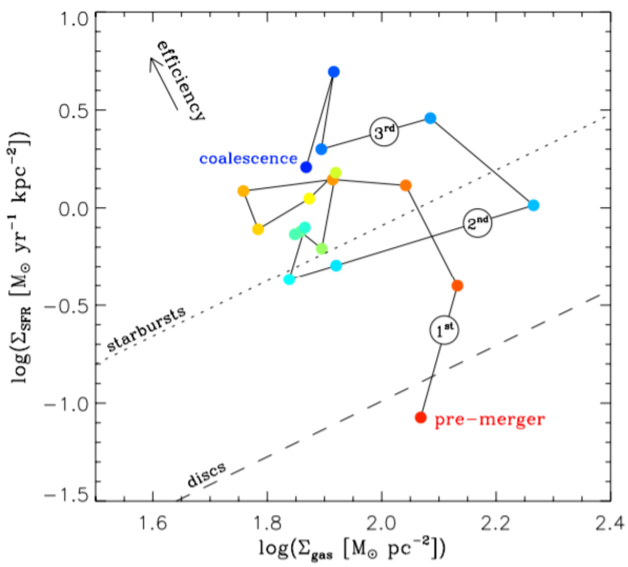

Figure 1.13: The simulation of Σ_{gas} and Σ_{SFR} inside the half mass radius of the galaxy (Renaud et al. 2014). The color indicates the time from early (red) to late (blue). The number of circles indicates each encounter between two galaxies.

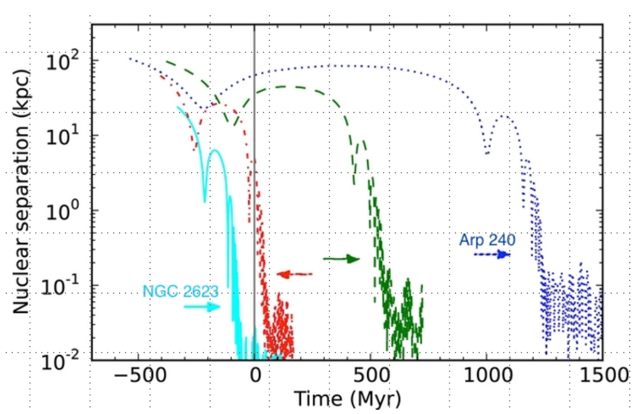

(a)

Figure 1.14: The simulated results of the nuclear separation as a function of time for several merging systems (Privon et al. 2013). The time t=0 Myrs identifies the current viewing time. From the graph we can see Arp 240 has just been through first passage.

ter Array (ALMA) to study the molecular gas properties in different regions of this system. We will further compare the derived molecular gas properties with other observed quantities such as stellar mass (SM) and SFR. Our major goal in this research is to study how SF activity is related to different properties of the molecular gas.

In Chapter 2 we summarize the basic information of the ALMA CO observations and steps to make the spectral line image. In Chapter 3 we describe our analysis on the CO data and present our major science results, including RADEX modeling of the gas properties, disk stability analysis and testing turbulence regulated star formation models. This chapter is a paper in progress and there will be some repetition of content from Chapter 1 and Chapter 2. In Chapter 4 we supplement our disk stability analysis with kinematic modeling of the two galaxies using CO line data. In Chapter 5 we discuss our major findings and the future direction for general study of mergers.

Chapter 2

Observations and Data Reduction

2.1 Spectral and Spatial Setup

The data is from project 2015.1.00804.S (principal investigator (PI): Kaz Sliwa) observed during 2016 with ALMA. It contains data from Band 3 and Band 6. We were mostly interested in constraining molecular gas properties and therefore we mainly use the CO spectral line data. Band 3 covers ^{12}CO J=1-0 (115 GHz) and ^{13}CO J=1-0 (110 GHz) and Band 6 covers ^{12}CO J=2-1 (230 GHz). Both the ^{12}CO J=1-0 and J=2-1 observations include 12m Array and 7m Atacama Compact Array (ACA) data while ^{13}CO J=1-0 only contains 12m array data. The total usable bandwidth for each of the spectral windows (SPW) was 1875 MHz for the 12m array and 2000 MHz for the 7m array. The width of a single channel is 1.953 MHz.

Band 3 data uses the single pointing observing mode. In contrast, Band 6 uses multiple pointings for each field, which is called mosaic pointings. The

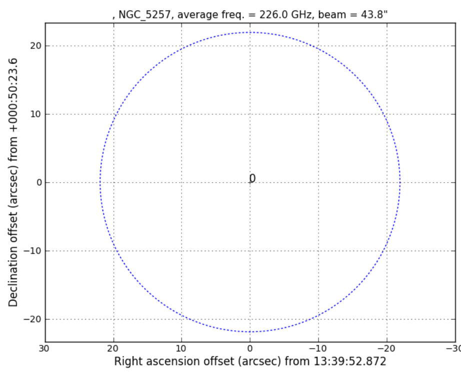

(a)

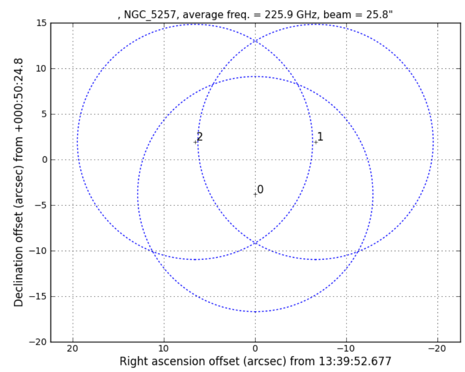

(b)

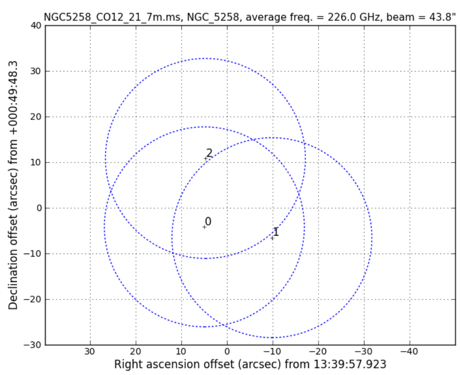

(c)

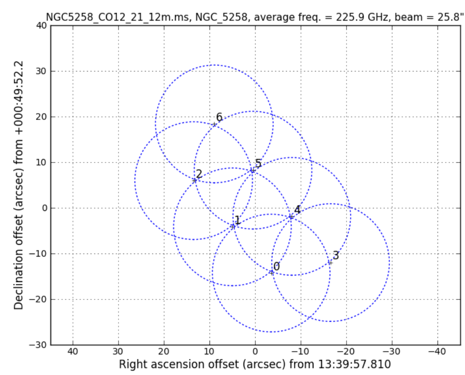

(d)

Figure 2.1: Mosaic pointings for Band 6 data of NGC 5257 (top) and NGC 5258 (bottom). The left column is the pointings for the ACA and the right is the pointings for the 12m array.

pointing sets for the two fields are shown in Fig. 2.1.

2.2 Imaging

2.2.1 General Process

The data we are dealing with has already been calibrated by the script provided by the observatory. We then proceed to the imaging step with Common Astronomy Software Applications (CASA) as our analysis tool.

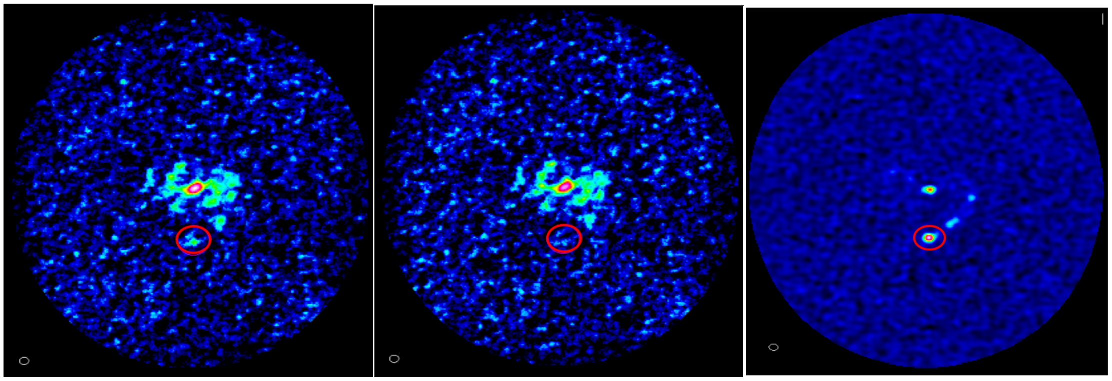

(a) (b) (c)

Figure 2.2: Demonstration of continuum subtraction effect for ^{13}CO J=1-0 moment 0 map. (Left) ^{13}CO J=1-0 moment 0 map without continuum subtraction. (Middle) ^{13}CO J=1-0 moment 0 map with continuum subtraction. (Right) The continuum image in ^{13}CO J=1-0 band. We can see the south continuum source, which is enclosed by the red aperture, contributes a fair amount of flux in the ^{13}CO J=1-0 line emission map before continuum subtraction is applied.

The project contains ^{12}CO J=1-0 and ^{12}CO J=2-1 data from both the 7m and the 12m array. To recover the flux on both large scales and small scales, we combine the 7m and 12m measurement set (MS) files with the command `uvcombine`. Then we proceed with the continuum subtraction for all three lines. We made dirty line images, which still contain noise and sidelobes from the observation, with the `tclean` command for both continuum subtracted and non subtracted MS files. To compare images made from those two datasets, we made moment 0 maps with the command `immoments`. For NGC 5257, we can see a clear difference in flux towards the south continuum source between the ^{12}CO J=1-0 and ^{13}CO J=1-0 moment 0 map. To check if the missing flux is due to continuum radiation from the source, we made continuum dirty images of NGC 5257 for ^{12}CO J=1-0 and ^{13}CO J=1-0 with the command `tclean` with specmode set to "mfs". It turns out ^{12}CO J=1-0 and ^{13}CO J=1-0 have a strong continuum source in the missing flux region (see Fig. 2.2). We also tried to make the continuum image at ^{12}CO J=2-1 wavelength but we don't have any continuum detection in the dirty continuum image.

As we have made the dirty image cubes for all three lines, we can also measure the root-mean-square (RMS) noise of the image cube. We will generally clean the image cube until the peak signal in the residual cleaned cube is below 2 times the RMS noise. We also use the `auto-multithresh` function in `tclean`. This function contains four major parameters, noisethreshold, sidelobethreshold, lownoisethreshold and negativethreshold. The negativethreshold is applied to absorption lines and therefore we set it to be 0. The basic principle is shown in Fig. 2.3. The first step is to pick the signal from the image cube. The signal should be both above the noisethreshold and the sidelobethreshold times the RMS noise. Any signal region with area smaller than the beam size is then pruned, as shown in Fig. 2.3 (a). Then the signal is extended to neighboring regions which are above the lownoisethreshold times the RMS noise. The last step is to trim the detected signals. The detected signal is then Fourier transformed backed to the uv visibility and stored as the modeled signal in the original visibility file. In each cycle, only a fraction of the signal is cut and stored in the model and it proceeds with multiple cycles. Generally we find that the noisethreshold affected the image quality the most. Therefore, we generally keep the other parameters at their default values while tweaking the noisethreshold to ensure it finally masked all the signal regions. For ^{12}CO J=2-1 specifically, the cleaned image will have a severely anomalous cleaned region at the edge of the field. By checking the dirty map of the ^{12}CO J=2-1 image, we find the noise level at the edge is significantly higher and is probably caused by sidelobes in the observation. Therefore, we raise our side-

Table 2.1: Auto-multithresh parameters

		noisethreshold	sidelobethreshold
NGC 5257	^{12}CO J=1-0	4.5	3.0
	^{13}CO J=1-0	4.2	3.0
	^{12}CO J=2-1	4.0	4.0
NGC 5258	^{12}CO J=1-0	4.5	3.0
	^{13}CO J=1-0	4.5	3.0
	^{12}CO J=2-1	4.5	4.0

lobethreshold and successfully solve this problem. The different parameters for the auto-multithresh function are shown in Table 2.1.

After getting the cleaned image cubes, we can make the moment 0, 1, 2 maps with the command texttttimmoments. We set the moment 0 map cut to be 2 times the RMS noise and moment 1, 2 map cuts to be 4 times the RMS noise. We also make moment 1 and 2 maps with the script from Sun et al. (2018). The feature of this script is to select signals in more than two consecutive channels, which will reduce the pixels with inaccurate velocity dispersion measurements.

2.2.2 Ratio Map

To make the ratio map between the different line images, we need to make sure all the line images have the same uvcoverage and beam size. We use the `plotms` command to look at the uvcoverage of the different line images. To reduce the time for the command, we run this command on a single velocity channel of the ms file. We can see ^{12}CO J=2-1 has a lower limit of the uvrange of about 6 kλ while ^{12}CO J=1-0 and ^{13}CO J=1-0 has lower limits about 3 kλ, as shown in Fig. 2.4. We use the command `uvrange` to cut the ^{12}CO J=1-0 and ^{13}CO J=1-0 uvdata below 6 kλ. We then use the command `uvtaper`

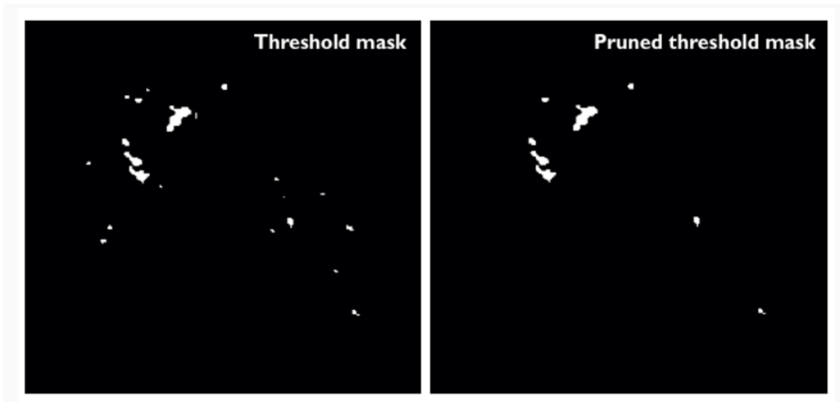

(a)

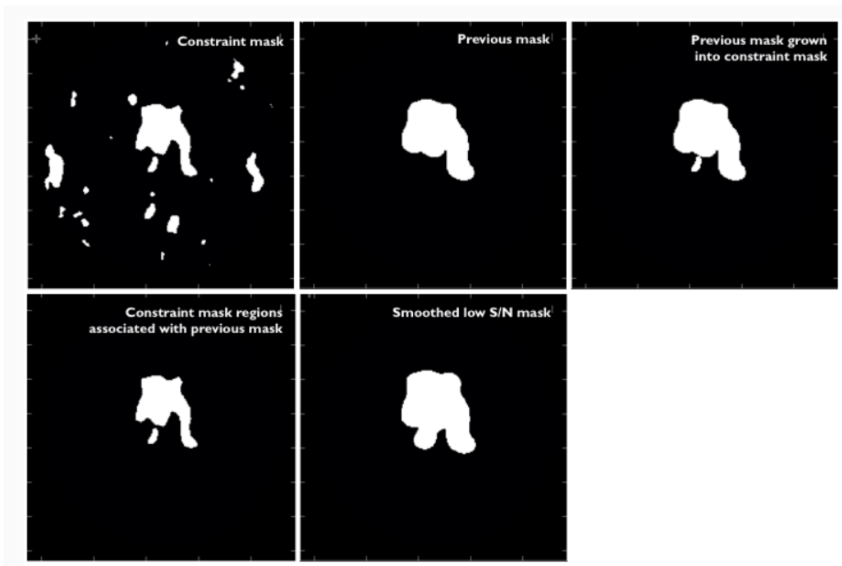

(b)

Figure 2.3: The illustration of how auto-multithresh works (Masks for Deconvolution 2017, https://casa.nrao.edu/casadocs/casa-5.1.0/synthesis-imaging/masks-for-deconvolution). Diagram (a) shows how masked regions with area smaller than the beam size are pruned in the auto-multithresh function. The left is the masked signal region and the right is the pruned masked signal region. Diagram (b) shows how the signal region is expanded to lower signal-to-noise (S/N) regions. The top left is the constraint mask of regions with signal above the lownoisethreshold. The top middle is the final mask from the previous clean cycle. The top right is the mask from previous clean cycle expand into regions in constraint mask where the region is associated with the previous mask. The bottom left is the expanded mask multiplied with the top left constraint mask to pick out only the signal region in the constraint mask. The bottom middle mask is the final pruned, smoothed mask from the bottom left mask.

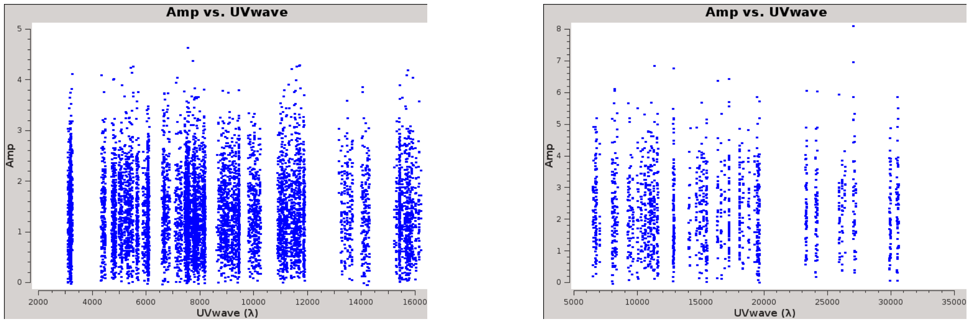

(a) (b)

Figure 2.4: Lower end of uvcoverage for (a) ^{12}CO J=1-0 and (b)^{12}CO J=2-1. We cut the short uvrange for both lines to be above 6 kλ.

to make the image beam of ^{12}CO J=2-1 similar to that of ^{12}CO J=1-0 and ^{13}CO J=1-0. The uvtaper function basically applies a normalized 2D Gaussian distribution function to the weight of visibility file. Therefore, the data from the outer part of the array is less weighted and thus the beam size is increased. To select the Gaussian function for the uvtaper, we use the CASA command `ia.beamforconvolvedsize`. As we know, the image is Fourier-Transformed from the uv visibility file. Therefore, multiplication in the visibility file is the convolution function in the image. Therefore, the uvtaper beam should be similar to the smooth beam to convolve the image to the target beam. After cutting the short uvrange and applying the uvtaper, the beams of the 3 lines are still not exactly the same. Therefore, we need to apply the CASA function `imsmooth` to make the beam size of the 3 lines to be exactly the same.

After making the 3 line cubes to have the same beam, we can then start to make ratio maps between the different lines. We first make the moment 0 map of all 3 lines with a certain cutoff. The cutoff is decided by the different line ratio maps we make. For ^{12}CO/^{13}CO 1-0 ratio, we applied a cut of 2 times the RMS of the ^{13}CO J=1-0 cube for making ^{13}CO J=1-0 moment 0 map. We

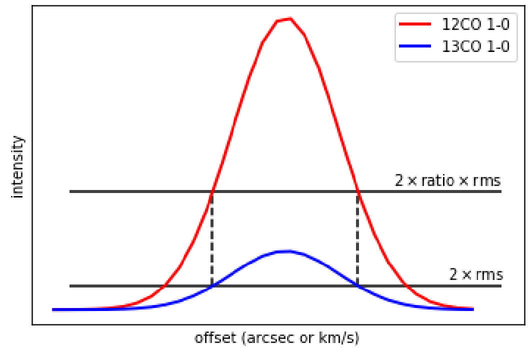

(a)

Figure 2.5: Illustration of the principle to determine the cutoff to make the ^{12}CO/^{13}CO 1-0 ratio map based on the ratio between the two maps. The red and blue line indicate the ideal Gaussian distribution of the ^{12}CO J=1-0 and ^{13}CO J=1-0 intensity distribution on spatial or spectral axis. The two horizotal lines indicate the cutoff for ^{12}CO J=1-0 and ^{13}CO J=1-0 with this method. As we can see both lines extracted via this method have the same spectral or spatial coverage.

also applied the cut of 2 RMS of the ^{12}CO J=1-0 cube for the ^{12}CO J=1-0 moment 0 map. We then calculated the total flux ratio between ^{12}CO J=1-0 and ^{13}CO J=1-0. We adopted this ratio as the typical ratio of ^{12}CO/^{13}CO 1-0 for this system. We then applied the cut of 2 times the ratio times the RMS of ^{13}CO J=1-0 cube as the cutoff of ^{12}CO J=1-0 moment 0 map cutoff. Based on this principle, we make sure we select the signal from both lines within same spatial range and velocity range, as shown in Fig. 2.5. For the ^{12}CO 2-1/1-0 ratio map, we applied the same method. However, because the 2 RMS cut for the ^{12}CO J=1-0 cube is relatively sensitive and meanwhile, the ^{12}CO 2-1/1-0 temperature ratio is close to 1.0. The cutoff for the ^{12}CO J=2-1 map is not high enough to exclude all the noise. Therefore, to exclude the noisy pixel in the outer region, we applied a region mask to include pixels only within the galaxy. The ratio maps are shown in Fig. 3.6.

Chapter 3

Arp 240

This chapter was prepared as a paper, and will be submitted for publication in the Monthly Notices of the Royal Astronomical Society. It contains a short introduction and an abbreviated discussion of the data reduction in this work. Although some of the material overlaps with material in earlier chapters, the earlier chapters serve as a complete and detailed account of the research background and data reduction methods.

3.1 Introduction

In the 1980s, the IRAS satellite was used to identify a new class of objects with extremely high infrared luminosity called LIRGs and ULIRGs (Ultra/Luminous Infrared Galaxies). Most of these objects have been identified as merging pairs of galaxies with extreme starburst activity (Sanders et al. 1988). As a laboratory for star formation (SF) in extreme environments, many of these mergers have been studied in molecular gas (as traced by CO) at high resolution (e.g. Wilson et al. 2008; Sliwa et al. 2017). However, most of these studies have focused on intermediate or late-phase mergers, with few observations of early-stage mergers when the two galaxies are still well separated (d_{proj} > 40 kpc). These objects are gaining increasing attention in statistical studies for understanding galaxy evolution along the merging sequence. According to many studies (e.g. Violino et al. 2018; Pan et al. 2018), the average star formation efficiency (SFE=SFR/M_{H_2}) is not enhanced significantly as the projected distance decreases, and so the major enhancement seen in the SFR is attributed to an increase of H_2 gas mass. However, the large scatter seen in the SFE could hide a dependence on the physical properties of the molecular gas. To fully understand the merging process, we need to have more resolved studies focused on the molecular gas environment in early mergers.

Simulations have shown that the inflow of gas caused by tidal interactions will trigger a starburst in the center of the galaxy (Mihos & Hernquist 1996a), which is observed in most cases. However, some mergers, such as the Antennae (NGC4039/39), show an off-nuclear starburst. High resolution (1 pc scale) simulations show that compressive turbulence is responsible for this off-center starburst location (Teyssier et al. 2010; Renaud et al. 2014). Unlike normal spiral galaxies, which have $\Sigma_{mol} \sim \Sigma_{SFR}$, the Kennicutt-Schmidt law becomes superlinear in these starburst galaxies with high Σ_{mol} (Daddi et al. 2010). Usero et al. (2015) found that while the depletion time t_{dep}= 1/SFE decreases as Σ_{mol} increases, the depletion time for dense gas, which is traced by HCN emission, stays almost constant in the whole range of Σ_{mol}. This could be explained by turbulence models (Krumholz & McKee 2005). In this model, the turbulence will set the probability density function (PDF) of the clouds. Only the dense part of the cloud will collapse and form stars on the time scale of the cloud freefall time. In this model, the fraction of gas to form stars could be represented by the SFE per freefall time, which is

$$\epsilon_{ff} = \frac{t_{dep}}{t_{ff}} \tag{3.1}$$

Krumholz et al. (2012) argued that ϵ_{ff} should be 2% on all scales with only a factor of 3 scatter. However, Lee et al. (2016) calculate ϵ_{ff} for local Galactic clouds and find that the scatter in this quantity is larger by a factor of 0.72 with a maximal value of several 10%. Semenov et al. (2016) found that the distribution of cloud virial parameters is broad enough to account for the observed scatter of ϵ_{ff} for an individual galaxy. Overall, ϵ_{ff} still seems to be highly dependent on the environment. Therefore, we need to explore the molecular gas properties in detail to understand star formation in these regions.

Since the amount of molecular gas cannot be traced directly by H_2, we generally use the ^{12}CO J=1-0 emission to trace the amount of molecular gas. This will introduce the conversion factor $\alpha_{\rm CO}$ between the surface density of the molecular gas and the ^{12}CO J=1-0 intensity. $\alpha_{\rm CO}$ in the Milky Way is found to be 4.3 $\rm M_{\odot}pc^{-2}(Kkms^{-1})^{-1}$ (Bolatto et al. 2013). In LIRGs and ULIRGs, the typical conversion factor is found to be smaller, with a typical value of 1.1 $\rm M_{\odot}pc^{-2}(Kkms^{-1})^{-1}$ (Downes & Solomon 1998, including Helium). Narayanan et al. (2011) explored the difference in conversion factors between mergers and normal disk galaxies in simulations. They found $\alpha_{\rm CO}$ will decrease as merging starts and then eventually come back to the Milky Way value as the merging event finishes. They also found the rise in velocity dispersion and temperature in combination is what causes the conversion factor to be lower than the Milky Way value by factor of 2 to 10. Papadopoulos et al. (2012) further point out that the major reason for small $\alpha_{\rm CO}$ in LIRGs and ULIRGs is the large velocity dispersion. However, the cause of the low conversion factor in these systems is still under debate.

One of the tools to constrain the molecular gas properties as well as the conversion factor is RADEX modeling (van der Tak et al. 2007). To perform this kind of analysis, we need multiple CO lines. This kind of analysis is typically performed over entire galaxies with large beams (e.g. Kamenetzky et al. 2016). With the help of ALMA, we can perform this kind of analysis in resolved regions of individual galaxies (e.g. Saito et al. 2017; Sliwa & Downes 2017). These studies enable us to make a direct comparison between mergers in different stages. Sliwa et al. (2017) compared the early stage merger Arp 55 with the late stage merger NGC 2623. They found that for an early merger like Arp 55, the conversion factor is still well below the Milky Way conversion factor. They argue that Arp 55 is not an early enough merger to catch the transition of α_{CO} from the Milky Way value to the ULIRG value. A study of an even earlier merger will help us to explore this problem.

In this chapter, we study Arp 240, which is an even earlier merger than Arp 55. Arp 240 is composed two massive spiral galaxies, NGC 5257 and NGC 5258. The two galaxies are intertwined in HI (Iono et al. 2005) but well separated in optical images. The projected distance of the two galaxies is about 40 kpc. Simulations (Privon et al. 2013) also show the two galaxies are in the early stage of the merging process and have just been through the first passage. Basic information on Arp 240 is listed in Table 3.1. In studying this system, we hope to get a better understanding of the star formation activity and gas physical properties in an early merger system.

This chapter is organized as follows. In Section 2, we describe basic information on the observations and how we processed the data. In Section 3,

Table 3.1: Basic Information for NGC 5257 and NGC 5258

	NGC 5257	NGC 5258	# References
Coordinates (J2000) [a]	ra= $13^h39^m52.91^s$	ra= $13^h39^m57.70^s$	...
	dec=$+00°50'24.5''$	dec=$+00°49'51.1''$	...
Morphological Type [b]	SAB(s)b pec	SA(s)b:pec	...
Redshift [b]	0.022676	0.022539	...
Luminosity Distance (Mpc)	98.0	97.4	1
$L_{H\alpha}$ ($10^6 L_\odot$)	5	6	2
L_{TIR} ($10^{11} M_\odot$) [c]	1.3	1.5	This work
HI mass ($10^{10} M_\odot$)	1.2	0.98	3
H_2 mass ($10^9 M_\odot$) [d]	2.6	4.8	This work
Stellar Mass ($10^{10} M_\odot$) [e]	9.4	10.5	This work
SFR ($M_\odot$ yr^{-1}) [f]	27.8	24.9	3,4

Notes. [(a)]HyperLEDA. [(b)]NED. [(c)]From the combination of 24 um image from Spitzer and 70 um from Herschel. [(d)]From the ^{12}CO J=1-0 ALMA observation assuming ULIRG conversion factor. [(e)]From the 3.6um and 4.5um Spitzer data. [(f)]From $L_{1.4\mathrm{GHz}}$.

References. (1) Mould et al. (2000); (2) Sofue et al. (1993); (3) Iono et al. (2005); (4) Yun et al. (2001)

we report our measurements of several quantities, such as gas mass, line ratio, and SFR in different regions. In Section 4, we performed RADEX analysis to explore the gas physical properties and conversion factors in different regions. In Section 5, we use ^{12}CO J=2-1 data and 33 GHz continuum data to explore the relationship between molecular gas and SFR under the framework of the turbulence model. In Section 6, we discuss our overall analysis of calculating α_{CO} and ϵ_{ff} and what these values indicate.

3.2 Observations and Data Reduction

We use multiple CO lines (^{12}CO J=1-0, J=2-1 and ^{13}CO J=1-0) from ALMA to determine the physical properties of the gas in Arp 240. To further constrain the properties of the gas, we add ^{12}CO J=3-2 data from the Submillimeter

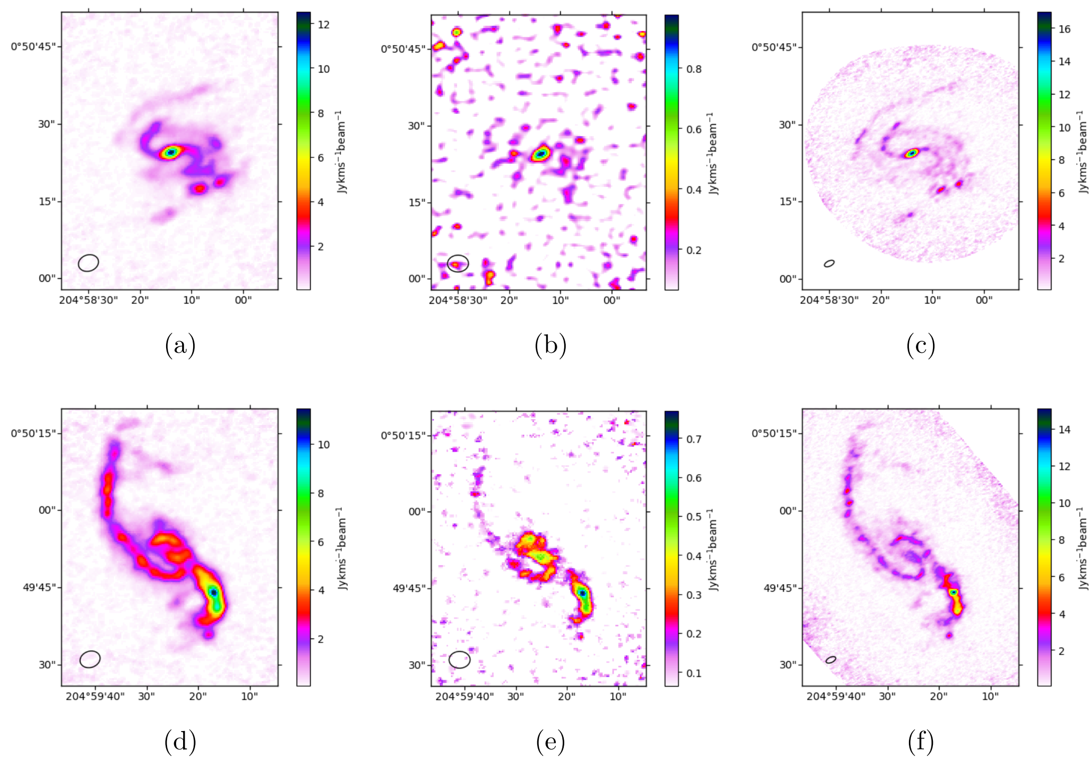

Figure 3.1: From left to right are the moment 0 of ^{12}CO J=1-0 ^{13}CO J=1-0 and ^{12}CO J=2-1 for NGC 5257 (top panel) and NGC 5258 (bottom panel). The black ellipse in each plot indicates the size of the beam.

Array (SMA). The SFR is traced by infrared data and radio continuum. We use the 24 um map from Spitzer, the 70 um map from Herschel, and 33 GHz continuum map from the VLA to trace the SFR.

3.2.1 ALMA Data

The data for Arp 240 was acquired from project 2015.1.00804.S (PI: Kaz Sliwa). Arp 240 was observed in 2016 as a filler project in ALMA cycle 3 with both the 12m array and 7m array. The Band 3 data were observed in configuration C36-3 and the Band 6 data were observed in configuration C36-5. Single pointings were used for the Band 3 data. For the Band 6 data, four

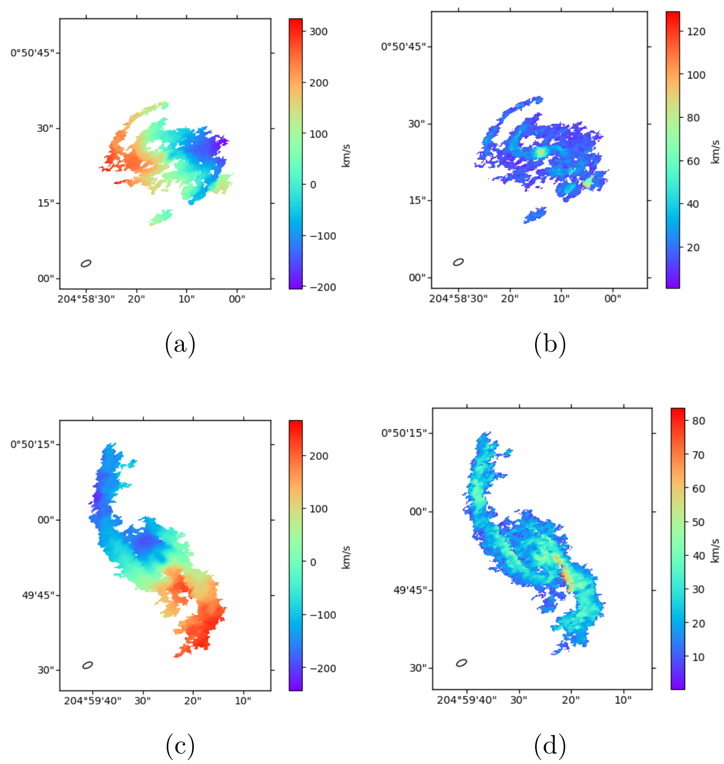

(a) (b)

(c) (d)

Figure 3.2: Velocity field and dispersion map of NGC 5257 (top panel) and NGC 5258 (bottom panel) derived from the ^{12}CO J=2-1 data cube.

pointings were used for NGC 5257 while 9 pointings were used for NGC 5258. The resolution of Band 3 is about 2 arcsec (1 kpc) while the resolution of Band 6 is about 1 arcsec (0.5 kpc). Band 3 covers ^{12}CO J=1-0 (112 GHz) and ^{13}CO J=1-0 (108 GHz) and Band 6 covers ^{12}CO J=2-1 (223 GHz). The total usable bandwidth for each of the spectral windows was 1875 MHz for 12m array and 2000 MHz for 7m array. The width of a single channel is 1.953 MHz.

The original reduction scripts were used to calibrate the raw data using the appropriate CASA version 4.5.0. We use CASA 5.1.1 to select line free channels and subtract the continuum from the line cubes using `uvcontsub` command. All imaging steps were carried out in CASA 5.4.0. We used the command `tclean` and set the channel width to be 10 km/s for ^{12}CO J=1-0 and ^{12}CO J=2-1 and 20 km/s for ^{13}CO J=1-0 to achieve better sensitivity. The total velocity range is set to be 500 km/s. For cleaning, we set the threshold to be 2 times the RMS noise. We use the auto multithreshold option in the `tclean` command to identify clean regions automatically. There are four key parameters: noisethreshold, sidelobethreshold, lownoisethreshold and negativethreshold. We generally use the default setting except for ^{12}CO J=2-1. We found strong sidelobes at the edges of the ^{12}CO J=2-1 map for NGC 5257 and therefore we set the sidelobethreshold to be 4.0 instead of the default 3.0. To make the line ratios (Section 3.3), we use the `uvtaper` option in `tclean` to make the ^{12}CO J=2-1 image with a similar resolution as ^{12}CO J=1-0. We also cut the short uvrange of ^{12}CO J=1-0 to make both data cubes have the same uvcoverage.

After imaging, we created moment 0 maps using the CASA command `immoments` with threshold of 2 RMS for each image cube. For the moment 1 and 2 maps, we use the script from Sun et al. (2018). This script identifies detections with S/N >5 for 3 consecutive channels and then expands to the neighboring pixels with S/N>2 for at least two channels. In this way, we can avoid selecting pixels with a single channel detection, which could lead to extreme values in the velocity field and dispersion measurements.

Table 3.2: Summary of ALMA molecular line observations

Molecular line	RMS noise (mJy/beam)	Beam (")	Configuration	Field Mode	Channel Width (km/s)	Observed Frequency (GHz)
^{12}CO J=1-0	1.6	2.0 × 1.6	12m+7m array	Cycle 3	10	112.73
^{12}CO J=2-1	3.0	1.0 × 0.5	12m+7m array	Cycle 3	10	225.46
^{13}CO J=1-0	0.64	2.1 × 1.6	12m array	Cycle 3	20	107.78

3.2.2 SMA Data

Arp 240 was observed with the SMA in ^{12}CO J=2-1 and ^{12}CO J=3-2 using the compact array configuration. The ^{12}CO J=3-2 has a beam size of $3.79'' \times 2.8''$. The data processing is described in Wilson et al. (2008). The moment 0 map is made from a cube with channel width of 40 km/s with a threshold of 2 RMS (127 mJy/beam).

3.2.3 Infrared Data

We obtained the Spitzer 3.6 um, 4.5 um and 24 um data from the archive. The Spitzer 3.6 um and 4.5 um data is from project 70038 (PI:Sanders) with a resolution of roughly 2 arcsec. We can use the data to calculate the stellar mass in the galaxies. The relevant equation is given in Eskew et al. (2012)

$$M_\star = 10^{5.65} F_{3.6}^{2.85} F_{4.5}^{-1.85} (\frac{D}{0.05})^2 \tag{3.2}$$

where $M_\star$ is the stellar mass in $M_\odot$. $F_{3.6}$ and $F_{4.5}$ are fluxes in Jy and D is the distance of the source in Mpc. This equation assumes a Salpeter IMF. To convert to the Kroupa IMF, we multiply the result by 0.7. The 24 um data is from the GOALS survey. The 24um data has a resolution of 6 arcsec (3 kpc). We use the calibrated relations from Leroy et al. (2008) to calculate the SFR.

$$\mathrm{SFR} = 2.14 \times 10^{-42} L(24um) \tag{3.3}$$

where SFR is the star formation rate in solar masses per year and $L(24um) = \nu_{24um} L_\nu(24um)$ is the luminosity of the source in erg s^{-1}.

We also use the Herschel 70 um data from the project KPGT_esturm_1

(PI: Sturm). The resolution is about 6 arcsec as well. We use the relationship from Kennicutt & Evans (2012) for calculating the SFR, which is

$$\mathrm{SFR} = 5.9 \times 10^{-44} \nu_{70um} L_{\nu} \tag{3.4}$$

where ν_{70um} is the rest frequency in Hz and L_{ν} is the luminosity of the source in ergs^{-1}Hz^{-1}.

3.2.4 Radio Continuum

Arp 240 was observed with the VLA in 33 GHz continuum. The detailed description of the data is in Linden et al. (2019). The resolution of the data is about 0.5 arcsec and the sensitivity is about 9.8×10^{-6} Jy/beam. The relation between the radio continuum and SFR has been calibrated (Murphy et al. 2011) as

$$\mathrm{SFR} = 10^{-27}[2.18(\frac{T_e}{10^4\ K})^{0.45}(\frac{\nu}{\mathrm{GHz}})^{-0.1} + 15.1 \times (\frac{\nu}{\mathrm{GHz}})^{-\alpha^{NT}}]^{-1}(\frac{L_{\nu}}{\mathrm{ergs^{-1}Hz^{-1}}}) \tag{3.5}$$

where SFR is in solar masses per year, T_e is the electron temperature in Kelvin, ν is the observed frequency in Hz and L_{ν} is the luminosity of the source in ergs^{-1}Hz^{-1}. α^{NT} is the spectral index for synchrotron emission. We assume $\alpha^{NT} = 0.7$ (Murphy et al. 2011) and $T_e = 10^4$K.

3.3 Measurements

3.3.1 Gas Mass

The ^{12}CO J=1-0 line is a commonly used tracer for molecular gas mass in galaxies. The equation to calculate the gas mass from the CO luminosity is

$$M_{mol} = \alpha_{CO} \times L_{CO}(1-0) \tag{3.6}$$

where M_{mol} is the molecular gas mass in $M_\odot$, $L_{CO}(1-0)$ is the ^{12}CO J=1-0 luminosity in K km s^{-1} pc^2 and $\alpha_{\rm CO}$ is the CO-to-H$_2$ conversion factor in $M_\odot$ (K km s^{-1} pc^2)$^{-1}$. L_{CO} is calculated as

$$L_{CO}(1-0) = 2453\ S_{CO}\Delta v D_L^2/(1+z) \tag{3.7}$$

where $S_{CO}\Delta v$ is the integrated flux in Jy kms^{-1}, D_L is the luminosity distance to the source in Mpc and z is the redshift of the source. The conversion factor $\alpha_{\rm CO}$ varies among different types of galaxies. We adopted the conversion factors of the Milky Way and ULIRGs separately to get the range of molecular gas mass. The gas mass is about $0.26 - 1.28 \times 10^{10}$ $M_\odot$ for NGC 5257 and $0.48 - 2.5 \times 10^{10}$ $M_\odot$ for NGC 5258.

In order to roughly quantify the conversion factor of the molecular gas, we adopt the recipe in Violino et al. (2018). In their paper, they calculate the conversion factor as

$$\alpha_{CO} = (1 - f_{SB}) \times \alpha_{CO,MS} + f_{SB} \times \alpha_{CO,SB} \tag{3.8}$$

where f_{SB} is the probability for a galaxy to be a starburst galaxy. This prob-

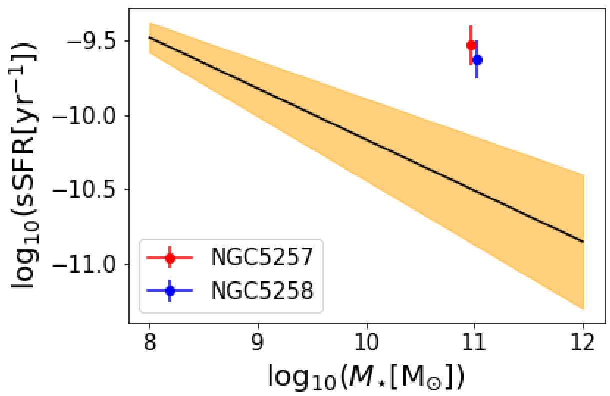

Figure 3.3: sSFR versus $M_\star$ for NGC 5257, NGC 5258. The straight line and the shade indicate the fitting line and 1 σ uncertainty of galaxies from star forming main sequence from Catinella et al. (2018)

ability is determined by the offset of the specific star formation rate (sSFR) from the star-forming main sequence (Sargent et al. 2014). For the expected sSFR of the main sequence versus a function of stellar mass, we adopted the equation from Catinella et al. (2018),

$$\log \mathrm{sSFR}_{MS} = -0.344(logM_\star - 9) - 9.822 \tag{3.9}$$

with an uncertainty of

$$\sigma_{MS} = 0.088(logM_\star - 9) + 0.188 \tag{3.10}$$

Then we calculate the ratio between the actual sSFR and the expected sSFR from the main sequence fitting relation. The ratio is 9.37 for NGC 5257 and 7.8 for NGC 5258 (see Fig 3.3). This corresponds to $f_{SB} \approx 1$. This analysis suggests that we should adopt the ULIRG conversion factor for both galaxies.

By comparing the moment 0 maps from all three lines, we can see the morphologies of the different line tracers are almost the same. Therefore, we use the ^{12}CO J=1-0 image to study the molecular gas distribution among different regions of the galaxies. For NGC 5257, the gas is clearly concentrated in the center. To quantitatively learn about the gas concentration degree, we calculated $\Sigma_{mol,500pc}/\Sigma_{mol,R25}$, which is the ratio between the gas surface density in the central 500 pc and within isophotal radius R25, which is 53.3 arcsec for NGC 5257 (Fuentes-Carrera et al. 2019). Since we assume the gas conversion factor is the same among different regions of the galaxy, we calculate the intensity ratio of ^{12}CO J=2-1 instead of the surface density ratio between the center and the whole region. Due to the limited sensitivity, we do not detect molecular gas out to the isophotal radius. We estimated the gas surface density out to R25 using two methods. The first method is to assume all the non-detected regions have an intensity equal to zero. The second is to assume all the non-detected regions have an intensity equal to the noise, which defines the lower limit of the ratio. We calculated the concentration degree of NGC 5257 to be 72 $\sim$ 95. Sakamoto et al. (1999) compared the gas concentration degree of barred galaxies and unbarred galaxies. They found the concentration degree is 100.2 ± 69.8 (the error is the standard deviation for 10 objects) for barred galaxies and 24.9 ± 18.5 for unbarred galaxies. This clearly suggests that NGC 5257 is fairly gas concentrated in the center. For NGC 5258, the gas is concentrated in the south spiral arm instead of the center. We therefore encircled the 500 pc aperture around the position of peak intensity in the south arm of NGC 5258. We calculated the concentration degree is around 33 $\sim$ 37. We can see the gas is less concentrated in the south arm of NGC 5258 than in the central region of NGC 5257. We also put the 500 pc aperture in the center of NGC 5258 and calculated the concentration degree in the center, which is about 11 $\sim$ 13. This value is among the typical values for normal disk galaxies.

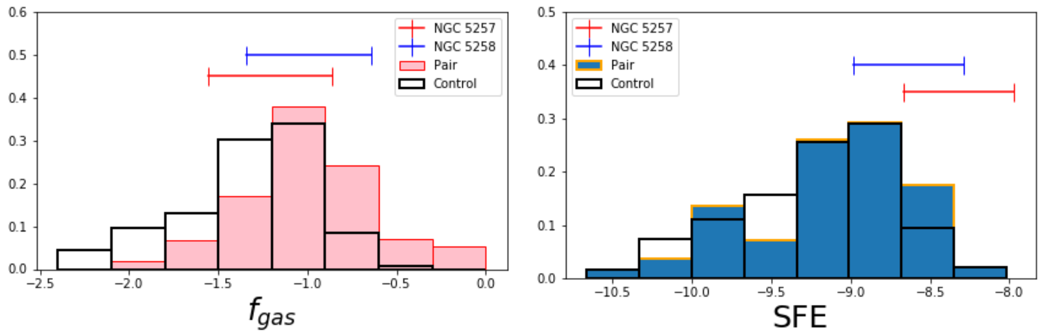

(a) (b)

Figure 3.4: (a) The gas fraction histogram of individual galaxies in the pairs and control samples from Pan et al. (2018). The global gas fractions of NGC 5257 and NGC 5258 are overlaid on the histogram. The upper and lower limit use the Miky Way and ULIRG conversion factor respectively. (b) The SFEs of NGC 5257 and NGC 5258 overplotted on the SFE histogram of individual galaxies in the pairs and control sample from Pan et al. (2018). The global SFEs of NGC 5257 and NGC 5258 are overplotted on the top. The lower and upper end correspond to the Milky Way and ULIRG α_{CO} respectively.

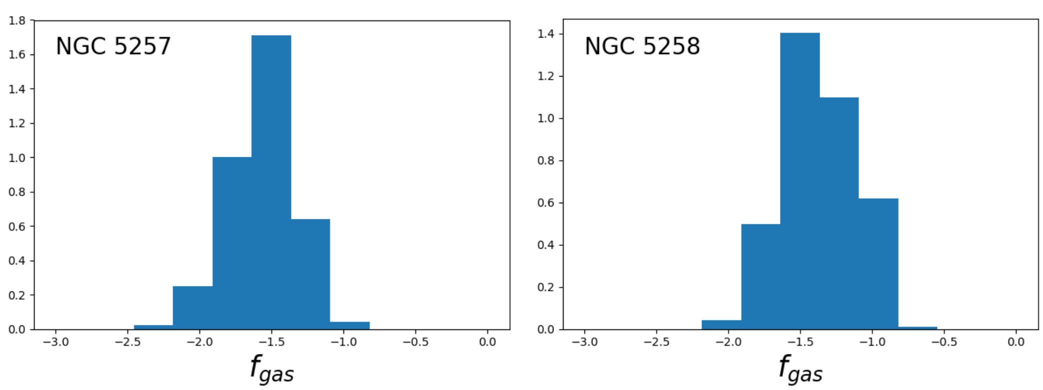

(a) (b)

Figure 3.5: The gas fraction histogram for individual pixels in (a) NGC 5257 and (b) NGC 5258. The conversion factor used is the ULIRG value.

We also calculated the global molecular gas to stellar mass fraction and SFE in both galaxies. The stellar mass is calculated with Spitzer 3.6 um and 4.5 um image (see section 2.3). We use both the Milky Way and ULIRG conversion factors, which set the upper and lower limit of the total gas mass. From Figure 3.4, we can see that the gas amount is low even compared to the normal disk galaxies if we adopt the ULIRG conversion factor. On the contrary, the SFE of both galaxies is at the higher end of the distribution even though we adopt the Milky Way α_{CO}. As we have described in the last paragraph, this system probably has the ULIRG α_{CO}. Therefore, the SFE in this galaxy should be significantly higher than normal spiral galaxies.

We also plotted the gas fraction histogram for the pixels of each galaxy. We apply the ^{12}CO J=1-0 intensity as the weighting of the histogram. For a given mass fraction bin, the weighted number count is calculated as

$$W_m = \sum_{m}^{i} I_{m,i} \tag{3.11}$$

where W_m is the weighted number counts of the m^{th} fraction bin, $I_{m,i}$ is the ^{12}CO J=1-0 intensity for i^{th} pixel in m^{th} bin. This way we calculated how much of the gas has a certain gas fraction instead of how many pixels. We then normalize the sum of the weighted number counts to be 1. This histogram is shown in figure 3.4. We only use pixels with ^{12}CO J=1-0 detections based on the ^{12}CO J=1-0 moment 0 maps made with the SpectralCube package (See section 2.1). From the histogram figure, we can see that NGC 5258 is more gas rich than NGC 5257. This might suggest NGC 5258 has more gas yet to be converted to stars and therefore is in a younger star forming stage.

Table 3.3: Line ratio measured in different regions of NGC 5257 and NGC 5258.

		^{12}CO/^{13}CO J=1-0	^{12}CO J=2-1/1-0
NGC 5257	Center	14.1 ± 1.3	0.87 ± 0.06
	Spiral Arm	13.9 ± 1.3	0.79 ± 0.06
	South West Bright Region	25.9 ± 4.9	0.80 ± 0.06
	South continuum	8.4 ± 3.4	1.3 ± 0.2
	total	13.1 ± 1.0	0.85 ± 0.06
NGC 5258	North Arm	13.3 ± 1.2	0.98 ± 0.09
	South Arm	13.7 ± 1.0	0.88 ± 0.07
	South SFR region	14.4 ± 1.1	0.91 ± 0.07
	Center	5.6 ± 0.5	0.80 ± 0.07
	Ring around Center	9.7 ± 0.8	0.77 ± 0.06
	Total	10.9 ± 0.8	0.85 ± 0.06

3.3.2 Line Ratio

We made brightness temperature ratio maps for the different molecular lines to see how the molecular gas properties vary among different regions. We made ^{12}CO/^{13}CO J=1-0 ratio maps and ^{12}CO J=2-1/1-0 ratio maps. Before we make the ratio map, we need to make sure all the data have the similar beam size and UV coverage. We cut the inner uvrange of the ^{12}CO J=1-0 and ^{13}CO J=1-0 data and uvtaper the ^{12}CO J=2-1 data in `tclean` in CASA. After getting the image cube, we smoothed all the image cubes to have a beam size of 2.186×1.896 arcsec. For making the ^{12}CO/^{13}CO J=1-0 ratio map, we notice that the ^{13}CO J=1-0 cube has fewer detected regions in the cubes. To make sure the ratio map only contains pixels with signal detected in both image cubes, we apply different threshold cuts while making moment 0 maps of the two cubes. We applied a 2 RMS cut for the ^{13}CO J=1-0 moment 0 maps. We then applied the same 2 times ^{12}CO J=1-0 RMS cut for the ^{12}CO J=1-0 moment 0 map and calculate the typical ^{12}CO/^{13}CO J=1-0 flux ratio across the whole galaxy. We then applied the 2 $\times$ ratio $\times$ ^{13}CO J=1-0 RMS

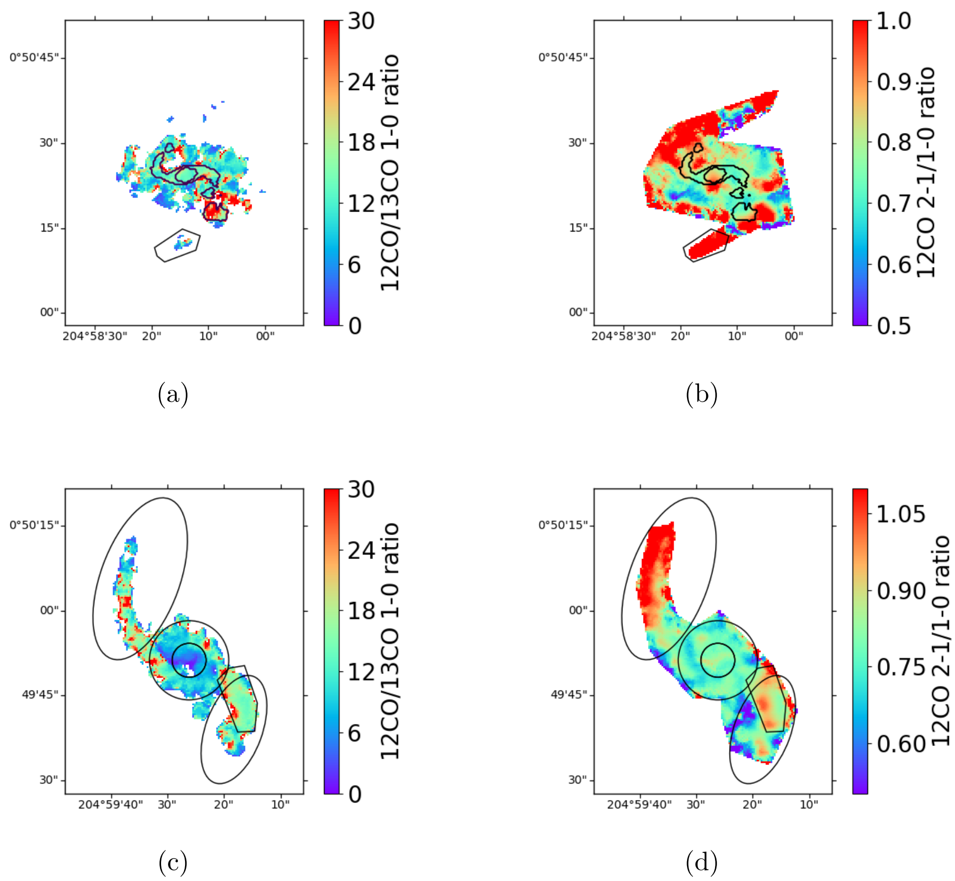

Figure 3.6: Temperature ratio maps of different molecular lines for NGC 5257 (top panel) and NGC 5258 (bottom panel). The left column is the ^{12}CO/^{13}CO J=1-0 ratio map and the right column is the ^{12}CO J=2-1/1-0 ratio map. The black regions are the apertures we used to measure the flux ratio (see text in detail).

cut to ^{12}CO J=1-0 cube to make the moment 0 map. The final step is to do primary beam correction for both moment 0 maps and calculate the ratio map. For the ^{12}CO J=2-1/1-0 ratio map, we applied the same procedure to calculate the ratio maps. Since the 2 RMS cut for ^{12}CO J=1-0 cube is a low threshold, the ratio map will contain a lot of false detected pixels with extreme values. Therefore, we manually draw polygons around each galaxy in ^{12}CO J=1-0 map and mask out the pixels outside this region.

Both ratio maps are shown in Figure 3.6. We divide both galaxies into different regions based on morphology. For NGC 5257, we divide the galaxy into center, disk, south west source based on the ^{12}CO J=1-0 intensity criterion. We also draw a polygon aperture on the separated south gas clump. For NGC 5258, we divided the galaxy into center, ring around center, north and south spiral arms. We further measured the ratio in the star forming region in the south spiral arm, as traced by the 33 GHz continuum image.

Both galaxies have a total ^{12}CO/^{13}CO J=1-0 flux ratio around 10, which is typical for normal spiral galaxies. For NGC 5257, the majority of the disk has a ^{12}CO/^{13}CO J=1-0 ratio around 13 except for the south-west belt region and the south isolated gas clump. The south west belt has a significantly higher ^{12}CO/^{13}CO J=1-0 ratio. This could be caused by a high [^{12}CO/^{13}CO] abundance ratio, which may suggest the inflow of fresh molecular gas from outer region or HI gas converting to the molecular gas. The south isolated gas clump has a low ^{12}CO/^{13}CO J=1-0 ratio but with a large uncertainty. As we can see from the ^{13}CO J=1-0 map, there is not much detected in this region. For NGC 5258, different regions have very different ratio values. The spiral arms have significantly higher ^{12}CO/^{13}CO J=1-0 ratios than the central region, which may also suggest a higher [^{12}CO/^{13}CO] abundance ratio in this region. The ^{12}CO/^{13}CO J=1-0 ratio map is used in later sections to calculate the conversion factor based on the assumption of LTE.

The global ^{12}CO J=2-1/1-0 ratio for both galaxies is about 0.85, which is larger than the typical ratio of 0.7 for normal spiral galaxies (references in Sun et al. 2018). The ratio varies less across different regions for both galaxies. For NGC 5257, the south region has a ratio value above 1.0, which may suggest this region is not in local thermal equilibrium (LTE). The same thing happens for the north spiral arm of NGC 5258. In later sections, we will use the ^{12}CO J=2-1 map to trace the gas surface density assuming a typical ^{12}CO J=2-1/1-0 ratio. We generally assume the typical ratio to be the global flux ratio between ^{12}CO J=2-1 and ^{12}CO J=1-0 map.

3.3.3 Star Formation Rates

Murphy et al. (2011) started to use 33 GHz continuum as a SFR tracer. The radio continuum mainly comes from two sources, free-free and synchrotron. Therefore, an important parameter is what is the fraction of each component. We use the Spitzer 24um and Herschel 70 um data to test if the radio continuum SFR equation holds in these regions. From Galametz et al. (2013), we can also calculate the total infrared luminosity of the galaxy based on the 24 um and 70 um flux, which is

$$L_{TIR} = 3.98\nu_{24um}L_{24um} + 1.553\nu_{70um}L_{70um} \tag{3.12}$$

where L_{TIR} is the total infrared luminosity in erg s^{-1}, ν_{24um} and ν_{70um} are the frequency of each wavelength in Hz, L_{24um} and L_{70um} are the luminosity of the galaxy in the corresponding wavelength in erg s^{-1} Hz^{-1}. Then we can calculate the SFR based on the derived L_{TIR} (Kennicutt & Evans 2012), which is

$$\mathrm{SFR} = 3.9 \times 10^{-44} L_{TIR} \tag{3.13}$$

where SFR is the star formation rate in $\mathrm{M}_\odot$/yr.

Since Spitzer and Herschel have beam sizes of 6 arcsec, the measured flux could be affected by aperture effects. We first smooth the 33 GHz image to have the same beam size of 6 arcsec. We then compare the flux measured in the south and center region in the original image and smoothed image of 33 GHz to find the aperture size to measure the flux of the region. We get the aperture size to be about 1.24 times the beam size of 6 arcsec.

The results are shown in Table 2. We can see for the center region, the 33 GHz result is consistent with the 70 um SFR calculation result, but differs from the Spitzer result. By comparing the Spitzer and Herschel images of NGC 5257, we can see the flux in the center differs quite a lot. Since NGC 5257 is an early merger, there is still not much AGN activity (Díaz-Santos et al. 2017). The far-infrared radiation could trace the SFR quite well. The combined SFR also favors the 70 um result, which confirms the 33 GHz as a SFR tracer in the center.

In the south region, the 33 GHz differs from the 24 um and 70 um result a bit more. This region has been identified as a single young ($\sim$ 4 Myr), massive ($\sim 10^7$ $\mathrm{M}_\odot$) star cluster (Linden et al. 2017). In this region, there could be an instantaneous starburst instead of continuous SF activity at a certain rate. Therefore, the SFR equation might fail in this case.

For NGC 5258, we did the same process for the south arm region to calculate the aperture size we should adopted. We adopted a circular aperture with

Table 3.4: SFR in different regions of NGC 5257 and NGC 5258.

		SFR ($M_\odot$/yr)			
		24um	70um	24um and 70um	33 GHz
NGC 5257	center	1.16	1.97	2.0 ± 0.2	2.17 ± 0.05
	south	2.15	1.94	1.99 ± 0.2	2.8 ± 0.06
NGC 5258	south arm	6.04	7.29	7.48 ± 0.8	8.9 ± 0.3

radius of 6 arcsec. The calculated SFR is also shown in the Table 2. Generally the SFRs from 24um and 70um agree well with 33 GHz but is systematically lower.

From the comparison above, we can see that the SFR calculated using 33 GHz is generally consistent with the results from other SFR tracers. It indicates that those radio luminous regions are indeed SF regions. Furthermore, the 33 GHz continuum have a better resolution, which enables us to obtain a more accurate measurement of Σ_{SFR} in the starburst regions. As shown in Fig. 3.7, we draw polygon apertures around different SF regions to measure the Σ_{SFR}, which is shown in Table 3.10. These polygon regions drawn by eye roughly correspond to regions with S/N value greater than 4.0. We also tried to vary the boundary slightly and the measured Σ_{SFR} doesn't significantly change. However, due to the limited sensitivity of the 33 GHz continuum, we actually miss a large fraction of SFR outside those polygon apertures. The SFR enclosed in the center of NGC5257 takes up only 7% of the total SFR of NGC 5257, which is similar to the south continuum source in NGC 5257. For NGC 5258, the only radio detected SF region contains about 30% of the total SFR of this galaxy. Therefore, we need to note that those starburst regions might not be representative of the SF activities in the entire system.

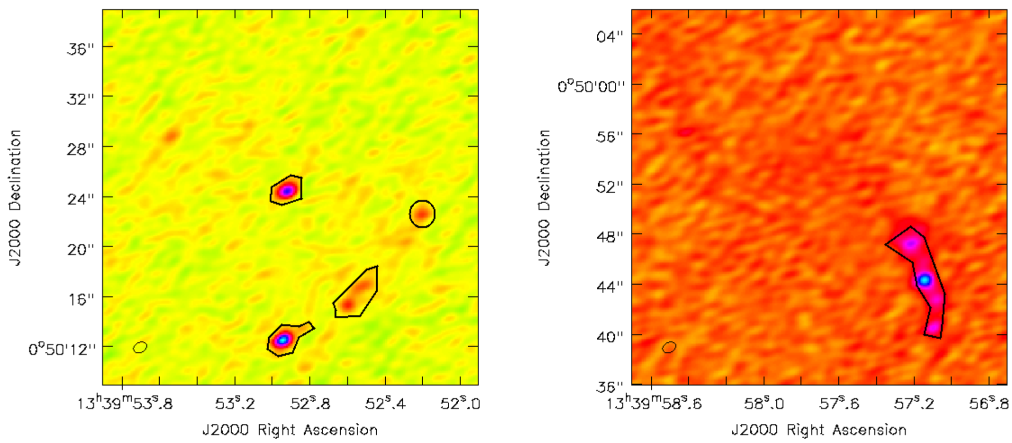

Figure 3.7: 33 GHz continuum image for NGC 5257 (Left) and NGC 5258 (Right) smoothed to the beam size of 1.1″× 0.8″. We divide both galaxies into different regions based on the 33 GHz intensity. NGC 5257 is divided into center, south continuum source, south-west arm and west point region. NGC 5258 only has a strong detection in the south spiral arm.

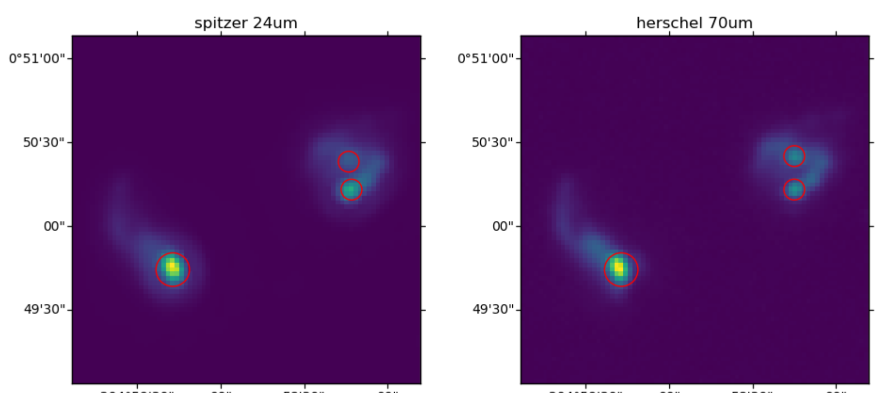

Figure 3.8: Spitzer 24 µm and Herschel 70 µm image of Arp 240. Red Circles are apertures used to measure the flux and calculate the SFR from the image.

Table 3.5: Properties of the star cluster in the south region of NGC 5257

$M_\star$ ($M_\odot$) (B band)	$M_\star$ ($M_\odot$) (33 GHz)	gas mass ($M_\odot$) (within 500 pc)	virial mass ($M_\odot$) (within 500 pc)
4×10^6	1.8×10^7	9.25×10^7	4.7×10^8

3.3.4 The Southern Star Cluster in NGC 5257

In NGC 5257, the south continuum source stands out for low gas content but high SFR. Linden et al. (2019) pointed out that this region corresponds to a single star cluster identified in Linden et al. (2017), as shown in Figure 3.9. We can see there is a slight offset (1.0 arcsec) between the identified star cluster position and the peak of the south continuum source. This might be due to a systematic offset in the optical observation. This young star cluster is massive ($\sim 4 \times 10^6$ $M_\odot$) and young ($\sim$ 3.3 Myr) (Linden et al. 2017). We can also use the 33 GHz flux to derive the mass of the south continuum source. For a young star cluster, we expect all the photons to come from the free-free emission. Therefore, using the equation from Murphy et al. (2011), we can calculate the total number of photons based on the equation

$$\left[\frac{Q(H^0)}{\mathrm{s}^{-1}}\right] = 6.3 \times 10^{25} \left(\frac{T_e}{10^4\mathrm{K}}\right)^{-0.45} \left(\frac{\nu}{\mathrm{GHz}}\right)^{0.1} \times \left(\frac{L_\nu}{\mathrm{ergs}^{-1}\mathrm{Hz}^{-1}}\right) \tag{3.14}$$

where $Q(H^0)$ is the total number of ionizing photons, T_e is the electron temperature which is generally assumed to be 10^4 K and L_ν is the luminosity of the source at 33 GHz. We can then calculate the star cluster mass based on the equation in Leroy et al. (2018)

$$M_\star \sim \frac{Q(H^0)}{4 \times 10^{46}} \mathrm{M}_\odot \tag{3.15}$$

where $M_\star$ is the mass of the star cluster. The stellar mass of the south continuum source is about 1.8×10^7 $M_\odot$. This is clearly larger than the mass derived from B band. If we consider the contribution from synchrotron radiation as we did for calculating the SFR, we will get the stellar mass to be about 1.0×10^7 $M_\odot$.

As we can see in Figure 3.9, there is CO emission around this region. To see if the gas in this region is gravitationally bound, we can compare the gas mass and virial mass in this region. We choose the peak of the 33 GHz continuum in this region and draw the aperture with radius of 1.1 arcsec (528 pc) to measure the ^{12}CO J=2-1 flux in this region. We then use the measured ^{12}CO J=2-1/1-0 ratio to calculate the equivalent ^{12}CO J=1-0 flux in this aperture. We adopt the typical ULIRG conversion factor with helium included to calculate the gas mass. The calculated molecular gas mass is 9.25×10^7 $M_\odot$. The virial mass is calculated as (Leroy et al. 2018)

$$M_{vir} = 892 * R * \sigma_v^2 \tag{3.16}$$

where R is the radius of aperture in pc and σ_v is the velocity dispersion of this region in km/s. The measured velocity dispersion is about 31 km/s. The virial mass within the aperture is $4.7 \times 10^8 M_\odot$. We can see the viral mass is about a factor of 5 larger than the measured gas mass assuming ULIRG conversion factor. This suggests the gas surrounding the star clusters is not gravitationally bound. However, due to the limitation of the resolution, we might encircle a lot of clouds that are not gravitationally bound to the star cluster. We also compared the gas mass and virial mass within the whole south gas clump in the ^{12}CO J=2-1 map. We approximate this region as an

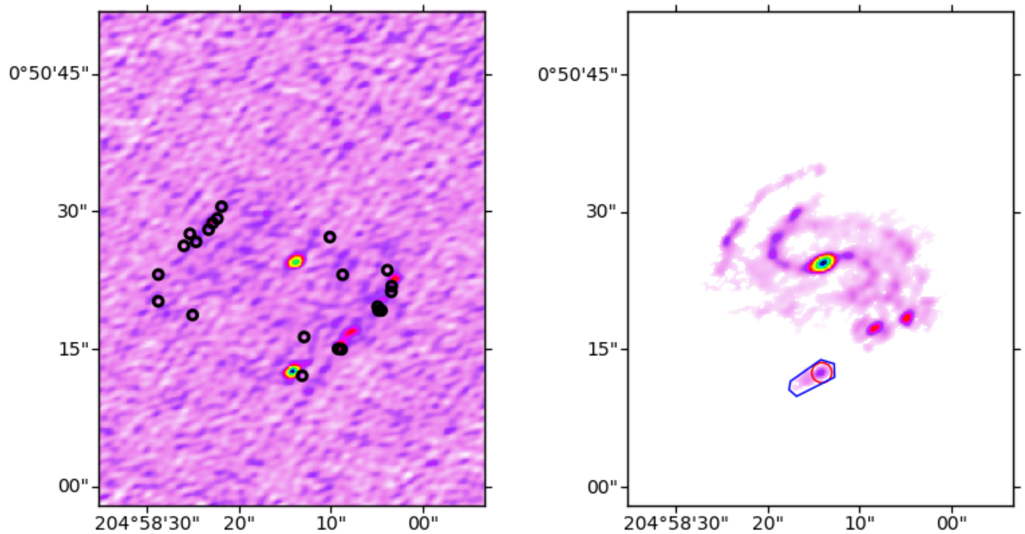

(a) (b)

Figure 3.9: (a) Star clusters identified in Linden et al. (2017) in NGC 5257. The black circles are identified star clusters. The background image is 33 GHz continuum. (b) The aperture used to measure the gas mass around the star cluster in the south continuum source.

elongated ellipse with size of $4'' \times 1.5''$. We calculate the characteristic radius as

$$R = \sqrt{\text{major} \times \text{minor}} \tag{3.17}$$

where the major and minor axis are in units of pc. We get the virial gas to gas mass ratio of 1.9 for the whole region, which is not so far from 1.0. We need to note that the rough estimate of the size and irregular shape of cloud will bring a lot of uncertainty. Overall, the clumps around the south continuum source seem more likely to be gravitationally bound.

3.3.5 Dust Temperature

The dust temperature is correlated with the gas temperature in extremely dense regions where the dust and gas are expected to be well coupled in thermal equilibrium. The 24 um and 70 um images trace the radiation from dust. Therefore, we can derive the dust temperature based on the ratio of the fluxes in different regions. We assume a modified gray body spectrum for the dust in optically thin limit. In this case, the spectrum of the dust can be expressed as (Casey 2012)

$$S_\nu \propto \nu^\beta B_\nu(T) = \frac{\nu^{\beta+3}}{e^{h\nu/kT} - 1} \tag{3.18}$$

where S_ν is the intensity of the dust source, $B_\nu(T)$ is the blackbody radiation and β is the spectral emissivity index. β is generally assumed to be 1.5 with a large range between 1 and 2. We can get the flux with same proportional relationship. Dividing the 70 um flux by the 24 um flux, we have the relation

$$\frac{F_{70um}}{F_{24um}} = \left(\frac{\nu_{70um}}{\nu_{24um}}\right)^{3+\beta} \frac{e^{h\nu_{24um}/kT} - 1}{e^{h\nu_{70um}/kT} - 1} \tag{3.19}$$

where F_{70um} and F_{24um} are the fluxes measured from 24 um and 70 um image, ν_{24um} and ν_{70um} are the frequencies of corresponding wavelength. The results are in Table 3.6. For NGC 5257, we can see both the center and the south region has dust temperatures around 50 to 60 K. Vlahakis et al. (2005) show for local disk galaxies that the dust emission can be generally decomposed into cold and warm component. Therefore, our measured dust temperature should be mostly from the warm component (30 – 50 K). The cold dust component makes up the majority of the dust mass and is more associated with the cold molecular gas. Therefore, we would expect the measured dust temperature

Table 3.6: Dust Temperature

Galaxy	Region	Dust Temperature (K)		
		$\beta = 1$	$\beta = 1.5$	$\beta = 2.0$
NGC 5257	Center	56	52	48
	South	61	57	53
NGC 5258	South Arm	59	54	51

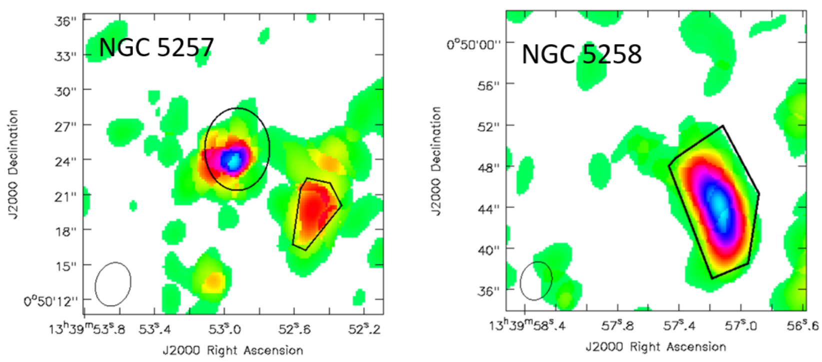

(a) (b)

Figure 3.10: The SMA moment 0 map of ^{12}CO J=3-2 for (a) NGC 5257 and (b) NGC 5258. Regions encircled by black apertures are used for radex modeling.

sets the upper limit of the gas temperature.

3.4 Radiative Transfer Analysis

To constrain the physical properties of the molecular gas, we use the radiative transfer code RADEX (van der Tak et al. 2007). This code calculates line intensity based on input temperature, number density of H_2 and column density of the modeled molecules divided by the linewidth. We use a grid of models across the parameter space to fit the observed line intensities. In addition to gridding, we use a Baysian likelihood code by (Kamenetzky et al. 2016) to create probability distributions for the various parameters. This code gives two

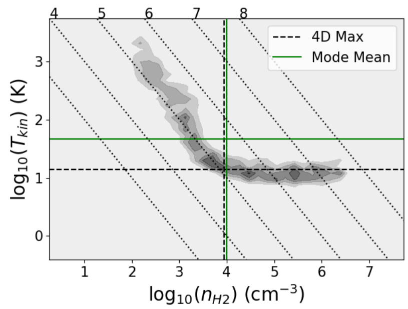

(a)

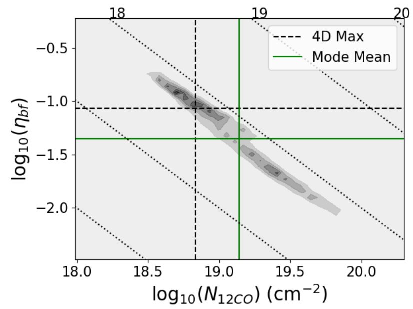

(b)

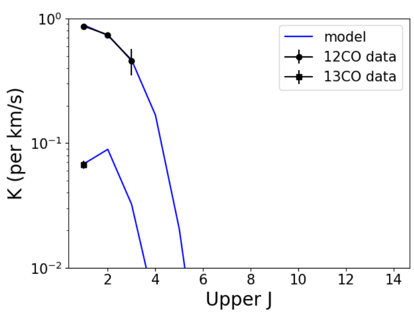

(c)

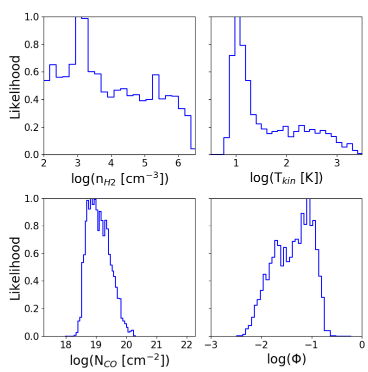

(d)

Figure 3.11: RADEX modeling results for the center of NGC 5257 assuming [^{12}CO/^{13}CO]=50. (a) The temperature vs volume density probability distribution contour. Diagonal dot-dashed lines indicate constant thermal pressure. The green and dashed cross indicates the 1D mean value and 4D best fit value respectively. (b) The column density vs beam filling factor probability distribution contour. Diagonal dot-dashed lines indicate constant beam averaged column density. (c) The spectral line energy distribution (SLED) of the data and modeled result. (d) The 1D probability distribution function of temperature, volume density, column density and beam filling factor.

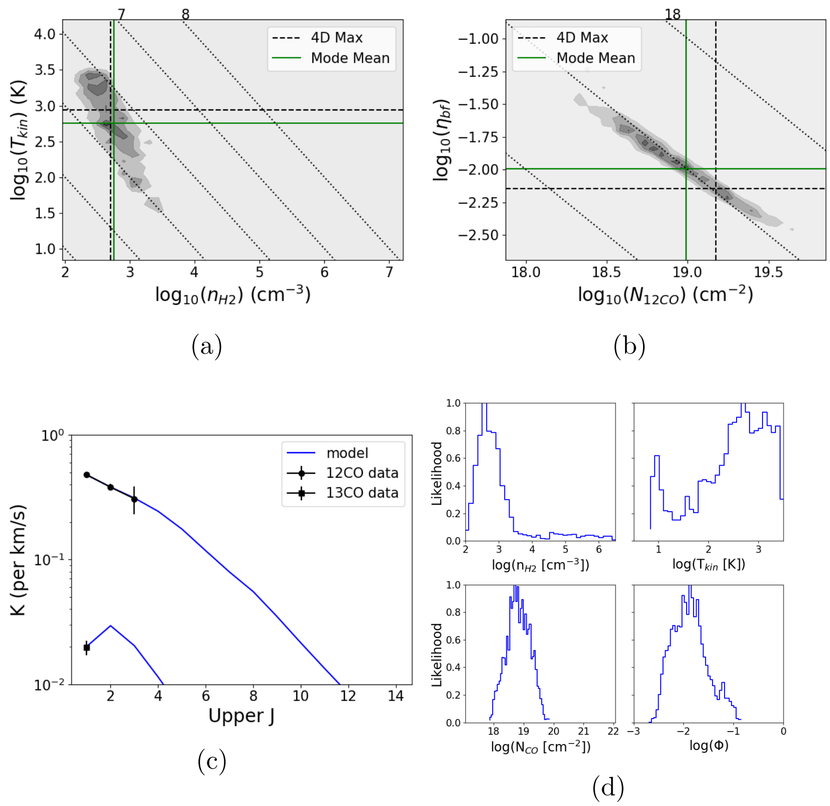

Figure 3.12: RADEX modeling results for the southwest ^{12}CO J=3-2 concentration region of NGC 5257 assuming [^{12}CO/^{13}CO]=50. See Figure 3.11 for details.

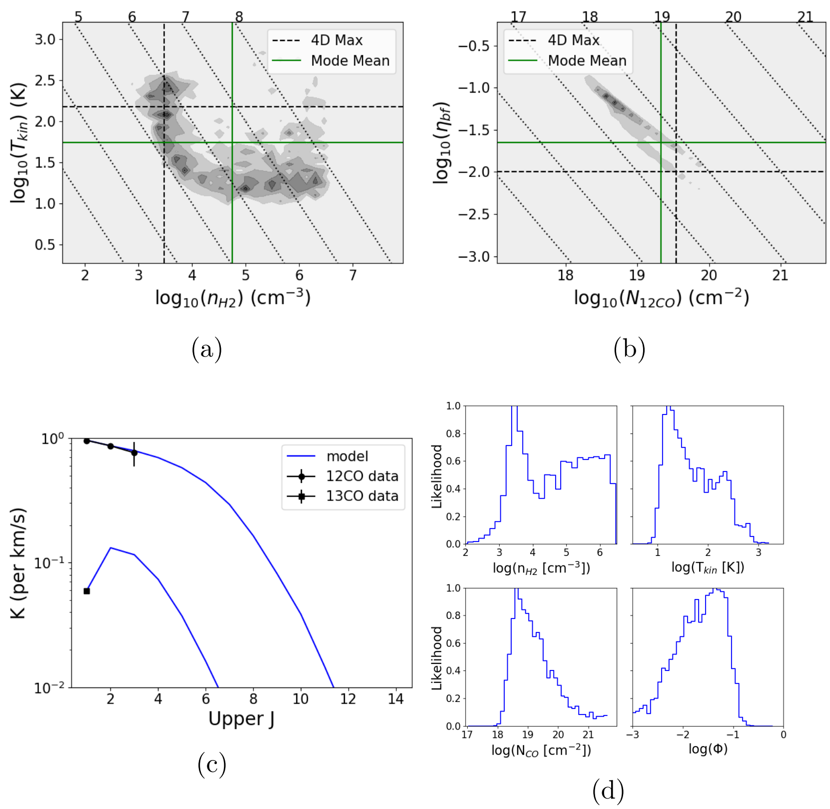

Figure 3.13: RADEX modeling results of the south arm of NGC 5258 assuming [^{12}CO/^{13}CO]=50. See Figure 3.11 for details.

types of solutions, 1D Max and 4D max. The 1D max gives the solution of the parameters with maximal likelihood in one dimensional parameter space. The 4D max gives the solution with maximal likelihood for the combination of the 4 parameters. This code also introduces an additional parameter called the beam filling factor, which is how large a fraction of the area CO emission actually covers within a single beam. This factor is somewhat degenerate with the actual CO column density, but these two parameters have different effects on the CO line ratios. This code also includes a two-component model to account for the radiation from the warm gas. For more details on the likelihood code, see Kamenetzky et al. (2016) .

We use all 3 CO lines observed with ALMA. We smooth all the line images to a common beam of $2.186'' \times 1.896''$ and measure the average intensity of different regions. For the center of NGC 5257 and the south arm of NGC 5258, we also use the ^{12}CO J=3-2 detection from the SMA. Therefore we smooth all the line images to a beam size of $3.8'' \times 2.99''$ and measure the average intensity. Possibly due to the missing flux problem of the SMA data (Wilson et al. 2008), the center of NGC 5257 has an extremely low ^{12}CO J=3-2 flux compared to the fluxes of the other lines. Therefore, we use the peak intensity instead of the average intensity for the center of NGC 5257. To constrain all the parameters, we would still need an additional ^{13}CO line. Therefore, we fix the [^{12}CO/^{13}CO] abundance ratio to be 30, 50 and 100, respectively, based on Cormier et al. (2018) to run the code. Because we only model the lower J CO lines, we chose a one-component model. The linewidth is measured as the median full width at half maximum (FWHM) of the lines in the selected region. The RADEX inputs is given in Table 3.7

Table 3.7: Input parameters for the RADEX modeling.

Galaxy	Region	Assumed $[^{12}CO/H_2]$	linewidth (km/s)	Beam (arcsec)	Helium Correction
NGC 5257	center	10^{-4}	135	3.789×2.989	1.4
NGC 5257	southwest	10^{-4}	116.1	3.789×2.989	1.4
NGC 5258	south arm	10^{-4}	87.0	3.789×2.989	1.4

3.4.1 Results

The results are shown in Table 3.8. Most results vary with the different assumed $[^{12}CO/^{13}CO]$ ratios. The density varies by 2 orders of magnitude among different $[^{12}CO/^{13}CO]$ ratios and cannot be constrained very well. Temperature, column density and beam filling factor vary less.

We can see for both the center of NGC 5257 and the south arm of NGC 5258, where the gas is mostly concentrated, the temperature and the density are similar. However, for the off-center ^{12}CO J=3-2 luminous region in NGC 5257, the temperature is much higher and the density is much less. This is what we expect as this region doesn't show an emission peak in the ^{12}CO J=1-0 and ^{12}CO J=2-1 moment 0 maps. However, the temperature and density in each region is much less constrained. In fact, the 1D PDF of the solution for these quantities always shows a double peak and the best fitted value always varies among the different assumed $[^{12}CO/^{13}CO]$.

Another interesting quantity is the beam filling factor η_{bf}. η_{bf} is around $0.01 \sim 0.1$. For nearby normal spiral galaxies, this quantity is on the order of several 0.1 (Krumholz et al. 2012). Our derived value is a bit lower than this value. However, we need to keep in mind that we smooth all the images to the beam of $3.8'' \times 2.9''$. Therefore, the emission actually covers regions with no signal detection and η_{bf} is reduced by this artificial effect. Taking the center of NGC 5257 as an example, we can see from the ^{12}CO J=2-1 moment 0 map in Fig. 3.1 that the emission from the center is roughly the same as the beam size of $1.1'' \times 0.6''$. When it's smoothed to $3.8'' \times 2.9\,''$, the beam filling factor is brought down by a factor of 16.

Table 3.8: RADEX Modeling Results

Galaxy	Region	Assumed $[^{12}CO/^{13}CO]$	T_{kin} (K)	$\log(n_{H2})$ (cm^{-3})	$\log(N_{12CO})$ (cm^{-2})	η_{bf}	log(P) (K cm^{-3})	$\log(N_{12CO,bc})$ (cm^{-2})
NGC 5257	Center	100	$64\,^{+175}_{-46}$	3.3 ± 1.3	19.53 ± 0.32	$0.04^{+0.04}_{-0.02}$	5.9 ± 0.9	18.12 ± 0.10
NGC 5257	Center	50	$46\,^{+180}_{-36}$	4.0 ± 1.2	19.14 ± 0.38	$0.04\,^{+0.06}_{-0.03}$	5.6 ± 0.8	17.79 ± 0.09
NGC 5257	Center	30	$51\,^{+248}_{-42}$	4.0 ± 1.2	18.85 ± 0.42	$0.05\,^{+0.08}_{-0.03}$	5.7 ± 0.7	17.55 ± 0.07
NGC 5257	South West	100	$122\,^{+609}_{-102}$	3.5 ± 1.3	19.14 ± 0.42	$0.02\,^{+0.02}_{-0.009}$	5.6 ± 0.8	17.33 ± 0.14
NGC 5257	South West	50	$564\,^{+1157}_{-379}$	2.8 ± 0.3	18.99 ± 0.28	$0.01\,^{+0.007}_{-0.004}$	5.5 ± 0.3	17.00 ± 0.06
NGC 5257	South West	30	$562\,^{+1554}_{-413}$	2.6 ± 0.5	18.09 ± 0.48	$0.04^{+0.07}_{-0.03}$	5.4 ± 0.3	16.74 ± 0.08
NGC 5258	South Arm	100	$69\,^{+141}_{-46}$	4.6 ± 1.2	19.77 ± 0.75	$0.02\,^{+0.03}_{-0.01}$	6.5 ± 1.1	18.02 ± 0.35
NGC 5258	South Arm	50	$55\,^{+114}_{-37}$	4.7 ± 1.1	19.33 ± 0.76	$0.02\,^{+0.04}_{-0.02}$	6.5 ± 1.0	17.67 ± 0.33
NGC 5258	South Arm	30	$123\,^{+497}_{-98}$	3.7 ± 1.1	18.79 ± 0.49	$0.03\,^{+0.04}_{-0.02}$	5.8 ± 0.6	17.23 ± 0.13

For each assumed [^{12}CO/^{13}CO] ratio value, the beam averaged column density, which is the multiplication of column density and beam filling factor, is more accurately modeled than the two individual parameters. Therefore, we will use the beam averaged column density to calculate the conversion factor in different regions.

3.4.2 CO-to-H_2 Conversion Factor

From the RADEX modeling, we get the 1D mean result for the ^{12}CO beam averaged column density. We can calculate the H_2 surface density based on the ^{12}CO column density of the gas and an assumed [^{12}CO/H_2] abundance ratio with

$$N_{H_2} = \frac{N_{12CO}}{[^{12}\mathrm{CO/H_2}]} \tag{3.20}$$

where N_{H_2} is the column density of H_2, N_{12CO} is the column density of the ^{12}CO and [^{12}CO/H_2] is the CO to H_2 abundance ratio. In this case we assume [^{12}CO/H_2] $= 1 \times 10^{-4}$. We can compare these results directly with the ^{12}CO J=1-0 intensity to calculate the conversion factor.

We calculate α_{CO} for these three regions separately. From the calculation, we can see the conversion factor of the three regions are closer to the typical ULIRG conversion factor. The derived conversion factor is highly dependent on the assumed [^{12}CO/^{13}CO] and [^{12}CO/H_2] abundance ratios. To constrain the [^{12}CO/^{13}CO] ratio, we need at least two more CO lines.

3.4.3 Comparison with LTE Analysis

We can do a local thermal equilibrium (LTE) analysis for the ^{12}CO/^{13}CO J=1-0 ratio to try to understand what causes the change in ratio. When both ^{12}CO

Table 3.9: RADEX modeled α_{CO} results

Galaxy	Region	Conversion Factor ($M_\odot pc^{-2}(Kkms^{-1})^{-1}$)		
		[^{12}CO/^{13}CO]=100	[^{12}CO/^{13}CO]=50	[^{12}CO/^{13}CO]=30
NGC 5257	Center	1.88	0.88	0.52
	Arm	0.90	0.42	0.23
NGC 5258	South Arm	2.92	1.33	0.48

and ^{13}CO lines are optically thin, the ratio of the brightness temperatures will tell us about the abundance ratio. In the general case, ^{12}CO is optically thick while ^{13}CO is optically thin. In that case (Cormier et al. 2018),

$$R = \frac{T_{ex,12}(1 - e^{-\tau_{12CO}})}{T_{ex,13}(1 - e^{-\tau_{13CO}})} \tag{3.21}$$

where $(1 - e^{-\tau_{12CO}}) \to 1$ and $(1 - e^{-\tau_{13CO}}) \to \tau_{13CO}$. The ratio can then be simplified as

$$R = \frac{1}{\tau_{13CO}} \tag{3.22}$$

Then we can calculate the column density based on the excitation temperature and optical depth via

$$N_{13} = \frac{3.0 \times 10^{14}}{1 - \exp(-5.29/T_{ex,13})} \times \frac{\tau_{13CO}}{1 - \exp(-\tau_{13CO})} \times I_{13CO}[\mathrm{cm}^{-2}] \tag{3.23}$$

where N_{13} is the ^{13}CO column density in cm^{-2} and I_{13CO} is the ^{13}CO intensity in the units of Kkms^{-1}. We also have

$$T_{obs} = \eta_{bf} J_\nu(T_{ex,13}) \times (1 - e^{-\tau_{13CO}}) \tag{3.24}$$

where $J_\nu(T_{ex,13})$ is the blackbody intensity with temperature of $T_{ex,13}$, η_{bf} is the beam filling factor of ^{13}CO and T_{obs} is the observed brightness temperature of ^{13}CO J=1-0 which can be calculated as

$$T_{obs} = \frac{I_{13CO}}{\text{FWHM}} \tag{3.25}$$

where FWHM is the linewidth of the spectrum.

We use these equations to map the conversion factor across both galaxies. We assume the abundance ratio of [^{12}CO/^{13}CO] to be 50 and the beam filling factor to be 0.1. We also assume that [^{12}CO/H_2]=10^{-4}, which is the same as our input into the RADEX model. We then binned the pixels to be 1.5″× 1.5″. The map of the conversion factor is shown in Figure 3.14. For both galaxies, we can clearly see that the bulk of the region has a conversion factor below 1.0. This suggests that most of gas in Arp 240 has a typical ULIRG conversion factor.

In Fig. 3.14, we also show the conversion factor as function of ^{12}CO J=1-0 intensity. Basically we can see there is no correlation between $\alpha_{\rm CO}$ and ^{12}CO J=1-0 line intensity. This is inconsistent with Narayanan et al. (2012), who found a negative correlation between $\alpha_{\rm CO}$ and ^{12}CO J=1-0 intensity. However, we need to note that in this analysis, we assume a constant beam filling factor across the entire system, which is probably not true in the real situation.

3.5 Gas Properties and SFR

We use the 33 GHz continuum image to trace the SFR. We divide both galaxies into different regions based on the 33 GHz continuum image, as shown in Figure

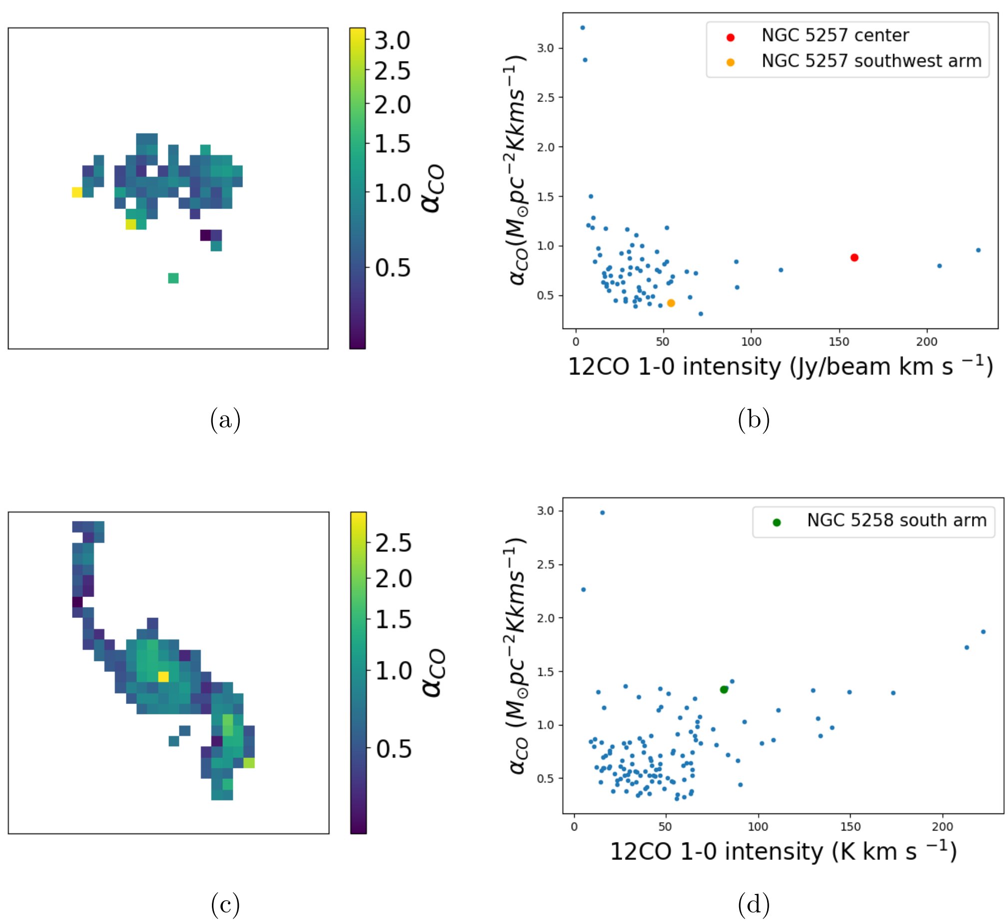

Figure 3.14: (Left) The map of the conversion factor for (a) NGC 5257 and (c) NGC 5258. (Right) $\alpha_{\rm CO}$ as a function of ^{12}CO J=1-0 intensity for each individual pixel in (b) NGC 5257 and (d) NGC 5258. The big filled points represent the RADEX derived $\alpha_{\rm CO}$.

Table 3.10: Depletion time of different regions in NGC 5257 and NGC 5258

Galaxy	Region	Σ_{SFR} ($\mathrm{M_\odot kpc^{-2} yr^{-1}}$)	Σ_{mol} ($\mathrm{M_\odot pc^{-2}}$)	Depletion Time (10^8 years)
NGC5257	center	0.58	163	2.8
	arm	0.38	51	1.36
	South	1.1	28.6	0.26
NGC5258	South Arm	0.79	133	1.69

Σ_{SFR} is calculated using the 33 GHz image
Σ_{mol} is calculated using ^{12}CO J=2-1 assuming ^{12}CO J=2-1/1-0 ratio of 0.85 and typical ULIRG conversion factor

3.7. We can then calculate the depletion time with

$$t_{dep} = M_{mol}/\mathrm{SFR} \tag{3.26}$$

The molecular mass is calculated based on the ^{12}CO J=2-1 intensity. We assume the conversion factor to be a ULIRG conversion factor. We also assume the ^{12}CO J=2-1/1-0 ratio is about 0.85, which is the flux ratio measurement from section 3.2. The depletion time is shown in Table 3.10. We can see different regions have very different depletion times. The different depletion times could be caused by different gas environments. We further explore this below.

3.5.1 Turbulence Model

One of the theoretical models to account for different depletion times is the turbulence model (Krumholz & McKee 2005). According to this model, turbulence will broaden the density PDF of the clouds. Assuming a constant SFE per free-fall time, the depletion time will decrease as the surface density of the gas increases. The general equation for free-fall time is

$$t_{ff} = \sqrt{\frac{3\pi}{32G\rho_{mid}}} \tag{3.27}$$

where ρ_{mid} is the volume density of the molecular gas in the middle of the disk. If we assume the galaxy is filled with gas, then the volume density could be calculated as

$$\rho_{mid} = \frac{\Sigma_{mol}}{2H} \tag{3.28}$$

where H is the scale height of the disk and Σ_{mol} is the surface density of the molecular gas measured from the ^{12}CO J=2-1 cube (See section 3.2). Assuming the gas disk is in equilibrium and that vertical gravity is dominated by gas self-gravity, then we can calculate the scale height as (Wilson et al. 2019)

$$H = \frac{\sigma_v^2}{\pi G \Sigma_{mol}} \tag{3.29}$$

where σ_v is the velocity dispersion of the molecular gas. Combining all the equations above, we can write the free-fall time as

$$t_{ff} = \frac{\sqrt{3}}{4G}\frac{\sigma_v}{\Sigma_{mol}} \tag{3.30}$$

Therefore the SFE per free-fall time can be calculated as

$$\epsilon_{ff} = \frac{t_{ff}}{t_{dep}} = \frac{\sqrt{3}}{4G}\frac{\sigma_v \Sigma_{SFR}}{\Sigma_{mol}^2} \tag{3.31}$$

(Wilson et al. 2019). Using these equations we can calculate ϵ_{ff}. We use the ^{12}CO J=2-1 cube processed with the script from Sun et al. (2018) to calculate the moment 0 and moment 2 map. Then we smooth both the ^{12}CO J=2-1 image and the 33 GHz image to a beam size of $1.1'' \times 0.8''$. We then binned the pixels to $1.0'' \times 1.0''$. Then we applied the S/N=4 cut for the 33 GHz image. The result is shown in Figure 3.15.

As shown in the figure, the SFR, t_{dep} and ϵ_{ff} extend smoothly from the results of U/LIRGs from Wilson et al. (2019) assuming the ULIRG conversion factor. However, in the low surface density regions, ϵ_{ff} can be above 1.0. For general clouds, ϵ_{ff} can be as high as several 10% (Lee et al. 2016). Therefore, we might overestimate the true efficiency in this case.

The freefall time calculated on a galactic scale will tend to overestimate the true freefall time for the collapse of an individual GMC. As we do not have accurate information about the velocity dispersion and surface density on GMC scales, we will assume some typical values for these variables just to see how this GMC analysis will affect the efficiency. In this case, the star-forming efficiency is regulated by collapse of individual clouds instead of a 500 pc region. We consider a toy model assuming all the clouds within the 500 pc pixel region are identical with beam filling factor $\eta_{bf} = 0.1$. The free-fall time can be derived in the following steps. As we know, the most general equation for free-fall time is

$$t_{ff} = \sqrt{\frac{3\pi}{32G\rho_{GMC}}} \tag{3.32}$$

We assume the relationship between ρ_{GMC} and Σ_{GMC} is

$$\rho_{GMC} = \frac{\Sigma_{GMC}}{2R} \tag{3.33}$$

where R is the radius of the cloud. Due to the beam filling factor, the observed molecular density relates to the real GMC density as

$$\Sigma_{GMC} = \Sigma_{mol}/\eta_{bf} \tag{3.34}$$

We also have the size-linewidth relation (Heyer et al. 2009), which is

$$\sigma_{GMC} = CR^{0.5} \tag{3.35}$$

Combining all those equations above, we have:

$$t_{ff} = \frac{\sqrt{3}}{4\sqrt{G}}\sqrt{\frac{\sigma_{GMC}^2\eta_{bf}}{C^2\Sigma_{mol}}} \tag{3.36}$$

The coefficient $C = 0.7kms^{-1}pc^{-0.5}$. We assume $\sigma_{GMC} = 10km/s$. As shown in Figure 3.15, this method will bring down the efficiency by a factor of 10. The maximal ϵ_{ff} will be on the order of 10%, which is closer to the observations of individual GMCs (Lee et al. 2016). However, this analysis doesn't change the decreasing trend of ϵ_{ff} as a function of Σ_{mol}. Moreover, the assumption that all GMCs have same σ_v makes the trend even steeper. ϵ_{ff} on galactic scale is still a representative quantity for comparing the efficiency of star formation between different regions within Arp 240.

3.5.2 Toomre Stability

As shown in Section 3.3, both galaxies are still fairly normal rotating disks. Therefore, we can apply a Toomre stability analysis to see if the star forming regions satisfy the instability criterion and if there is a dependence of t_{dep} on the value of Toomre factor. Comparing to Leroy et al. (2008), we use

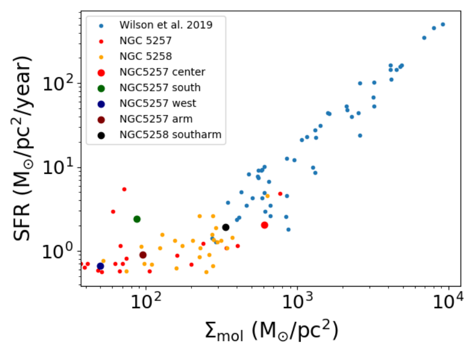

(a)

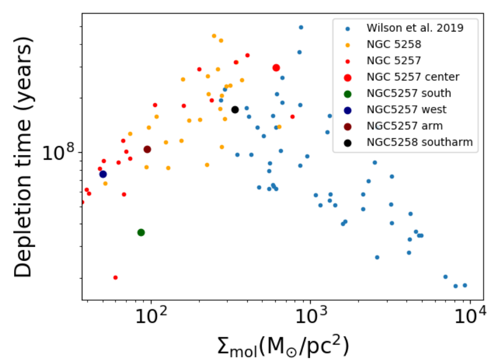

(b)

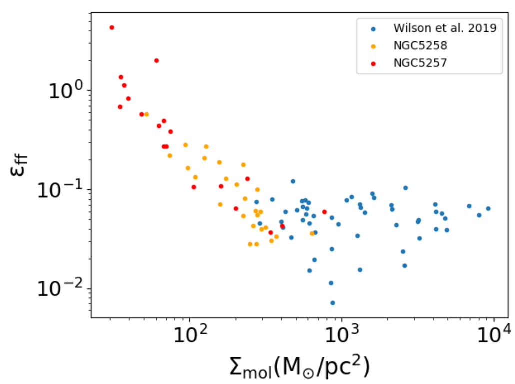

(c)

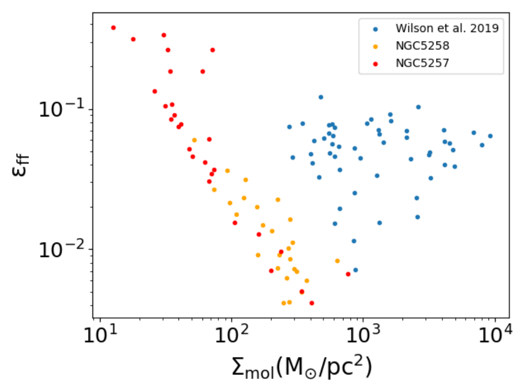

(d)

Figure 3.15: (a) Σ_{SFR} versus Σ_{mol} . (b) t_{dep} versus Σ_{mol}. The bottom two panel show SFE per freefall time ϵ_{ff} versus Σ_{mol} on (c) galactic scale and (d) GMC scale assuming the beam filling factor to be 0.1 and velocity dispersion to be 10 km/s. We assume the ULIRG conversion factor for all the galaxies. While calculating the surface density, we do not correct for the inclination angle. In the first row we calculate the free fall time with the measured velocity dispersion. In the second row we calculate the free fall time assuming a velocity dispersion to be 10 km/s.

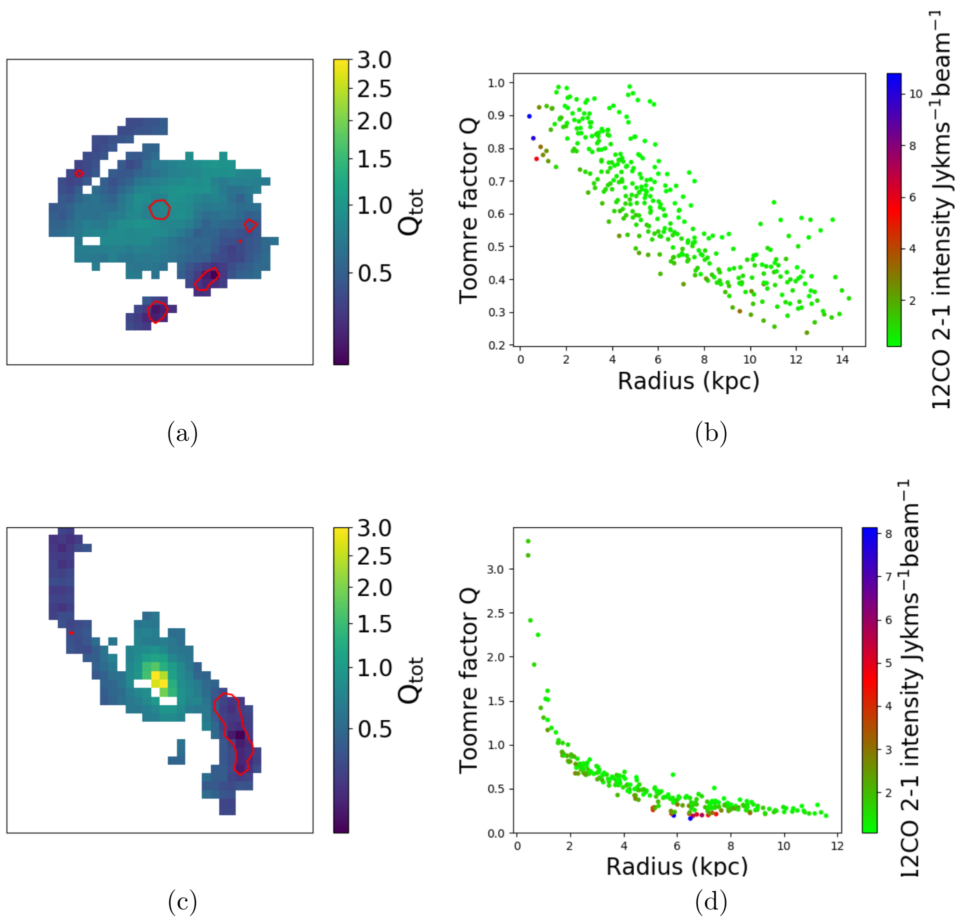

Figure 3.16: The Toomre factor map and scatter plot of NGC 5257 (first row) and NGC 5258 (second row). The red contour in the map is the 33 GHz continuum at a level of 2.0 $\times 10^{-5}$ Jy beam^{-1}. The scatter plot is color coded by the ^{12}CO J=2-1 intensity.

the measured gas velocity dispersion instead of assuming a constant value. Therefore, we might get different conclusions from Leroy et al. (2008), who found there is no correlation between the Toomre factor and the depletion time.

The Toomre factor for a pure gas disk is given by

$$Q = \frac{\sigma_v \kappa}{\pi G \Sigma_{mol}} \tag{3.37}$$

where Σ_{mol} and σ_v are the surface density and the velocity dispersion measured with a ^{12}CO J=2-1 line. We assume the ULIRG conversion factor. κ is the epicyclic frequency given by

$$\kappa = \sqrt{2}\frac{V}{R}(1 + \frac{dlnV}{dlnR}) \tag{3.38}$$

where V is the rotational speed and R is the radius from center. We use the parametric fitted rotation curve from Fuentes-Carrera et al. (2019). For galaxies, the stellar gravitational potential will help to stablize the disk. Wang & Silk (1994) introduce the composite Toomre factor which includes the effect of stars

$$Q_{tot} = Q(1 + \frac{\Sigma_\star}{\Sigma_{mol}}\frac{\sigma_v}{\sigma_\star}) \tag{3.39}$$

where $\Sigma_\star$ and $\sigma_\star$ are the surface density and velocity dispersion of stars in the galaxy. The surface density of the stars is obtained with 3.6 um and 4.5 um Spitzer image (See section 2.3). We do not have the data for $\sigma_\star$. We use the theoretical equation (Leroy et al. 2008) based on the assumption of disk hydrostatic equilibrium, which is

$$\sigma_{\star,z} = \sqrt{\frac{2\pi G l_\star}{7.3}} \Sigma_\star^{0.5} \tag{3.40}$$

$$\sigma_\star = \sigma_{\star,R} = \sigma_{\star,z}/0.6 \tag{3.41}$$

where $\sigma_{\star,R}$ and $\sigma_{\star,z}$ are the stellar velocity dispersion along the vertical and radial direction and $l_\star$ is the scale length of the stellar disk, which is 4.2 kpc and 5.8 kpc for NGC 5257 and NGC 5258 respectively (Fuentes-Carrera et al. 2019).

The Q_{tot} maps for the two galaxies are shown in Figure 3.16. Both galaxies have the majority of the disk with $Q_{tot} < 1$, except for the very central region of NGC 5258. For the center of NGC 5257, the Toomre factor is close to the critical value 1.0, which satisfies the instability criterion. Except for that region, all the star forming regions have a Toomre factor below 0.5, which is highly unstable to gravitational collapse. In the center of NGC 5258, the Q value is about 3, which is consistent with the fact that this is not a star forming region. We also plotted the radial profile of Q color coded by the ^{12}CO J=2-1 intensity. The general decreasing trend is set by the epicycle frequency κ. The Toomre factor without the stellar component correction Q also follows the same trend, with values above 1.0. The stellar component brings down Q by a factor of $2.5 \sim 10$.

For Toomre factors below 0.5, the GMC lifetime is regulated by the gravitational collapse time (Jeffreson & Kruijssen 2018). In this case, we expect ϵ_{ff} to be representative of the true efficiency for gas to form stars. As we mentioned in section 3.5.1, we can still use the galactic ϵ_{ff} for comparing different regions in Arp 240. ϵ_{ff} as a function of the Toomre factor is shown in Figure

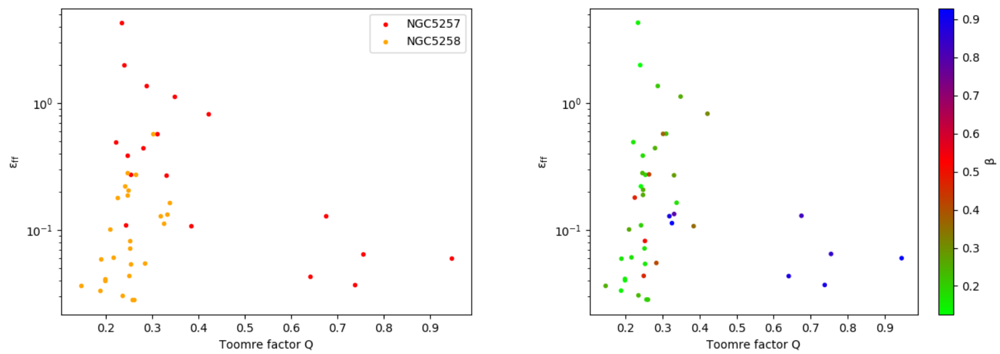

(a) (b)

Figure 3.17: (a) SFE per free fall time as a funtion of the Toomre factor. (b) The same plot color coded by the circular velocity differential β.

3.17. For NGC 5257, there is a general decreasing trend. However, for NGC 5258, similar Q_{tot} corresponds to much lower ϵ_{ff}. Most of these points come from the star forming region in the south spiral arm of the galaxy.

We further explored if cloud shear could cause the difference in the efficiency. We calculated the circular velocity differential β, which is

$$\beta = \frac{d\ln v_c(R)}{d\ln R} \tag{3.42}$$

where $v_c(R)$ is the circular velocity at radius R. In Figure 3.17 (b), we can see that on average, ϵ_{ff} decreases as β increases. However, at low Toomre factor end, points with low β can have both high and low ϵ_{ff}, which might suggest that cloud shear is not the cause for the difference. However, we need to be aware this is an early merger system and clouds may not entirely follow circular motion.

3.6 Discussion and Conclusion

3.6.1 CO-to-H_2 Conversion Factor

We modeled the gas properties with the RADEX code. Due to the lack of molecular lines, we have to fix the abundance ratio to do the modeling. Generally the beam averaged column density is well constrained for each assumed [^{12}CO/^{13}CO] abundance ratio and therefore we can calculate the conversion factors in different cases. Despite the fact that the conversion factor relies on the abundance ratio, we can still constrain the upper and lower limit of the conversion factor given reasonable assumptions for the [^{12}CO/^{13}CO] abundance ratio. The upper limit of the conversion factor is about 1.3 (including helium), which is close to the typical ULIRG conversion factor. We also performed an LTE analysis across the whole region of both galaxies, which also suggests most of regions will have a lower conversion factor than the typical ULIRG value. Generally, the conversion factor will be decreased by the high temperature of the gas or high velocity dispersion of the clouds (Bolatto et al. 2013).

In our later analysis, we use the conversion factor of 0.8 (Downes & Solomon 1998). This is the value without helium correction. We further multiply the calculated gas mass by 1.4 to get the total molecular gas mass. However, the modeled conversion factor from RADEX is typically lower than this value. For a similar type of merger system like Arp 55, the nuclear regions have [^{12}CO/^{13}CO] abundance ratios of 15 $\sim$ 30 (Sliwa et al. 2017). If we adopt an abundance ratio of 30, this will give us a conversion factor of 0.3 for the center of NGC 5257, which will bring down our estimated gas mass. On the other hand, in the RADEX modeling, we must assume a certain [^{12}CO/H_2] abundance of 2×10^{-4} as input. Clouds in the Milky Way generally have [$^{12}CO/H_2$] of about 10^{-4} (van Dishoeck et al. 1992) with values ranging from 5×10^{-5} to 2.7×10^{-4} (references in Zhu et al. 2003). Zhu et al. (2003) derived the typical [$^{12}CO/H_2$] value for the Antennae of between $0.5 \sim 1.0 \times 10^{-4}$. If this is also the case for Arp 240, then our estimated conversion factor should be a bit higher. In consequence, the real conversion factor might still be close to the typical ULIRG conversion factor we assumed.

3.6.2 Turbulence Model

In this thesis, we explored the relationship between the molecular gas properties and the SF activity in different regions of this system. In the turbulence regulated model, ϵ_{ff} is the important parameter to characterize the SF activity. From the Toomre map of the two galaxies, we can see that most star forming regions have Toomre factor Q_{tot} smaller than 0.5, which suggests that gravitational collapse is the dominant process for cloud to form stars (Jeffreson & Kruijssen 2018). In simulations, ϵ_{ff} is a constant value of 1% with little scatter (Grudić et al. 2019, and references therein). However, observations show a much larger scatter with values up to 10% (e.g. Lee et al. 2016). We adopted two methods to calculate ϵ_{ff}. In the first method, we assume the SF activity is regulated by the overall properties of the molecular gas disk. In this case, we found some regions with ϵ_{ff} exceeding 1. In the second method, we assume the SF activity is regulated by the collapse of individual GMCs. Because we do not have enough resolution to resolve individual GMCs, we need to make assumptions about the beam filling factor and the velocity dispersion. In spite of that, we get a more realistic ϵ_{ff} which is well below 1. However, the large scatter in this parameter is in contradiction with simulation predictions. The highest ϵ_{ff} is above 10%. Most of these points come from the south continuum source in NGC 5257, which is likely to be a star cluster (see section 3.4). Leroy et al. (2018) studied star clusters in the center of NGC 253 and found their ϵ_{ff} is generally larger than 10%. At the highest surface density end, some points have an efficiency below 1%. One important assumption we made in our GMC analysis is the beam filling factor $\eta_{bf} = 0.1$. In the high surface density ($> 100\ M_{\odot} pc^{-2}$), η_{bf} is probably close to 1.0, which will bring up the ϵ_{ff}. As we have discussed in the previous section, our adopted ULIRG conversion may probably lead to an overestimate of the molecular gas content and thus bring down the efficiency, particularly for the center of NGC 5257. Another factor is the assumed velocity dispersion. Observations show higher velocity dispersion of GMC in mergers like Antennae (Sun et al. 2018). Therefore, our assumed velocity dispersion of individual GMC might lead to an underestimate of the efficiency. To further study what influence the ϵ_{ff}, we need GMC scale resolution data.

3.6.3 Conclusion

We summarize major conclusions of this paper:

- As a LIRG, Arp 240 has a gas fraction close to typical normal spiral galaxies (assuming a ULIRG conversion factor). The global gas fraction is 0.03 for NGC 5257 and 0.046 for NGC 5258. On the other hand, the global depletion time is about 10^8 years, which is a dex lower than typical normal spiral galaxies. Recent studies (Violino et al. 2018; Pan et al. 2018) find that early mergers typically have higher gas fractions but similar SFEs when compared to normal spiral galaxies. Therefore, Arp 240 is a special case for the early merger systems which has a significantly higher SFE.

- The gas is concentrated in the center of NGC 5257. This is consistent with the theory that gas will inflow towards the center. However, NGC 5258 shows gas concentration in the south spiral arm instead of the center. Correspondingly, the 3.6 and 4.5 μm, which trace the stellar mass, also shows peak at that region. The mass concentration is this area is probably caused by the compression from the tidal field.

- The RADEX model shows that the center of NGC 5257 and the south arm of NGC 5258 have similar temperature and density. On the other hand, the off-center ^{12}CO J=3-2 peak region in NGC 5257 has gas with much higher temperature and lower density, which suggests ^{12}CO J=3-2 emission from this region mostly traces the warm-phase gas.

- As a starburst galaxy, Arp 240 has a conversion factor closer to the ULIRG conversion factor. This is confirmed both by RADEX modeling of ^{12}CO J=3-2 detected regions and LTE analysis across entire galaxies. However, the calculated conversion factor is dependent on the assumed [^{12}CO/^{13}CO] abundance ratio. For similar early merger systems like Arp 55, the abundance ratio is about $15 \sim 30$, which means the conversion factor ($0.1 \sim 0.3$) in Arp 240 will be much lower even than the typical ULIRG conversion factor. We argue that our input [^{12}CO/H_2] ratio might be an overestimate.

- The depletion time for star forming regions can be as short as 10^7 years for the off-center starburst region in NGC 5257. This region corresponds to several identified star clusters (Linden et al. 2017). The south continuum source corresponds to a single young (3.3 Myrs) massive ($4\times10^6 M_\odot$) star cluster. The gas surrounding this single cluster is not gravitationally bound with virial mass to gas mass ratio of ~ 5. However, whole clump of detected gas in that region might be gravitationally bound with ratio ~ 1.9.

- We calculated the galactic SFE per freefall time ϵ_{ff} for different regions of both galaxies. The value can be above 100% for some off-center starburst regions. We argue that this suggests the star forming activity in parts of Arp 240 is regulated by cloud collapse on GMC scales. We show that ϵ_{ff} on GMC scales can be a factor of 10 lower than that on galactic scales, with the highest value of several 10%. This value is consistent with typical $\epsilon = M_\star/M_{mol}$ for super star clusters.

- For most star forming regions in the system, the Toomre factor Q_{tot} is below 0.5, which suggests the SF activity is regulated by gravitational collapse. ϵ_{ff} has no significant dependence on Q_{tot} especially in the lower Q_{tot} regime. Shear also seems not to be the cause for the different ϵ_{ff}.

Chapter 4

Kinematic Results

Arp 240 is an early merger system. As we can see from the ^{12}CO J=2-1 kinematic maps, both galaxies show rotation patterns similar to normal spiral disk galaxies. The rotation patterns of the two galaxies have already been shown in Hα images (Fuentes-Carrera et al. 2019). However, there are still some irregular gas motions shown in the velocity field. For example, the southwest region in NGC 5257 shows the opposite line of site velocity from the neighboring regions (see Fig. 3.2). In order to quantitatively compare the gas motion with the rotation of the spiral disk, we decided to fit the rotation curve of the ^{12}CO J=1-0 and ^{12}CO J=2-1 maps. For rotation curve fitting, we use 2 types of methods, 2D and 3D fitting. We use DiskFit (Sellwood & Spekkens 2015) for 2D fitting and Barolo (Di Teodoro & Fraternali 2015) for 3D fitting. We will discuss each method in the following sections. The final result of the rotation curve fitting is shown in Fig. 4.1.

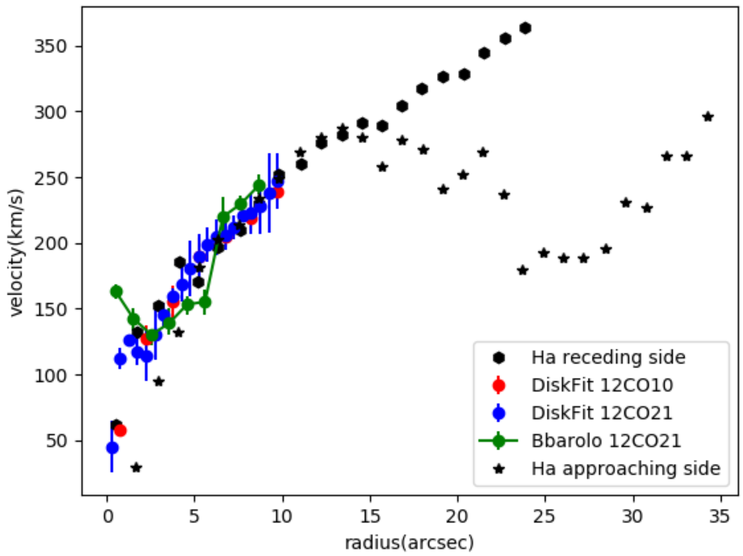

(a)

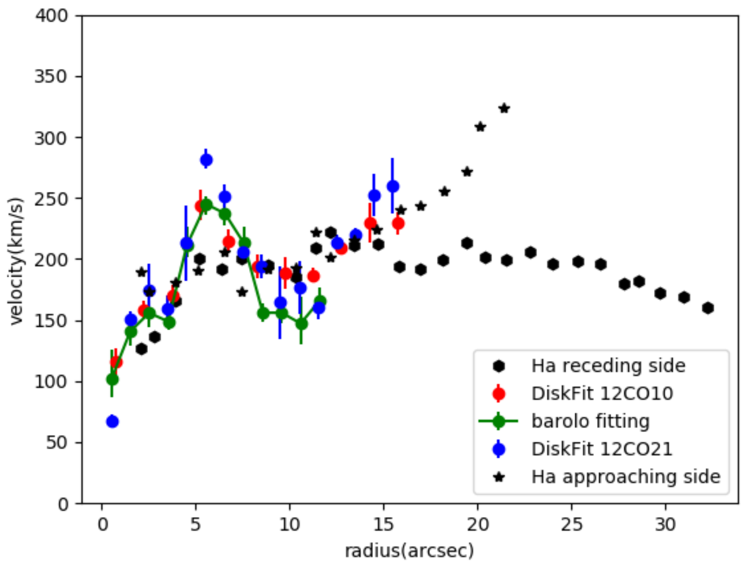

(b)

Figure 4.1: The rotation curve of (a) NGC 5257 and (b) NGC 5258.

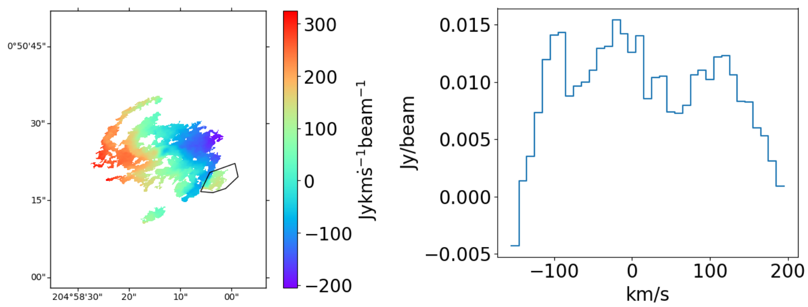

(a) (b)

Figure 4.2: Anomalous kinematic region in NGC 5257. (a) The region in the velocity field map. (b) The mean intensity spectrum of this region of the ^{12}CO J=2-1 cube.

4.1 2D Fitting

We use DiskFit for the 2D kinematic modeling of Arp 240. In the DiskFit modeling, the galaxy is assumed to be a thin disk with a single fixed inclination and position angle.

From the previous chapter, we know both NGC 5257 and NGC 5258 are weakly barred galaxies. Considering simple modeling of the disk with only circular motion, the general expression of the rotational velocity is (Spekkens & Sellwood 2007)

$$V_{rot}(r,\theta) = V_0(r) + \sum_{m=1}^{\infty} V_m cos[m\theta + \theta_m(r)] \tag{4.1}$$

The rotational velocity is not perturbed much periodically. We therefore only fit the rotational velocity to the zeroth order.

We can see from the moment 1 map that there is an anomalous velocity region in the south west of NGC 5257, as encircled in Fig. 4.2. To exclude this region from the fitting, we adopt the simplest method to cut the outermost

Table 4.1: Geometric properties of NGC 5257 and NGC 5258 derived from different data

	NGC 5257		NGC 5258	
	inclination angle(°)	position angle(°)	inclination angle(°)	position angle(°)
^{12}CO J=1-0	58.71 ±3.14	111.68 ±0.27	55.1 ±1.9	213.3 ±0.85
^{12}CO J=2-1	65.23 ±5.19	110.11 ±1.61	55.22 ±3.59	216.35 ±4.99
Hα	58 ±5	95 ±3	57 ±4	218 ±5

radius to be 9.75 arcsec. For NGC 5258, as shown in the Hα literature data (see Fig. 4.1), the rotation curve starts to bifurcate at around 15″ from the center. Therefore, we set the outermost radius to be ∼ 15″.

The rotation curve result is shown in Fig. 4.1. The rotation curves derived from the different datasets agree quite well with each other for NGC 5257. For NGC 5258, the ^{12}CO J=1-0 and ^{12}CO J=2-1 curves are consistent with each other, but show a systematic deviation from Hα result between 5″ to 10″ (2.5–5 kpc) from the center. The bump shown in our fitted curve suggests that molecular gas in that region might not strictly follow the circular motion.

To further check our results, we first compare the derived geometric properties from our data with those from Hα data, as shown in Table 4.1. Our fitted results generally agree with Hα results quite well except for the position angle of NGC 5257. We suspect that might be caused by the varying position angle for rings at different radii.

We also check if our fitted rotation curve is representative of our datasets. To do this, we overlay our fitted rotation curve on the position-velocity (PV) diagram of the modeled galaxy, as shown in Fig. 4.3. We can see the rotation curve agrees with the observed data pretty well along the major axis for both galaxies. However, we can see that for NGC 5258, there is less data in the PV diagram. If the fitting is heavily affected by the data along the major axis,

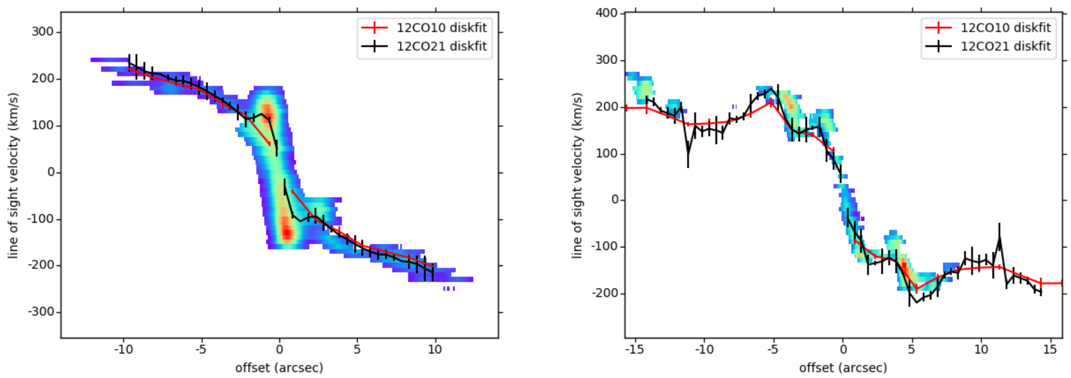

(a) (b)

Figure 4.3: DiskFit rotation curve overlaid on the ^{12}CO J=2-1 PV diagram along the major axis of (a) NGC 5257 and (b) NGC 5258.

this might indicate the 2D fitting for NGC 5258 is less trustworthy.

4.2 3D Fitting

4.2.1 Rotation Curve

In this section, we fit the rotation curve of both galaxies through 3D Barolo fitting. As mentioned in the previous section, both ^{12}CO J=1-0 and ^{12}CO J=2-1 give similar results despite the beam smearing effect. Therefore, we will only use the ^{12}CO J=2-1 image cube for kinematic fitting. The image cube is processed using the script from Sun et al. (2018) to pick out the signals. 3D Barolo uses the tilted-ring model to fit the rotation curve. This model assumes a thin disk with only circular motion around the center. Therefore, the disk can be broken into rings with different radii around the center. Each ring has its own inclination angle and position angle. In this case, the velocity towards the line of sight in each ring is calculated as

$$V_{los}(R) = V_{sys} + V_{rot}(R) cos\theta sini \tag{4.2}$$

where V_{sys} is the systematic velocity, V_{rot} is the rotational velocity of each ring and i and θ are the inclination angle and position angle of each ring. Many normal spiral galaxies such as our Milky Way are observed to have warps (Chen et al. 2019). In this case, the rotation curve can be better fitted by variable inclination angles and position angles. However, as mentioned in the documentation (Di Teodoro & Fraternali 2015), inclination angle is the hardest parameter to constrain. Therefore, the initial guess of the inclination angle matters a lot. In this case, we pick the inclination angle and position angle from Fuentes-Carrera et al. (2019) as our initial guess. It is also not advisable to let the inclination angle and position angle vary across the entire parameter space. We set the range of inclination angle to be 5° above and below the initial guess and of position angle to be 15° above and below the initial guess, which is the default setting of the code. The initial guess of the rotational velocity also affects the final result. In order to get robust result, we bootstrap the previous result into the next run and loop for 3 times. Generally we set the initial velocity to 100 km/s and the velocity dispersion to be 8 km/s (default).

For NGC 5257, as we can see from the velocity field map, there is a kinematically anomalous region in the south west region, as encircled in Fig. 4.2. The spectrum of this region also shows a double peak. Therefore, we need to remove the anomalous component from the image cube. We mask out the emission in this region between the velocity range 10 $\sim$ 200 km/s. We first proceed with fitting both sides of the galaxy. The result is shown in Fig. 4.4. We can see there is a deep drop from one iteration to the next at 4.0 kpc from the center in the rotation curve. As we can see from the major axis PV diagram, this is where the modeled data and the observed data start to become different. From the ^{12}CO J=2-1 moment 0 map (Fig. 3.1) and moment 1 map (Fig. 3.2), we can see the approaching side of the galaxy is more perturbed than the receding side. Therefore, we consider only fitting the receding side of the galaxy. The result is also shown in Fig. 4.4. We can see that there is no longer a drop in the rotation curve at the outermost radius. Furthermore, the modeled data shown in the PV diagram is more consistent with the observed data. By overplotting the Barolo fit result over the other fitted result (see Fig. 4.1), we can see the Barolo fitting generally agrees well with the other fitted result. The major difference between this 3D fitting and the other 2D fitting is the fact that Barolo fitting has significantly higher velocity than the other fitting near the center. Generally the 2D fitting suffers most from the beam smearing effect. Therefore, Barolo may better recover the rotational velocity near the center.

For NGC 5258, we also started with fitting both sides. As we can see from the Hα result, the rotation curve becomes different at around 15 arcsec from the center. Therefore, we set our outermost radius to be $\sim$ 15 arcsec (7 kpc). As shown in Fig. 4.5 (a), the rotation curve in the outermost region fluctuates a lot. This fluctuation may be an artificial effect from the fitting. Therefore, we cut the outermost radius to be 12 arcsec and then do the fitting again. The result is shown in 4.5 (b). We can see the multiple runs are consistent with each other.

The rotation curve of NGC 5258 shows a bump between 4 $\sim$ 8 arcsec. This

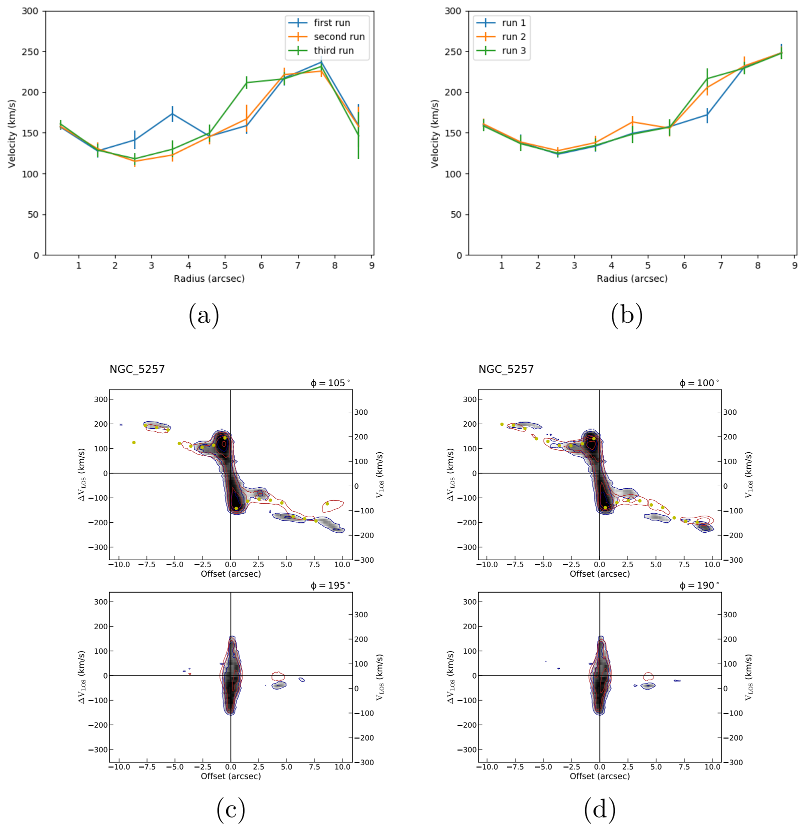

Figure 4.4: Barolo fitting of NGC 5257 with both sides (first column) and receding side only (second column). The top row is the rotation curve of the 3 runs (see text). The bottom row is the corresponding PV diagram. The blue contour indicates the observed data and the red contour indicates the modeled data. Yellow dots are the fitted rotation curve points.

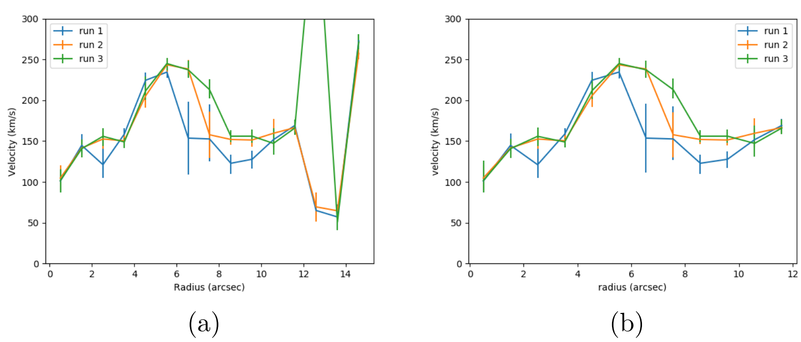

Figure 4.5: Barolo fit for NGC 5258 with the outermost radius to be (a) 15 arcsec (b) 12 arcsec.

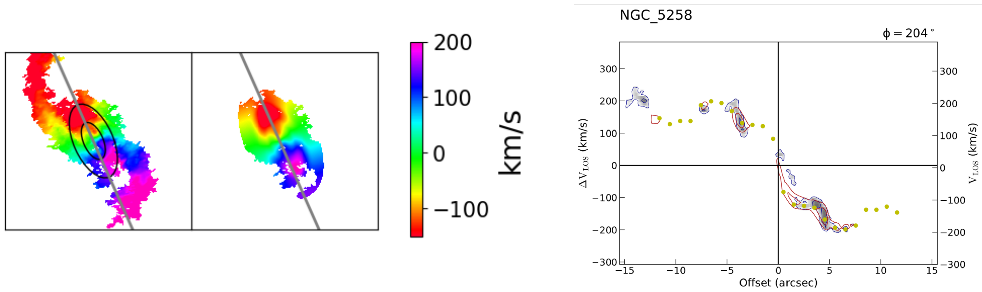

(a) (b)

Figure 4.6: (a) The observed and modeled velocity field. The gray line is the position angle of the galaxy and the ring is the region with bump in the rotation curve fitting. (b) The line of sight modeled velocity overlaid on the position velocity diagram of NGC 5258 (see Fig. 4.4 for detailed description).

bump is not significant in the Hα fitting but is significant in our CO 2D fitting. We further check the observed moment 1 map and modeled moment 1 map, as shown in Fig. 4.6. The bump region is encircled with a ring. We can see there is a sharp change in velocity field between the region along the major axis within the ring and its neighboring regions. These neighboring regions are in between the central disk and spiral arms and therefore probably perturbed by the tidal interaction.

4.2.2 Velocity Dispersion

3D Barolo not only gives the fitted rotation curve, but also gives the fitted velocity dispersion within the ring of each radius. The basic procedure for Barolo to fit the velocity dispersion is as follows.

After inputting the image cube, Barolo will identify clouds in the imagecube and project them onto the cylindrical coordinates of the modeled disk. Once the positions of the clouds are determined, each cloud is divided into multiple sub clouds, which are built around the average velocity of the cloud. These sub clouds have a velocity distribution of a Gaussian function with dispersion σ_v, which is

$$\sigma_v^2 = \sigma_{gas}^2 + \sigma_{intr}^2 \tag{4.3}$$

where σ_v is the total velocity dispersion observed for each sub cloud, σ_{gas} is the intrinsic gas velocity dispersion and σ_{intr} is the instrument induced velocity dispersion, which is calculated as

$$\sigma_{intr} = W_{ch}/\sqrt{2ln2} \tag{4.4}$$

where W_{ch} is the channel width of the input cube.

The velocity dispersion σ_{gas} is allowed to vary from ring to ring but is assumed to be the same within each ring. This makes sense for a typical normal spiral galaxy but might not be appropriate for a perturbed system like Arp 240. Therefore, we tested this model on one of the galaxies NGC 5257.

At the start, we tested if the fitting results vary with different initial guesses of the velocity dispersion. The result is shown in Figure 4.7. As we can see, the fitted rotational velocity is independent of our assumed initial velocity dispersion, which validates our rotation curve fitting result from the previous section. However, the velocity dispersion varies a lot with different assumed values. The default velocity dispersion is 8 km/s, which is a typical velocity dispersion within an individual GMC. But this value might not be appropriate for highly turbulent systems like mergers. We also compared the fitted velocity dispersion result with the measurement from the moment 2 map. In the moment 2 map, we calculated the mean velocity dispersion within each ring. As shown in the figure, the dispersion curve from the moment 2 map is closer to the fitted result with the assumption of 20 km/s and 50 km/s but

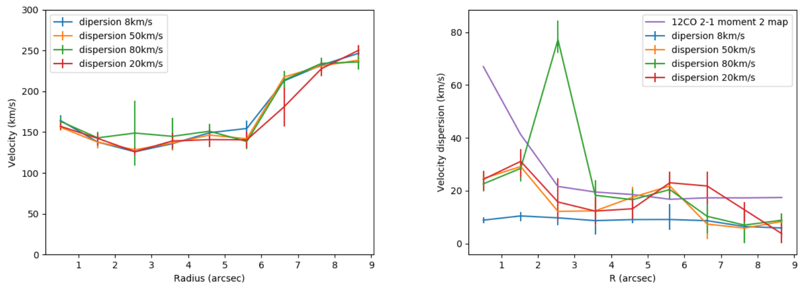

(a) (b)

Figure 4.7: Barolo fit results for NGC 5275 with different initial guess of velocity dispersion. (a). The rotation curve results (b). The velocity dispersion results.

has higher values in the center due to the beam smearing effect. However, the fitted results have much larger fluctuations than the moment 2 map curve, which suggests it is a bad initial guess.

We further compare the quality of the modeled results for different initial guesses by comparing the modeled moment 2 maps with the observed moment 2 maps as shown in Fig. 4.8. We can see that 80 km/s is a bad guess as the modeled dispersion map is clearly different from the observed dispersion map. Both 8 km/s and 50 km/s don't reproduce the high velocity dispersion in the spiral arms very well. We can also see a clear ring structure in all of these modeled maps. This could be caused by the assumption that each ring is supposed to have a single value of σ_{gas}. We know that the receding side of the galaxy is more perturbed than the approaching side for NGC 5257. Therefore, that assumption probably fails in this case.

4.3 Summary

We summarize the major conclusions of this chapter:

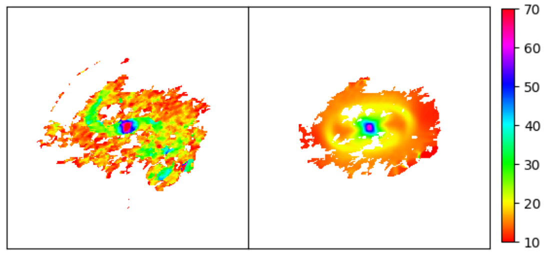

(a)

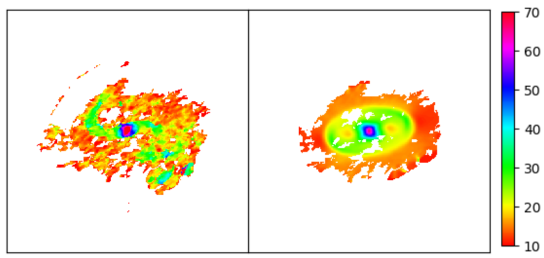

(b)

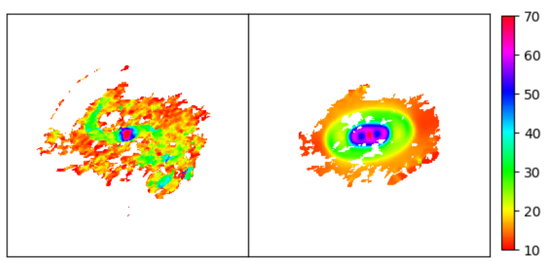

(c)

Figure 4.8: Comparison between the observed velocity dispersion (Left) and the Barolo modeled velocity dispersion (Right) with different initial guesses of velocity dispersion of (a) 8 km/s (b) 50 km/s (c) 80 km/s.

- The 2D DiskFit fitting results for the rotation curve and geometry of both galaxies based on ^{12}CO J=1-0 and ^{12}CO J=2-1 are consistent with each other. We also compared both results with Hα 2D fitting from Fuentes-Carrera et al. (2019). The geometry derived from Hα is consistent with that derived from molecular lines, except for a slight difference in the position angle of NGC 5257. The rotation curve of NGC 5257 agrees with the Hα curve but that of NGC 5258 shows a small bump between 5 to 10 arcsec from the center, which is not obvious in the Hα curve. This small bump might be caused by non-circular motion of the gas in that region due to tidal effects.

- The 3D Barolo fitted rotation curve based on the ^{12}CO J=2-1 data is generally consistent with our DiskFit 2D results except for center of the galaxies. This might be caused by the beam smearing effect. For NGC 5257, the rotation curve also agrees well with the Hα fitting. But for NGC 5258, the rotation curve shows a similar bump as the 2D molecular line fitting, which doesn't show in the Hα fitting. This suggests the molecular gas motion traced by ^{12}CO is different from the ionized gas motion traced by Hα emission,.

- We tried to test the Barolo velocity dispersion fitting on NGC 5257. It turns out the modeled velocity dispersion is highly dependent on the initial guess. The modeled moment 2 maps made by Barolo also show a ring structure, which probably comes from the assumption each ring has a single value of gas velocity dispersion σ_{gas}. We argue that this assumption is not valid for perturbed systems like Arp 240.

Chapter 5

Summary and Future Work

5.1 Summary

We have presented a detailed study of the early-stage galaxy merger Arp 240. We mainly studied the molecular gas properties and their relationships with the star forming activity. The summary is as follows:

Arp 240 is a starburst galaxy with sSFR about 7 times higher than that of main sequence galaxies. However, the gas fraction (divided by stellar mass) of this system is close to that of normal spiral galaxies. On the other hand, this system shows enhanced SFE ($t_{dep} \sim 10^8$ years). The resolved study shows some extreme regions with depletion times shorter than 10^7 years. This is in contrast to most galaxy pairs which have higher gas fractions but relatively normal SFE (Pan et al. 2018). As shown in simulations, this system has been through the first passage, which might be different from most pairs where the merging event hasn't happened yet. For the large survey of pair galaxies, people generally use projection distance as an indicator of the merging stage. This diagnosis might ignore the case when two galaxies have passed through each other. Therefore, a more accurate method needs to be developed to identify merger stages more accurately. These methods include counting the tidal features in mergers and identifying perturbed features based on rotation curve fitting.

We use RADEX modeling to fit the properties of the molecular gas. In this case, we can constrain the beam averaged column density of the molecular gas relatively well with a given assumed [^{12}CO/^{13}CO] abundance ratio. The result shows that for most star forming regions, the CO-to-H_2 conversion factor is close to the typical ULIRG conversion factor. We also performed an LTE analysis on this system, which shows the majority of the regions in these two galaxies show a conversion factor close to the ULIRG conversion factor. The result from the LTE analysis is close to that from the RADEX modeling. This is different from what what we would expect for this early merger which was expected to have a conversion factor between the Milky Way value and the ULIRG value. Perhaps as a typical LIRG, the conversion factor has already changed from the Milky Way value. As a starburst system, Arp 240 might actually in the later stage compared with less starbursting pairs. Therefore, to catch an earlier stage merger, we might need to search for those less starbursting systems outside the GOALS sample.

Arp 240 shows the organized rotating features of normal spiral galaxies. We fit the rotation curve for both galaxies with 2D and 3D fitting tools. The fitted rotation curve of the molecular gas generally agrees well with that of the ionized gas from Hα emission. We use the rotation curve derived from Hα to derive the combined Toomre factor Q_{tot} for Arp 240. We found that most starburst regions have Q_{tot} smaller than 0.5. The center of NGC 5257 has $Q_{tot} \sim 1$, which is the critical value for star forming activity. On the other hand, the center of NGC 5258 has $Q_{tot} > 3$ and is not star forming according to the 33 GHz continuum. This suggests that the star forming activity might be regulated by the gravitational instability. However, we didn't find a significant correlation between ϵ_{ff} and Q_{tot}. For most of regions, Q_{tot} is well below 1, which is inconsistent with nearby spiral galaxies where the star forming regions have $Q_{tot} \sim 1$. The extreme low value of Q_{tot} might be caused by the tidal interaction between the two galaxies. On the other hand, we need to note that our calculated Q_{tot} is mainly brought down below 1 by the stellar component. This might suggest the stellar component contribute a larger fraction to the cloud instability than we expected. This is actually consistent with the study by Romeo & Mogotsi (2017), which suggests the stellar component is the major driver for disk instability in nearby galaxies. However, the stellar velocity dispersion we use for this analysis might not hold true for this interacting system. Nowadays integral field unit (IFU) data has enabled us direct measurements of stellar velocity dispersion. We might therefore get a better understanding of Q_{tot} in these systems.

We further calculated the SFE per freefall time ϵ_{ff} on both galactic and GMC scales. For this starburst system, Σ_{mol} is in the range of 10–1000 $M_{\odot}$ pc^{-2}. For nearby spiral galaxies, Σ_{mol} is about 10–100 $M_{\odot}$ pc^{-2}, in which regime the molecular gas is in the form of clouds. In the higher surface density regime, we would expect the molecular gas dominates the gas disk. On galactic scales, we get ϵ_{ff} exceeding 100 % in the lowest Σ_{mol} regime. If we assume the molecular gas is in the form of clouds in this regime and calculate the GMC ϵ_{ff} based on some simple assumptions, we can get the maximal ϵ_{ff} of several 10%, which is closer to the maximal value for individual GMCs in the Milky Way (Lee et al. 2016). We can also observe a decreasing trend of ϵ_{ff} as a function of increasing Σ_{mol}, which is probably caused by the decreasing η_{bf} as Σ_{mol} increases. On the starburst Σ_{mol} at the other end, ϵ_{ff} on galactic scales is about several times 1%, which is consistent with the generally assumed value. This probably indicates that molecular gas dominates the gas disk in this regime. If we have higher resolution data on GMC scales, we can actually disentangle those two situations and quantitatively calculate the actual ϵ_{ff} for different Σ_{mol}. Then we can apply the turbulence model to see how ϵ_{ff} actually depends on other parameters like virial parameter α_{vir} and Mach number $\mathcal{M}$. Then we can actually test if the turbulence model with relatively constant ϵ_{ff} can apply for both GMC and galactic scales.

5.2 Future Work

For this specific system, we actually are short of lines to fully constrain all the physical parameters of the system. We adopted the ^{12}CO J=3-2 line from SMA observations. In the SMA observations, only a few gas concentrated regions are detected. On the other hand, the SMA observations have a short spacing problem and therefore might miss a significant amount of flux. The ALMA compact array has a beam size of about $4''$, which is close to the resolution of the SMA at this wavelength. We therefore proposed for the ALMA supplemental call for cycle 7 to observe this system with the ACA compact array only. This will help us to map the conversion factor across the entire galaxy without the LTE assumption.

For calculating ϵ_{ff}, we adopted several assumptions for the GMC analysis. Recently, ^{12}CO J=2-1 data with GMC resolution for this system has become public (project 2017.1.00395.S, PI: Tanio Diaz-Santos). This can enable us to constrain the assumed parameters like beam filling factor η_{bf} and gas velocity dispersion on GMC scale σ_{GMC}. Furthermore, we can study if the difference in GMC properties like virial parameter α_{vir} and turbulent pressure actually affects the SFE or ϵ_{ff} in different regions.

This study is focused on a specific early merger in the GOALS U/LIRG sample. As shown in this study, Arp 240 has enhanced SFE and normal gas fraction, which is different from typical pairs with enhanced gas fraction and normal SFE. It is interesting to explore the cause of such differences between different early merger systems. In the future, we can try to build a small sample of early mergers from the GOALS sample in comparison with the sample from Violino et al. (2018) to explore if this type of difference generally exists and if so, what is the primary cause for such a difference.

Bibliography

Armus, L., Mazzarella, J. M., Evans, A. S., et al. 2009, PASP, 121, 559, doi: 10.1086/600092

Bigiel, F., Leroy, A., Walter, F., et al. 2008, The Astronomical Journal, 136, 2846, doi: 10.1088/0004-6256/136/6/2846

Bigiel, F., Leroy, A. K., Walter, F., et al. 2011, The Astrophysical Journal, 730, L13, doi: 10.1088/2041-8205/730/2/L13

Boissier, S., Prantzos, N., Boselli, A., & Gavazzi, G. 2003, MNRAS, 346, 1215, doi: 10.1111/j.1365-2966.2003.07170.x

Bolatto, A. D., Wolfire, M., & Leroy, A. K. 2013, Annual Review of Astronomy and Astrophysics, 51, 207, doi: 10.1146/annurev-astro-082812-140944

Bosma, A. 1978, PhD thesis, -

Carroll, B. W., & Ostlie, D. A. 2007, An Introduction to Modern Astrophysics, 2nd edn., ed. S. F. P. Addison-Wesley

Casey, C. M. 2012, MNRAS, 425, 3094, doi: 10.1111/j.1365-2966.2012.21455.x

Catinella, B., Saintonge, A., Janowiecki, S., et al. 2018, MNRAS, 476, 875, doi: 10.1093/mnras/sty089

Chen, X., Wang, S., Deng, L., et al. 2019, Nature Astronomy, 3, 320, doi: 10.1038/s41550-018-0686-7

Cole, S., Lacey, C. G., Baugh, C. M., & Frenk, C. S. 2000, MNRAS, 319, 168, doi: 10.1046/j.1365-8711.2000.03879.x

Cormier, D., Bigiel, F., Jiménez-Donaire, M. J., et al. 2018, MNRAS, 475, 3909, doi: 10.1093/mnras/sty059

Cox, T. J., Jonsson, P., Somerville, R. S., Primack, J. R., & Dekel, A. 2008, MNRAS, 384, 386, doi: 10.1111/j.1365-2966.2007.12730.x

Daddi, E., Elbaz, D., Walter, F., et al. 2010, The Astrophysical Journal, 714, L118, doi: 10.1088/2041-8205/714/1/L118

Di Matteo, P., Bournaud, F., Martig, M., et al. 2008, A&A, 492, 31, doi: 10.1051/0004-6361:200809480

Di Teodoro, E. M., & Fraternali, F. 2015, MNRAS, 451, 3021, doi: 10.1093/mnras/stv1213

Díaz-Santos, T., Armus, L., Charmandaris, V., et al. 2017, ApJ, 846, 32, doi: 10.3847/1538-4357/aa81d7

Dobbs, C. L., Krumholz, M. R., Ballesteros-Paredes, J., et al. 2014, in Protostars and Planets VI, ed. H. Beuther, R. S. Klessen, C. P. Dullemond, & T. Henning, 3

Downes, D., & Solomon, P. M. 1998, The Astrophysical Journal, 507, 615, doi: 10.1086/306339

Dressler, A., Oemler, Augustus, J., Couch, W. J., et al. 1997, ApJ, 490, 577, doi: 10.1086/304890

Ellison, S. L., Catinella, B., & Cortese, L. 2018, MNRAS, 478, 3447, doi: 10.1093/mnras/sty1247

Eskew, M., Zaritsky, D., & Meidt, S. 2012, AJ, 143, 139, doi: 10.1088/0004-6256/143/6/139

Fuentes-Carrera, I., Rosado, M., Amram, P., et al. 2019, A&A, 621, A25, doi: 10.1051/0004-6361/201834159

Galametz, M., Kennicutt, R. C., Calzetti, D., et al. 2013, MNRAS, 431, 1956, doi: 10.1093/mnras/stt313

García-Burillo, S., Usero, A., Alonso-Herrero, A., et al. 2012, A&A, 539, A8, doi: 10.1051/0004-6361/201117838

Grudić, , M. Y., Hopkins, P. F., et al. 2019, MNRAS, 488, 1501, doi: 10.1093/mnras/stz1758

Grudić, M. Y., Hopkins, P. F., Faucher-Giguère, C.-A., et al. 2018, MNRAS, 475, 3511, doi: 10.1093/mnras/sty035

Harris, W. E., & Pudritz, R. E. 1994, ApJ, 429, 177, doi: 10.1086/174310

Hennebelle, P., & Chabrier, G. 2011, ApJL, 743, L29, doi: 10.1088/2041-8205/743/2/L29

Heyer, M., Krawczyk, C., Duval, J., & Jackson, J. M. 2009, The Astrophysical Journal, 699, 1092, doi: 10.1088/0004-637X/699/2/1092

Iono, D., Yun, M. S., & Ho, P. T. P. 2005, The Astrophysical Journal Supplement Series, 158, 1, doi: 10.1086/429093

Jeffreson, S. M. R., & Kruijssen, J. M. D. 2018, MNRAS, 476, 3688, doi: 10.1093/mnras/sty594

Kamenetzky, J., Rangwala, N., Glenn, J., Maloney, P. R., & Conley, A. 2016, ApJ, 829, 93, doi: 10.3847/0004-637X/829/2/93

Kennicutt, Robert C., J. 1998, The Astrophysical Journal, 498, 541, doi: 10.1086/305588

Kennicutt, R. C., & Evans, N. J. 2012, ARA&A, 50, 531, doi: 10.1146/annurev-astro-081811-125610

Kim, W.-T., & Ostriker, E. C. 2007, ApJ, 660, 1232, doi: 10.1086/513176

Kim, W.-T., Ostriker, E. C., & Stone, J. M. 2002, ApJ, 581, 1080, doi: 10.1086/344367

Kodama, T., & Smail, I. 2001, MNRAS, 326, 637, doi: 10.1046/j.1365-8711.2001.04624.x

Krumholz, M. R., Dekel, A., & McKee, C. F. 2012, The Astrophysical Journal, 745, 69, doi: 10.1088/0004-637X/745/1/69

Krumholz, M. R., & McKee, C. F. 2005, The Astrophysical Journal, 630, 250, doi: 10.1086/431734

Larson, K. L., Sanders, D. B., Barnes, J. E., et al. 2016, ApJ, 825, 128, doi: 10.3847/0004-637X/825/2/128

Larson, R. B. 1981, Monthly Notices of the Royal Astronomical Society, 194, 809, doi: 10.1093/mnras/194.4.809

Lee, E. J., Miville-Deschênes, M.-A., & Murray, N. W. 2016, The Astrophysical Journal, 833, 229, doi: 10.3847/1538-4357/833/2/229

Leroy, A. K., Walter, F., Brinks, E., et al. 2008, AJ, 136, 2782, doi: 10.1088/0004-6256/136/6/2782

Leroy, A. K., Bolatto, A. D., Ostriker, E. C., et al. 2018, ApJ, 869, 126, doi: 10.3847/1538-4357/aaecd1

Li, Y., Mac Low, M.-M., & Klessen, R. S. 2005, ApJ, 626, 823, doi: 10.1086/430205

Linden, S. T., Evans, A. S., Rich, J., et al. 2017, ApJ, 843, 91, doi: 10.3847/1538-4357/aa7266

Linden, S. T., Song, Y., Evans, A. S., et al. 2019, ApJ, 881, 70, doi: 10.3847/1538-4357/ab2872

Lukić, Z., Heitmann, K., Habib, S., Bashinsky, S., & Ricker, P. M. 2007, ApJ, 671, 1160, doi: 10.1086/523083

Madau, P., Pozzetti, L., & Dickinson, M. 1998, ApJ, 498, 106, doi: 10.1086/305523

Małek, K., Bankowicz, M., Pollo, A., et al. 2017, A&A, 598, A1, doi: 10.1051/0004-6361/201527969

Martin, C. L., & Kennicutt, Robert C., J. 2001, ApJ, 555, 301, doi: 10.1086/321452

Masks for Deconvolution. 2017, Masks for Deconvolution, https://casa.nrao.edu/casadocs/casa-5.1.0/synthesis-imaging/masks-for-deconvolution

McKee, C. F., & Ostriker, E. C. 2007, ARA&A, 45, 565, doi: 10.1146/annurev.astro.45.051806.110602

Mengel, S., Lehnert, M. D., Thatte, N., & Genzel, R. 2005, A&A, 443, 41, doi: 10.1051/0004-6361:20052908

Mihos, J. C., & Hernquist, L. 1996a, The Astrophysical Journal, 464, 641, doi: 10.1086/177353

—. 1996b, ApJ, 464, 641, doi: 10.1086/177353

Moreno, J., Torrey, P., Ellison, S. L., et al. 2019, MNRAS, 485, 1320, doi: 10.1093/mnras/stz417

Mould, J. R., Huchra, J. P., Freedman, W. L., et al. 2000, ApJ, 529, 786, doi: 10.1086/308304

Murphy, E. J., Condon, J. J., Schinnerer, E., et al. 2011, ApJ, 737, 67, doi: 10.1088/0004-637X/737/2/67

Narayanan, D., Krumholz, M., Ostriker, E. C., & Hernquist, L. 2011, Monthly Notices of the Royal Astronomical Society, 418, 664, doi: 10.1111/j.1365-2966.2011.19516.x

Narayanan, D., Krumholz, M. R., Ostriker, E. C., & Hernquist, L. 2012, Monthly Notices of the Royal Astronomical Society, 421, 3127, doi: 10.1111/j.1365-2966.2012.20536.x

Nordlund, Å. K., & Padoan, P. 1999, in Interstellar Turbulence, ed. J. Franco & A. Carraminana, 218

Oemler, Augustus, J. 1974, ApJ, 194, 1, doi: 10.1086/153216

Padoan, P., & Nordlund, Å. 2002, ApJ, 576, 870, doi: 10.1086/341790

Pan, H.-A., Lin, L., Hsieh, B.-C., et al. 2018, The Astrophysical Journal, 868, 132, doi: 10.3847/1538-4357/aaeb92

Papadopoulos, P. P., van der Werf, P., Xilouris, E., Isaak, K. G., & Gao, Y. 2012, The Astrophysical Journal, 751, 10, doi: 10.1088/0004-637X/751/1/10

Privon, G. C., Barnes, J. E., Evans, A. S., et al. 2013, The Astrophysical Journal, 771, 120, doi: 10.1088/0004-637X/771/2/120

Renaud, F., Boily, C. M., Naab, T., & Theis, C. 2009, ApJ, 706, 67, doi: 10.1088/0004-637X/706/1/67

Renaud, F., Bournaud, F., Kraljic, K., & Duc, P. A. 2014, MNRAS, 442, L33, doi: 10.1093/mnrasl/slu050

Robitaille, T. P., & Whitney, B. A. 2010, ApJL, 710, L11, doi: 10.1088/2041-8205/710/1/L11

Romeo, A. B., & Mogotsi, K. M. 2017, MNRAS, 469, 286, doi: 10.1093/mnras/stx844

Romeo, A. B., & Wiegert, J. 2011, MNRAS, 416, 1191, doi: 10.1111/j.1365-2966.2011.19120.x

Ryan, R. E., J., Cohen, S. H., Windhorst, R. A., & Silk, J. 2008, ApJ, 678, 751, doi: 10.1086/527463

Saito, T., Iono, D., Xu, C. K., et al. 2017, ApJ, 835, 174, doi: 10.3847/1538-4357/835/2/174

Sakamoto, K., Okumura, S. K., Ishizuki, S., & Scoville, N. Z. 1999, ApJ, 525, 691, doi: 10.1086/307910

Sanders, D. B., & Mirabel, I. F. 1996, ARA&A, 34, 749, doi: 10.1146/annurev.astro.34.1.749

Sanders, D. B., Soifer, B. T., Elias, J. H., et al. 1988, The Astrophysical Journal, 325, 74, doi: 10.1086/165983

Sargent, M. T., Daddi, E., Béthermin, M., et al. 2014, ApJ, 793, 19, doi: 10.1088/0004-637X/793/1/19

Sellwood, J. A., & Spekkens, K. 2015, arXiv e-prints. https://arxiv.org/abs/1509.07120

Semenov, V. A., Kravtsov, A. V., & Gnedin, N. Y. 2016, The Astrophysical Journal, 826, 200, doi: 10.3847/0004-637X/826/2/200

Shirley, Y. L. 2015, PASP, 127, 299, doi: 10.1086/680342

Sliwa, K., & Downes, D. 2017, A&A, 604, A2, doi: 10.1051/0004-6361/201630139

Sliwa, K., Wilson, C. D., Matsushita, S., et al. 2017, The Astrophysical Journal, 840, 8, doi: 10.3847/1538-4357/aa689b

Sofue, Y., Wakamatsu, K.-I., Taniguchi, Y., & Nakai, N. 1993, PASJ, 45, 43

Spekkens, K., & Sellwood, J. A. 2007, ApJ, 664, 204, doi: 10.1086/518471

Sun, J., Leroy, A. K., Schruba, A., et al. 2018, ApJ, 860, 172, doi: 10.3847/1538-4357/aac326

Teyssier, R., Chapon, D., & Bournaud, F. 2010, ApJL, 720, L149, doi: 10.1088/2041-8205/720/2/L149

Toomre, A. 1964, ApJ, 139, 1217, doi: 10.1086/147861

Toomre, A. 1977

Usero, A., Leroy, A. K., Walter, F., et al. 2015, The Astronomical Journal, 150, 115, doi: 10.1088/0004-6256/150/4/115

van der Tak, F. F. S., Black, J. H., Schöier, F. L., Jansen, D. J., & van Dishoeck, E. F. 2007, A&A, 468, 627, doi: 10.1051/0004-6361:20066820

Violino, G., Ellison, S. L., Sargent, M., et al. 2018, Monthly Notices of the Royal Astronomical Society, 476, 2591, doi: 10.1093/mnras/sty345

Vlahakis, C., Dunne, L., & Eales, S. 2005, MNRAS, 364, 1253, doi: 10.1111/j.1365-2966.2005.09666.x

Wang, B., & Silk, J. 1994, ApJ, 427, 759, doi: 10.1086/174182

Wild, W., Harris, A. I., Eckart, A., et al. 1992, Astronomy and Astrophysics, 265, 447

Wilson, C. D., Elmegreen, B. G., Bemis, A., & Brunetti, N. 2019, arXiv e-prints, arXiv:1907.05432. https://arxiv.org/abs/1907.05432

Wilson, C. D., Petitpas, G. R., Iono, D., et al. 2008, The Astrophysical Journal Supplement Series, 178, 189, doi: 10.1086/590910

Yamashita, T., Komugi, S., Matsuhara, H., et al. 2017, ApJ, 844, 96, doi: 10.3847/1538-4357/aa7af1

Yang, C.-C., Gruendl, R. A., Chu, Y.-H., Mac Low, M.-M., & Fukui, Y. 2007, ApJ, 671, 374, doi: 10.1086/522861

Yun, M. S., Reddy, N. A., & Condon, J. J. 2001, ApJ, 554, 803, doi: 10.1086/323145

Zhu, M., Seaquist, E. R., & Kuno, N. 2003, The Astrophysical Journal, 588, 243, doi: 10.1086/368353